NOTICE
This report was prepared as an account of work sponsored by the United States Government. Neither the United States nor the United States Atomic Energy Commission, nor any of their employees, nor any of their contractors, subcontractors, or their employees, makes any warranty, express or implied, or assumes any legal liability or responsibility for the accuracy, completeness or usefulness of any information, apparatus, product or process disclosed, or represents that its use would not infringe privately owned rights.

THE DEVELOPMENT OF A NEUTRON SPECTROMETER USING MULTI-WIRE SPARK CHAMBERS FOR THE MEASUREMENT OF THE SPECTRA OF STRAY NEUTRONS IN THE VICINITY OF HIGH ENERGY ACCELERATORS

Chun Bin Lim

Lawrence Berkeley Laboratory
University of California
Berkeley, California 94720

ABSTRACT

A method of neutron spectrometry which measures the energy spectra of the stray neutrons around the high energy accelerators, roughly between 50 MeV and 300 MeV, has been developed using a series of multi-wire spark chambers and polyethylene n-p converters. The method is based on the proton producing, neutron induced reactions in the converting medium and the measurement of the proton track lengths with the spark chambers. The proton energy spectrum is constructed from the collected proton track events, and later an incident neutron energy spectrum is unfolded numerically from this proton energy spectrum by solving the integral equation connecting the two quantities in the spectrometer volume using the least squares method.

For this method, 12 spark chambers with a sensitive area $50 \times 50\ cm^2$ have been designed and constructed. The spectrometer was assembled with all the related electronics and its various performances were tested. The proton producing reactions and the particle transport behavior in the detector volume have been throughly analyzed. An approximate integral relation connecting the incident neutron energy spectrum and the detected proton energy spectrum has been established in the above energy region. In the evaluation of the kernel matrix needed in the neutron unfolding process a random sampling technique

MASTER
DISTRIBUTION OF THIS DOCUMENT IS UNLIMITED

was utilized. Finally, the performances of the whole spectrometer set-up and the related neutron unfolding technique have been tested with the measurement of stray neutrons in the 100 MeV region around the 184-Inch Cyclotron at the Lawrence Berkeley Laboratory.

THE DEVELOPMENT OF A NEUTRON SPECTROMETER USING MULTI-WIRE SPARK CHAMBERS FOR THE MEASUREMENT OF THE SPECTRA OF STRAY NEUTRONS IN THE VICINITY OF HIGH ENERGY ACCELERATORS

Contents

Abstract

I. Introduction 1

II. Theory 7

1. Neutron Transport and Proton Generation 7

2. The Model 22

III. Spectrometer Set-up and Related Electronics 40

1. General Spectrometer Set-up and Triggering Logic . . 40

2. Spark Chamber Construction and Operation 49

3. Magnetostrictive Readout and Data Recording 55

4. Test of the Complete Spectrometer Set-up 61

IV. Data Processing 70

1. Method of Recording and Unpacking Data 70

2. Classification of Digitized Wand Data 73

3. Sorting of Good Events and Least Squares Line Fit . . 76

4. Proton Track Length and Conversion to Energy 81

5. Proton Energy Spectrum Generation 85

V. Neutron Spectrum Unfolding 88

1. Process Simulations 88

2. Cross Sections 92

3. Monte Carlo Simulation Procedure 112

4. Kernel Generation 117

5. Solution of the Neutron Spectrum from the Measured Proton Spectrum 127

VI. Sample Results 135

1. Measurement of stray neutron energy spectrum . . . 135

2. Unfolded Neutron Energy Spectrum 136

3. Concluding Remarks 136

Acknowledgments 148

References 149

Appendix 153

I. INTRODUCTION

High-energy accelerators give rise to complex radiation fields around biological shields, and information about these fields is essential in various radiation protection and health physics calculations. Among the components comprising the radiation field around accelerators, the charged particles and electromagnetic radiation are almost completely contained by the shielding in most cases, and the neutrons are essentially the only radiation components of the stray radiation field outside the biological shield.

The production and attenuation of neutrons inside the shielding has been discussed by Moyer[1] and Wallace[2], and the relevant collision phenomena of primary and secondary particles have been extensively treated by Metropolis[3] and later by Bertini.[4] A comprehensive report of the large shielding study by Gilbert et al.[5] discusses in detail the current understanding of the neutron fields inside the shield.

In the shield around an accelerator, large numbers of secondary particles are produced by cascade and evaporation processes. Of these particles, the neutrons above 150 MeV have the most penetrating power, due to their longer attenuation lengths, and are the major contributors to the stray neutron fields outside the shield.[6]

The quantity of primary interest in a stray neutron field is its energy distribution, which provides fundamental information for calculations of integral quantities, such as flux and dose rate, which are important in health physics work. The neutron spectrum to be measured is characterized by energy and intensity magnitudes extending over a large range, and by omnidirectionality. The present method of measuring the stray neutron spectrum is based on activation analysis, using threshold detectors.[5,7] This method has been discussed extensively in the studies made by Smith[7] and Routti.[8] A brief sketch of the method will be explained here[8]: It is based on the measurement of activities induced by high-energy neutrons in a set of detectors, thus providing information about the incident flux. The study of several

activation reactions of known energy-dependent cross sections with different threshold energies enables one to obtain the knowledge of the energy distribution of the incident neutron flux. In activation spectroscopy, measured activity in each detector is related to the neutron spectrum by the following activation equations:

$$A_j = \int_{E_{min}}^{E_{max}} \sigma_j(E_n)\,\phi\,(E_n)\,dEn, \quad j = 1, \cdots, m \tag{1.1}$$

Here A_j is the normalized saturation activity of the jth detector, $\sigma_j(E_n)$ is the corresponding activation cross section, and $\phi(E_n)$ is the neutron spectrum to be solved. Equation (1.1) is a degenerate case of the first kind of Fredholm integral equation

$$A(E') = \int_{E_{min}}^{E_{max}} K(E',E)\,\phi\,(E)dE, \tag{1.2}$$

which arises in many unfolding problems, such as the determination of the neutron spectrum $\phi(E)$ from a measured proton-recoil spectrum $A(E')$ which is related to $\phi(E)$ through the scattering kernel $K(E',E)$. So, the above method is composed of two parts: the measurement of induced activities A_j in a set of detectors and obtaining the solution from the activation equations for $\phi(E)$. In the measurement of induced activities, high-resolution semiconductor gamma-ray spectroscopy is used, and, for the solution technique for the above set of equations a numerical least squares method with matrix inversion or direct iterative least squares method is used.[8]

Neutron activation spectroscopy has the advantage or capability of covering a large range of neutron energies if a large number of detectors are used with their threshold distribution extending over a large energy range. However, in actual situations, a small number of detectors often are used, and accordingly, only a very limited

number of measured activities are available. This fact poses some difficulties in the unfolding process of searching for a solution for a neutron spectrum from a set of equations, and often requires the use of a priori physical information about the solution in addition to the measured responses. Therefore, it is desirable to develop a new kind of detector which can give more reliable information about the stray neutron spectrum around an accelerator. This work is an effort in that direction, to develop a new method to measure the neutron energy spectrum, using a set of multi-wire spark chambers and n-p converters. The outline of the new technique is as follows:

The fundamental principle of our spectrometer is based on the neutron scattering reactions with the nuclei in the hydrogeneous n-p converting material, and the detection of the tracks of the outcoming protons from the reaction using the multi-wire spark chambers with a magneto-strictive readout system. Collection of track data yields the energy spectrum of the detected protons through the range-energy relationship of protons in the spectrometer medium. This measured proton energy spectrum is related to the neutron distribution inside the spectrometer medium, and eventually to the incident neutron energy spectrum coming into the spectrometer. Using this relationship between the above two quantities the energy spectrum of the incident neutrons is unfolded numerically from the detected proton energy spectrum.

Logically this work can be divided into four parts for presentation purposes: firstly an analytical or theoretical part dealing with the relevant physics and particle transport; secondly, an experimental part dealing with the details of spectrometer setup and the attached electronics, including the proton detection method; thirdly, a data processing part dealing with definition, sorting of good events, and processing of the detected proton spectrum; and finally, the unfolding of the neutron energy spectrum from the measured proton spectrum.

Our spectrometer has been designed to measure neutrons of energy roughly between 30 MeV and 300 MeV, which is roughly the energy range below pi-meson production. For an n-p converting material,

polyethylene is used, thus supplying a proton target for the incoming neutrons. In the energy range of interest, neutrons interact with protons only through the elastic scattering mode. The cross sections for n-p scattering in this energy range are very well known, and this fact has been exploited. Even though polyethylene contains a high concentration of hydrogen atoms, it also contains carbon atoms, causing some complications in the analysis. In the above energy range, neutrons interacts with carbon nuclei both elastically and inelastically. However, the elastic scattering is so much forward peaked that one can safely assume no interactions at all,[9] and only inelastic interactions need be considered. The inelastic scattering in the above energy produces protons and neutrons through an intra-nuclear cascade process, which is a direct interaction.[10] This collision phenomenon has been extensively treated by Metropolis[3] and later Bertini,[4] and recently Bertini produced a lot of new data on intra-nuclear processes using Monte Carlo calculations.[11] At present, the information from this process is not as reliable as the n-p cross section, and the data are not presented in convenient form. However, the proton contribution from this inelastic process in the above n-p converting material is comparable to or even larger than that from the n-p scattering process, and therefore cannot be neglected. This effect has been properly incorporated in the analysis by putting n-C interaction on the same footing with the n-p cross sections, using the data in analytic form fitted by Alsmiller _et al._ to the data generated by Bertini.[4] Based on the above physics, the neutron transport and proton generation inside the spectrometer will be treated in detail in the next chapter. This will eventually lead to a basic relationship between the neutron energy spectrum and the detected proton spectrum, incorporating properly the effect of proton escaping, and will be used later in the unfolding process.

The experimental section can again be divided into three parts: the triggering, the charged particle track detecting device (i.e., spark chamber) and the data recording. Triggering is composed of three parts; the scintillators that sense the passage of charged particles, an

electronic logic box that processes the pulses from the scintillators and issues a trigger pulse only when certain conditions among the pulses are satisfied, and a high voltage pulsing system which applies the high voltage pulse across the spark chamber on reception of the trigger pulse. Next, a multi-wire spark chamber with magnetostrictive readout, which is a track locating device of charged particles, is a very versatile instrument.[12] Their widespread use in high energy physics research has made the technique of construction and use of them reliable, simple and inexpensive. Recording is accomplished by a magnetostrictive readout system,[13,14] magnetic tape and a selectric typewriter. Each part of this experimental section will be explained in detail in the third chapter.

Data processing is done on the accumulated proton track data taken from the measurement with the spectrometer, and thus generates the detected proton energy spectrum. Dealing with enormous amounts of data economically is not an easy task. There are a lot of unwanted events in the data tape coming from false triggering by γ-rays, various random errors of the machine, etc. Therefore, a good event is defined in a certain way, and only good events are extracted and used in the production of the proton energy spectrum. Gamma rays contribute to the false triggering; mainly, they come from low energy interactions of neutrons with hydrogen nuclei and from neutron interactions with carbon nuclei. Usually, in the case of using slow electronics, the effects of γ-rays are eliminated through the technique of pulse shape discrimination. We were not able to do this because we had to use fast electronics in the nanosecond range, in order to suppress the accidental coincidences. Data processing has been done with the CDC 6600 and 7600 computers; Chapter IV gives the details of the above data processing.

Chapter V will deal with the details of neutron flux unfolding procedure. The second chapter has formulated the mathematical relationship between the detected proton spectrum and the incident neutron spectrum. This will be the basic relationship which will be used in this chapter in the neutron unfolding process. However, difficulties arise

in the process due to the finite size and complicated geometrical nature of the spectrometer, as well as the highly directional nature of the incident neutrons in our energy range of interest. Proper correction for escaping protons, combined with the neutron distribution and proton generation spatial distribution, is especially difficult and almost impossible to calculate analytically. These difficulties have been overcome by the adoption of random sampling simulation of neutron transport, proton generation, and escape of proton tracks for each set of neutron and proton energies. This procedure gives the kernel matrix elements which are needed in the unfolding equation. Then the neutron energy spectrum is solved from the unfolding equation, using the detected proton spectrum. For the numerical scheme, the direct iterative least square method has been adopted, which minimizes the least square sum directly, rather than using the matrix inversion least square method.[8] The former scheme is better, due to the random nature of the given data.

Finally, the whole technique has been applied to the measurement of the stray neutron energy spectrum around the 184" cyclotron at the Lawrence Berkeley Laboratory as a sample measurement. The results and the discussions are mentioned in the final chapter.

II. THEORY

This chapter deals with the mathematics of particle behavior inside the spectrometer as the neutrons come into it, and lay the foundations for the relationship between the measured proton spectrum and the desired neutron spectrum. This relationship forms the basis of the unfolding process which follows later. Detected charged particle distribution, namely the proton distribution in space, is determined by the neutron distribution through the local proton-producing cross sections. Therefore, the behavior of neutrons inside the spectrometer is quite important in this case, and the related neutron transport phenomena is treated in the first section. The second section deals with the setup of the more specific model relevant to this case.

1. Neutron transport and proton generation

This section deals in a general sense with neutron transport and proton generation inside the region of detector volume, as the neutrons enter through the boundaries. The proton generation rate in space is then determined by the neutron distribution once it is obtained.

A neutron is a heavy, uncharged, elementary particle, and for the treatment of its transport in the medium only nuclear events need be considered among its interactions with the surrounding environment. The motion of a neutron can be described in terms of its collisions with atomic nuclei of the surrounding medium and with other freely moving neutrons; these collisions are well defined events because of known cross sections. Between such collisions, a neutron moves with a constant velocity, that is, in a straight line with a constant speed. Usually, the number of neutrons at any point in any given volume is negligibly small compared with the number of atomic nuclei present in that volume. Consequently, the mutual collisions of freely moving neutrons can be neglected, and only the collisions of neutrons with the atomic nuclei of the surrounding medium will be taken into account. Suppose we want to calculate the neutron distribution in a certain detector volume bounded by its boundary surface with free space. Then the basic quantity in neutron transport is the angular flux $\psi(\underline{r}, E, \underline{\Omega})$, which is

defined as $v\,n(\underline{r}, E, \underline{\Omega})$, where E is kinetic energy of the neutron, and $n(\underline{r}, E, \underline{\Omega})$ is the neutron density at the position $\underline{r}$ of the neutrons directed in the direction $\underline{\Omega}$ with the kinetic energy E. In the steady state situation, the angular flux at any position is governed by the following equation[15]:

$$\underline{\Omega}\cdot \mathrm{grad}\,\psi + \Sigma_{tot}(E)\,\psi = \int dE' \int d\underline{\Omega}'\, \Sigma(\underline{r}, E')c(\underline{r}, E) f(\underline{r}; E'\underline{\Omega}' \rightarrow E\underline{\Omega})\psi + S. \qquad (2\text{-}1)$$

This is the so-called transport equation or Boltzmann equation. The above equation represents the conservation of neutrons at the local point. The left hand side represents convection and reaction removal terms, and the right hand side are source terms consisting of collision and external sources. Here $\Sigma(\underline{r}, E)$ is a macroscopic total cross section of neutrons in the medium and is defined by

$$\Sigma = \sum_i N_i\, \sigma_i(E), \qquad (2\text{-}2)$$

where N_i is the number of the atoms of the ith kind per unit volume, and σ_i is the neutron reaction cross section pertaining to the various kinds of atom. $c(\underline{r}, E)$ is the average number of secondary neutrons per collision produced at $\underline{r}$ by a neutron of energy E. This quantity is important in our case in connection with neutron cascade interaction with the carbon nuclei in the medium, even though c is unity in the elastic collision of a neutron with a hydrogen nucleus. $f(\underline{r}; E'\underline{\Omega}' \rightarrow E\,\underline{\Omega})$ is the probability function of the neutron emerging from the reaction at the position $\underline{r}$ in such a way that $f(E'\underline{\Omega}' \rightarrow E\underline{\Omega})dEd\underline{\Omega}$ represents the probability that a neutron, entering a collision with velocity $v'\underline{\Omega}'$, will belong to $dEd\underline{\Omega}$ around $v\underline{\Omega}$ after the collision. $f(E'\underline{\Omega}' \rightarrow E\underline{\Omega})$ satisfies the following normalization condition:

$$\iint f(E'\underline{\Omega}' \rightarrow E\underline{\Omega})\, dEd\underline{\Omega} = 1. \qquad (2\text{-}3)$$

$f(\underset{\sim}{r}; E'\underset{\sim}{\Omega}' \rightarrow E\underset{\sim}{\Omega})$ is composed of the similar probability functions and cross sections of the interactions of the individual surrounding nuclei. More detailed expressions relevant to this case are given in the next section.

The equation (2-1) is an integro-differential equation, and boundary conditions should be specified in order to make the solution determinate. Since the neutrons are coming into the detector volume through its sides, the angular flux at the boundary should be the same as the incident neutron angular flux over all of its boundary:

$$\psi(\underset{\sim}{r}_s, E, \underset{\sim}{\Omega})\Big|_{\text{surface}} = \Psi_{inc}(E, \underset{\sim}{\Omega}) \quad \text{for} \quad \underset{\sim}{\Omega} \cdot \underset{\sim}{n} < 0. \tag{2-4}$$

where $\underset{\sim}{n}$ is an outward unit vector normal to the surface. This condition is called the "irradiation boundary condition", and has been proved to be sufficient to ensure that the problem is deterministic.[16] There is no external neutron source inside the detector volume, in this case, and the source term S in eq. (2-1) is uniformly zero.

With the above boundary condition, eq. (2-1) completely determines the neutron angular flux inside of the detector volume, and the remaining problem is to solve the above integro-differential equation.

Before we go any further, I would like to make one remark: The collision source term in eq. (2-1) contains only the neutron contribution from the reaction of neutrons. However, we are dealing with interactions in the higher energy range, and neutrons are also produced from the reaction of cascade protons[4] with the surrounding nuclei, i.e., carbon nuclei in this case. One might ask about the treatment of these protons:

A proton loses its energy in the medium through electromagnetic interactions with the surrounding atoms, and generally it has a short range for nuclear interactions along the path. Based on this reasoning, the neutron contribution from nuclear interactions of protons with surrounding nuclei has been neglected in equation (2-1).

Once the neutron flux is determined inside the detector volume from the neutron transport equation and the boundary conditions, the

next step is to calculate the proton generation rate in space and obtain the proton energy spectrum, which will be the measurable quantity by means of its range-energy relationship[17] in the medium. Protons are generated in the medium by neutron interactions that produce the protons as their reaction product. Since we are using organic material, that is, polyethylene (CH_2) as the n-p converting material inside the detector volume, the protons are generated from the interactions with the hydrogen and carbon nuclei. A neutron interacts with a hydrogen nucleus elastically, and a recoil proton is ejected with the scattered neutron. In carbon, a neutron interacts directly with the individual nucleons in the carbon nucleus, in our energy range, and protons are produced through the intranuclear cascade process as cascade particles. Note that in this case the number of outcoming protons is not conserved in the process. The above two phenomena are the main proton-producing interactions inside the medium, and only these two processes will be considered from now on. Note that the same processes are taking place in the plastic scintillator material used for triggering purposes.

Once the neutron flux is known, the total number of protons generated at each energy in the detector volume is represented mathematically by the equation:

$$\phi_p(E_p) = \int_V d\underset{\sim}{r} \int_0^\infty dE_n \int_{4\pi} d\underset{\sim}{\Omega} \int_{4\pi} d\underset{\sim}{\Omega}_p \; \Sigma_{np}(\underset{\sim}{r}, E_n)\, c_p(\underset{\sim}{r}, E_n)\, f_p(E_n \underset{\sim}{\Omega}_n \rightarrow E_p \underset{\sim}{\Omega}_p)\, \psi(\underset{\sim}{r}, E_n, \underset{\sim}{\Omega}_n), \tag{2-5}$$

where the spatial integration is over the whole detector volume and the other variables have the same meaning as previously defined. If one performs the integration over the variables $\underset{\sim}{\Omega}_p$ and $\underset{\sim}{\Omega}_n$, one obtains the more familiar equation form:

$$\phi_p(E_p) = \int_V d\underset{\sim}{r} \int_0^\infty dE_n \, \Sigma_{np}(\underset{\sim}{r}, E_n)\, c_p(\underset{\sim}{r}, E_n)\, f_p(E_n \rightarrow E_p)\, \phi_n(\underset{\sim}{r}, E_n), \tag{2-6}$$

where

$$f_p(E_n \to E_p) = \int_{4\pi} f_p(E_n, \underset{\sim}{\Omega}_n \to E_p, \underset{\sim}{\Omega}_p)\, d\underset{\sim}{\Omega}_p = \int_{-1}^{+1} d\mu_p \int_0^{2\pi} d\ _p\, f(E_n, E_p, \underset{\sim}{\Omega}_n, \underset{\sim}{\Omega}_p), \qquad (2\text{-}7)$$

and $$\phi_n(\underset{\sim}{r}, E_n) = \int_{4\pi} \psi(\underset{\sim}{r}, E_n, \underset{\sim}{\Omega})\, d\underset{\sim}{\Omega}_n = \int_{-1}^{+1} d\mu_n \int_0^{2\pi} d\varphi_n\, \psi(\underset{\sim}{r}, E_n, \mu_n, \varphi_n). \qquad (2\text{-}8)$$

In the above step the $\underset{\sim}{\Omega}_p$ variable is integrated first and the $\underset{\sim}{\Omega}_n$ integration later. $\phi_p(E_p)$ is the proton energy flux, and can be measured experimentally in the steady state situation by the measurement of the proton path lengths detected inside the detector volume, and by converting them into proton energies using the range-energy relationship for the medium. The proton energy flux $\phi_p(E_p)$ in equation (2-6) is only the generation rate of protons of energy E_p in the detector volume just before the formation of a track representing its energy. However, in an actual situation the detector size is small, and naturally there are many protons crossing the boundary. Therefore, a correction for the protons escaping through the detector boundary should be made in a practical measurement procedure.

A slight variation of equation (2-6) gives the equation which is used in the nuclear emulsion case for measuring the low energy neutron flux.[18] Usually an emulsion plate is very thin compared to the neutron mean free path in the plate, and the neutron attenuation inside the plate is negligibly small. This means that neutron flux inside the plate is uniform and equal to the flux outside. Another simplification in this case comes from the fact that only n-p elastic scattering need be considered in the lower energy region. Therefore, in equation (2-6) the position variable drops out and c becomes equal to one. Equation (2-6) then becomes:

$$N_p(E_p) = \int_0^{\infty} dE_n\, \Sigma_H(E_n)\, f_p(E_n, E_p)\, \phi_n(E_n), \qquad (2\text{-}9)$$

where $N_p(E_p)$ is the measured proton spectrum. One more simplification comes from the fact that the n-p elastic scattering cross section is isotropic in the center of mass system in this energy range. This

gives a simpler form of $f_p(E_n \rightarrow E_p)$ due to the one-to-one relationship between the recoil angle in the CM system and the Laboratory recoil proton energy by scattering kinematics:

$$f(E_n \rightarrow E_p) = \frac{1}{E_n} . \tag{2-10}$$

This gives the following form of equation from (2-9):

$$N_p(E_p) = \int_{E_p}^{\infty} dE_n \frac{\Sigma_H(E_n)}{E_n} \phi_n(E_n), \tag{2-11}$$

and the formal neutron flux expression can be obtained by only one differentiation:

$$\phi(E_n) = - \frac{1}{\Sigma_H(E)} \frac{d N_p(E)}{dE} . \tag{2-12}$$

Therefore, the neutron energy spectrum is obtained by differentiation of the measured proton energy spectrum. Corrections for the escaping protons are usually based on the isotropic flux at low neutron energies. The same model could also be applied in the measurement of neutron spectra using an organic scintillator, except for the light production.[19]

Returning to our problem, let us discuss briefly the difference tween our situation and the nuclear emulsion case. First of all, our spectrometer is quite large, and the material thickness in an average direction is comparable to as much as half of a mean free path or less in most of the energy range, even though the mean free path is relatively long at those energy of interest. See figures 1-5. This means that the neutron attenuation is not negligible in our detector volume and simply cannot be ignored. Therefore, the neutron flux inside the volume is neither uniform nor equal to the incoming neutron flux on the detector boundary, which is the quantity which we eventually want to know. This fact should be kept in mind. The second distinction

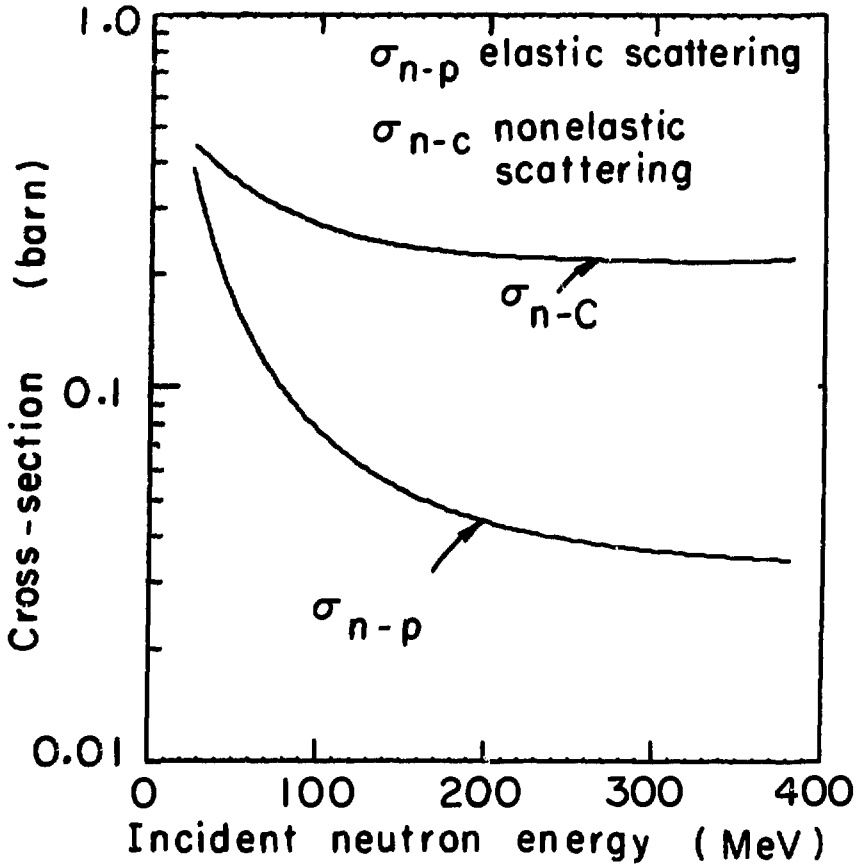

XBL7212-4957

Fig. 1. Microscopic cross sections of n-p and n-c interactions.

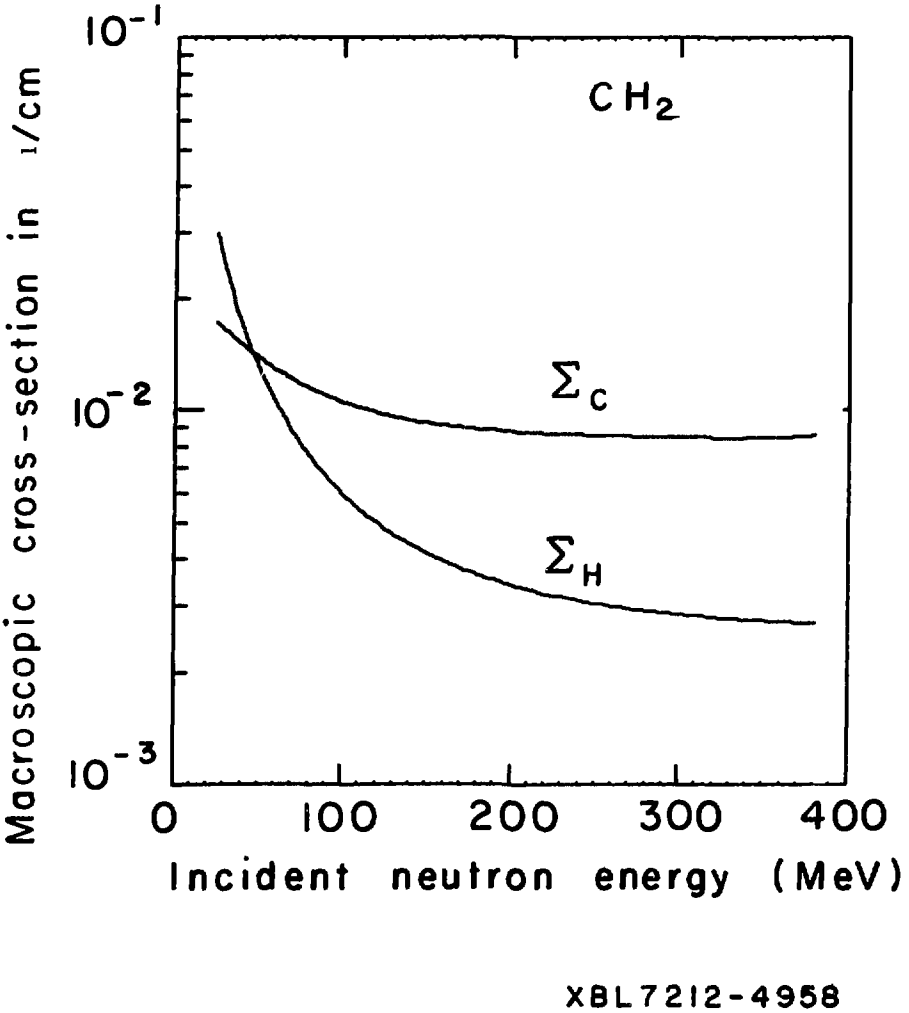

XBL7212-4958

Fig. 2. Macroscopic cross sections of polyethylene (CH_2).

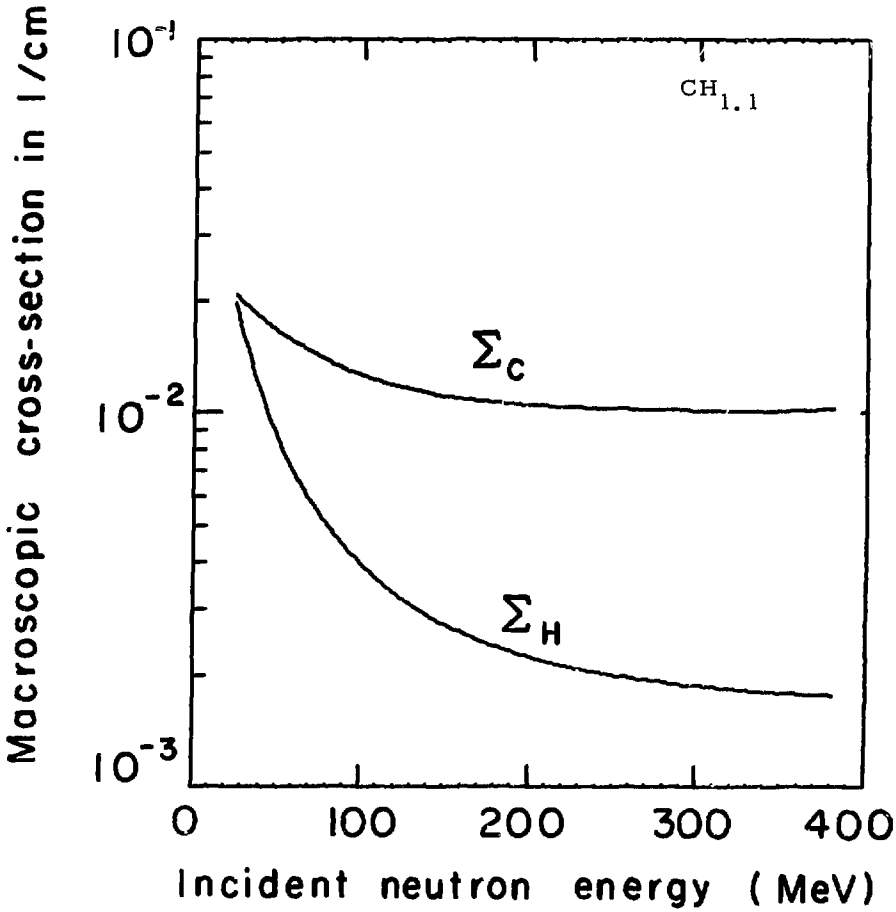

XBL7212-4956

Fig. 3. Macroscopic cross sections of a plastic scintillator (Pilot B).

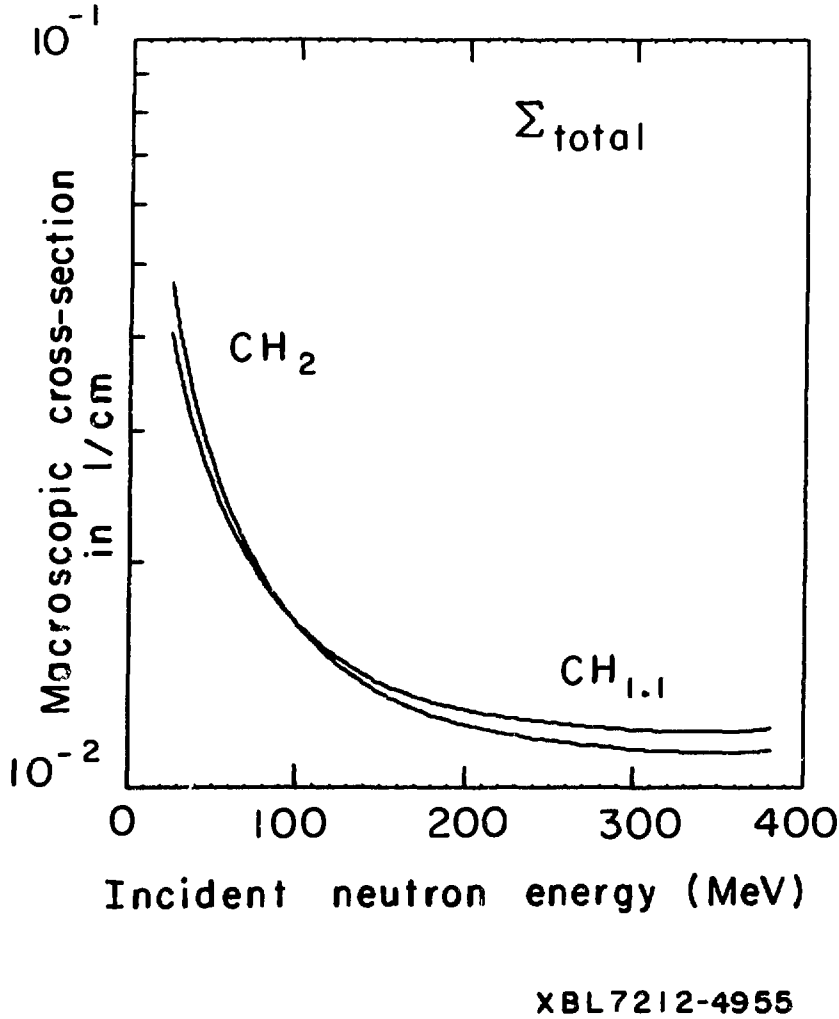

XBL7212-4955

Fig. 4. Total macroscopic cross sections of polyethylene and a plastic scintillator (Pilot B).

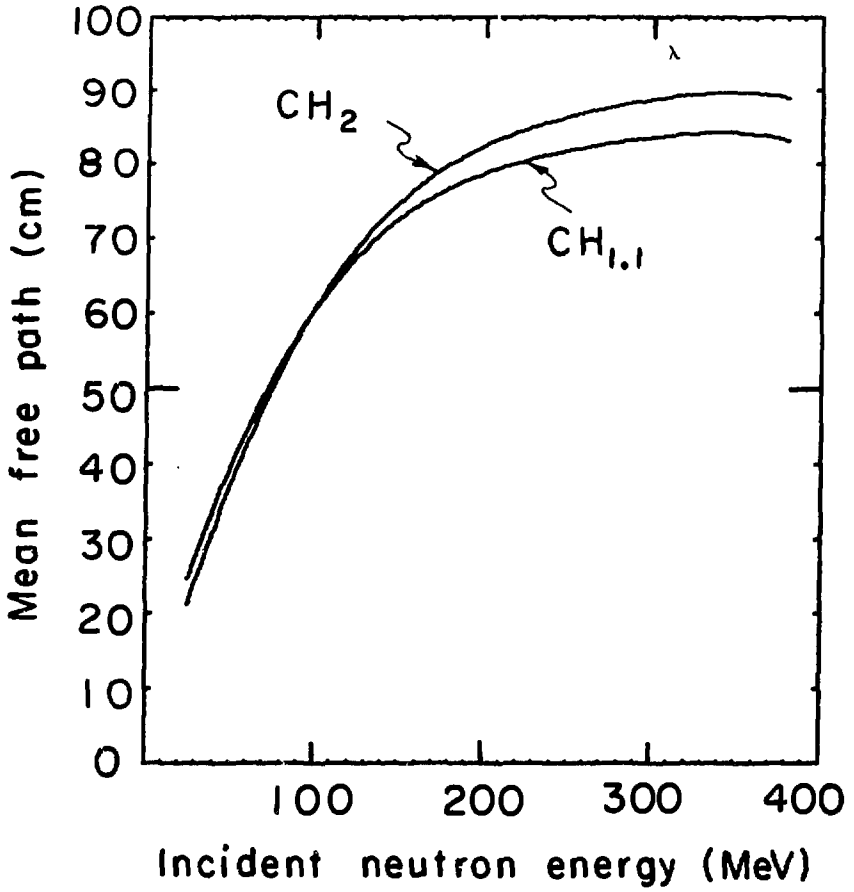

XBL7212-4954

Fig. 5. Mean free path of polyethylene (CH_2) and a plastic scintillator ($CH_{1.1}$).

comes from the fact that the proton range is relatively quite long, compared to the detector size, in the energy region we are covering. See figure 6. Consequently, the problem of escaping protons is more pronounced and, combined with the complicated nature of the detector volume (multi-medium, multi-region problem), makes a simple analytical correction for escaping protons almost impossible. The third distinction is in the highly directional nature of the surrounding neutron flux environment that forms the incident neutron flux to the detector volume. It should be noted that actually we are more interested in the neutron energy flux, which has been integrated over the solid angle, than in the directional neutron flux, which is a more basic quantity. All of the above difficulties are considered, and in the next section an effort is made to relate the incident neutron spectrum with the measured proton energy spectrum in our situation, based on some simplifying assumptions.

Returning to the neutron transport problem, the equation (2-1) does not show much about the particle processes inside the detector volume, and a purely mathematical effort to solve the equation is neither easy nor productive in this case. The goal of this section is to describe the particle behavior in an analytical way, and thereby gain an insight into the transport phenomena.

If we change our angle slightly and see the problem from the standpoint of pure neutron transport or diffusion, we are dealing with a transport medium which is comparable to or less than the mean free path of the neutrons. This means that many of neutrons will escape the detector volume before they make many interactions, and the part that forms the major fraction of the neutrons inside of the detector volume will be composed of unscattered incoming neutrons, plus the neutrons from the first few collisions. In this sense, the decomposition of neutron flux inside the detector volume, in terms of the incoming and multiply-scattered neutron fluxes, is very informative in our case; this will be developed in the remainder of this section, leading evenually to the integral representation of the neutron transport.

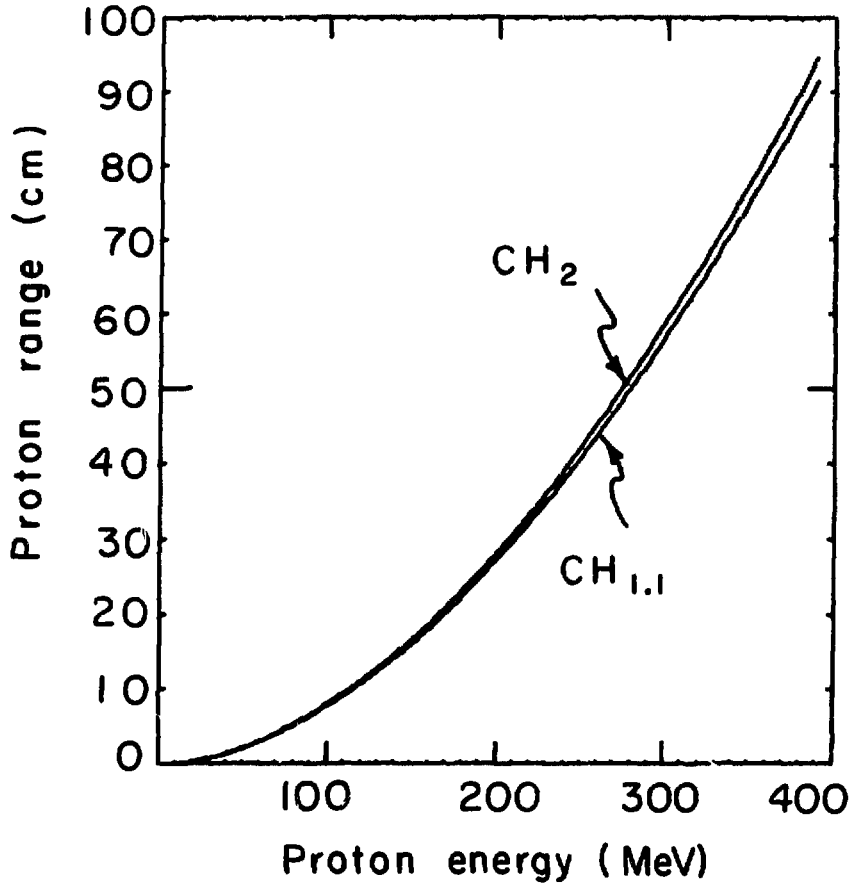

XBL7212-4953

Fig. 6. Range of protons in polyethylene (CH_2) and a plastic scintillator ($CH_{1.1}$).

Consider a volume V and neutrons coming into it as shown in figure 7.

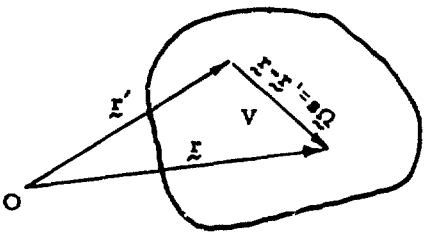

Fig. 7.

Neutrons arriving at the boundary from outside will be called incident neutrons or surface source neutrons, and will be represented as Ψ_{inc}. As far as the neutron distribution within the volume is concerned, it does not make any difference whether the boundary condition is defined as the incident neutron flux at the boundary or as the surface source distribution, but with no neutrons incident from the outside. The neutrons at the position $\underset{\sim}{r}$, originating from incident neutrons that did not make any collisions inside the volume V, are called unscattered neutrons and are represented, according to the exponential attenuation law:

$$\psi_0(\underset{\sim}{r},E,\underset{\sim}{\Omega}) = \Psi_{inc}\Big|_{surface} \cdot e^{-\Sigma_t(\underset{\sim}{r}',E)\,|\underset{\sim}{r}-\underset{\sim}{r}'|} \text{ (homo. case)}, \qquad (2\text{-}13)$$

or more generally in a non-homogeneous medium:

$$= \Psi_{inc}\Big|_{surface} \cdot e^{-\int_0^s \Sigma_t(s,E)ds}, \qquad (2\text{-}14)$$

where s is measured from the boundary to the point $\underset{\sim}{r}$, in this particular case, in the direction of neutron travel. The integral in the exponent is usually called the "neutron optical path length at energy E", and represented as $\tau(s,E)$ or $\tau(|\underset{\sim}{r}-\underset{\sim}{r}'|,E)$. Those coming from outside that have scattered only once in the volume element and have not been

absorbed are named "singly scattered neutrons", and can be written:

$$\psi_1(\underset{\sim}{r},E,\underset{\sim}{\Omega}) = \int_{\text{along } s\,\underset{\sim}{\Omega}} ds\, e^{-\tau(|\underset{\sim}{r}-\underset{\sim}{r}'|,E)} \int_0^\infty dE' \int_{4\pi} d\Omega' \psi_0(s,E',\underset{\sim}{\Omega}')\Sigma_t(E')\, c(E) f(E'\underset{\sim}{\Omega}' \to E\underset{\sim}{\Omega}). \tag{2-15}$$

Higher generations of scattered neutrons are analogously named, so that the n<u>th</u> scattered neutron flux is generally represented as:

$$\psi_n(\underset{\sim}{r},E,\underset{\sim}{\Omega}) = \int_{\text{along } s\underset{\sim}{\Omega}} ds\, e^{-\tau(|\underset{\sim}{r}-\underset{\sim}{r}'|,E)} \int_0^\infty dE' \int_{4\pi} d\Omega' \psi_{n-1}(s,E',\underset{\sim}{\Omega}')\Sigma_t(E')\, c(E) f(E'\underset{\sim}{\Omega}' \to E\underset{\sim}{\Omega}), \tag{2-16}$$

and the integration over $\underset{\sim}{\Omega}$ using the relations,

$$\int_{4\pi} \psi(\underset{\sim}{r},E,\underset{\sim}{\Omega})\, d\underset{\sim}{\Omega} \equiv \phi(\underset{\sim}{r},E) \tag{2-17}$$

and

$$ds\, d\Omega = \frac{d\underset{\sim}{r}'}{|\underset{\sim}{r}-\underset{\sim}{r}'|^2} . \tag{2-18}$$

gives the neutron-energy flux at each local point

$$\phi_n(\underset{\sim}{r},E) = \int \frac{d\underset{\sim}{r}'}{|\underset{\sim}{r}-\underset{\sim}{r}'|^2} e^{-\tau(|\underset{\sim}{r}-\underset{\sim}{r}'|,E)} \int_0^\infty dE' \int_{4\pi} d\Omega' \psi_{n-1}(\underset{\sim}{r}',E',\underset{\sim}{\Omega}')\Sigma_t(E')\, c(E) f(E' \to E, \underset{\sim}{\Omega}' \to \underset{\sim}{\Omega}). \tag{2-19}$$

The neutron flux in the volume is made up of the unscattered and multiply-scattered neutrons exclusive each other; the total neutron flux is the sum of all of these terms:

$$\begin{aligned} \psi(\underset{\sim}{r},E,\underset{\sim}{\Omega}) &= \psi_0(\underset{\sim}{r},E,\underset{\sim}{\Omega}) + \psi_1(\underset{\sim}{r},E,\underset{\sim}{\Omega}) + \cdots, \\ &= \sum_{n=0}^{\infty} \psi_n(\underset{\sim}{r},E,\underset{\sim}{\Omega}), \end{aligned} \tag{2-20}$$

and
$$\phi(\underset{\sim}{r},E) = \phi_0(\underset{\sim}{r},E) + \phi_1(\underset{\sim}{r},E) + \cdots, \qquad (2\text{-}21)$$
$$= \sum_{n=0}^{\infty} \phi_n(\underset{\sim}{r},E).$$

The equation (2-20) can be thought of as a formal solution of the following integral equation:

$$\psi(\underset{\sim}{r},E,\underset{\sim}{\Omega}) = \int ds \int dE' \int d\underset{\sim}{\Omega}' \left\{ \Sigma_t(\underset{\sim}{r}',E')\psi(\underset{\sim}{r}',E',\underset{\sim}{\Omega}')c(E)f(E',\underset{\sim}{\Omega}' \rightarrow E,\underset{\sim}{\Omega}) \right\} e^{-\tau(|\underset{\sim}{r}-\underset{\sim}{r}'|,E)} \qquad (2\text{-}22)$$

In fact, this is an integral representation of the transport equation, and the equivalence of this equation with equation (2-1) can be shown by integration of equation (2-1) along the path of particle travel.[15, 16]

In situations where the detector size is less than or comparable to the mean free path, as in our case, essentially the unscattered and the first few multiply-scattered neutron fluxes form most of the total neutron flux, and the rest of the scattered fluxes are negligibly small, due to the large neutron escape probability because of the small size of the detector. Therefore, only the first few fluxes need be considered in the analysis, and this fact will be exploited in the future approximating processes.

2. The Model

The goal of this chapter is to relate the incident neutron flux to the measured neutron spectrum.

The source that forms the neutrons inside the detector volume is the flux of incoming neutrons, and this is the quantity which we eventually want to know. The neutrons inside the detector volume generate protons through interactions with hydrogen and carbon nuclei. These protons have a certain length of travel depending on their energy in the medium, and leave detectable tracks along their path. We measure these tracks experimentally, and ultimately we obtain the detected proton energy spectrum. Therefore the basic task is to relate the above two quantities, with respect to our specific detector geometry and material.

Our spectrometer was set up as shown in figure 8. In order to provide the target nuclei for the incoming neutrons to generate the protons, 1 polyethylene sheet of a specific thickness was used as the converting material, and spark chambers to detect the proton tracks were inserted between the polyethylene sheets. In this case the n-p converting material also acts as an energy-degrading medium for the generated protons, and decides their ranges. Also, very thin plastic scintillators were sandwiched between the polyethylene and the spark chambers for the purpose of sensing the generated protons and to trigger the high voltage to the spark chambers whenever charged particles were present. The spark chambers were filled to one atmosphere pressure with neon gas and isolated by very thin mylar windows. The density of gas is very low compared with that of a solid, and the space occupied by the chambers will be regarded as empty space for the analysis of particle transport. The analysis will be done on the geometry specified above.

We shall start with the expression for proton generation and relate it to the incident neutron flux, which is the desired quantity. To simplify the analysis, we can think of the spectrometer as made up of one medium, namely polyethylene. For the plastic scintillators, we can use the effective equivalent nuclear parameters. Then only the space occupied by n-p converter material has non-vanishing nuclear parameters, and the nuclear properties are uniform in this medium. We can assume that n-p interactions happen only in this space, and space-dependency of the macroscopic nuclear parameters disappears. Equation (2-6), which represents the proton generation then becomes:

$$\phi_p(E_p) = \int_{V_m} d\underset{\sim}{r} \int_0^\infty dE_n \, \Sigma_{np}(E_n) \, c_p(E_n) \, f_p(E_n \rightarrow E_p) \, \phi_n(\underset{\sim}{r}, E_n), \qquad (2\text{-}23)$$

where V_m means the space occupied by the n-p converting medium. The medium consists of hydrogen and carbon atoms; protons are produced from the n-p elastic scattering with hydrogen and the inelastic cascade reaction with carbon nuclei.

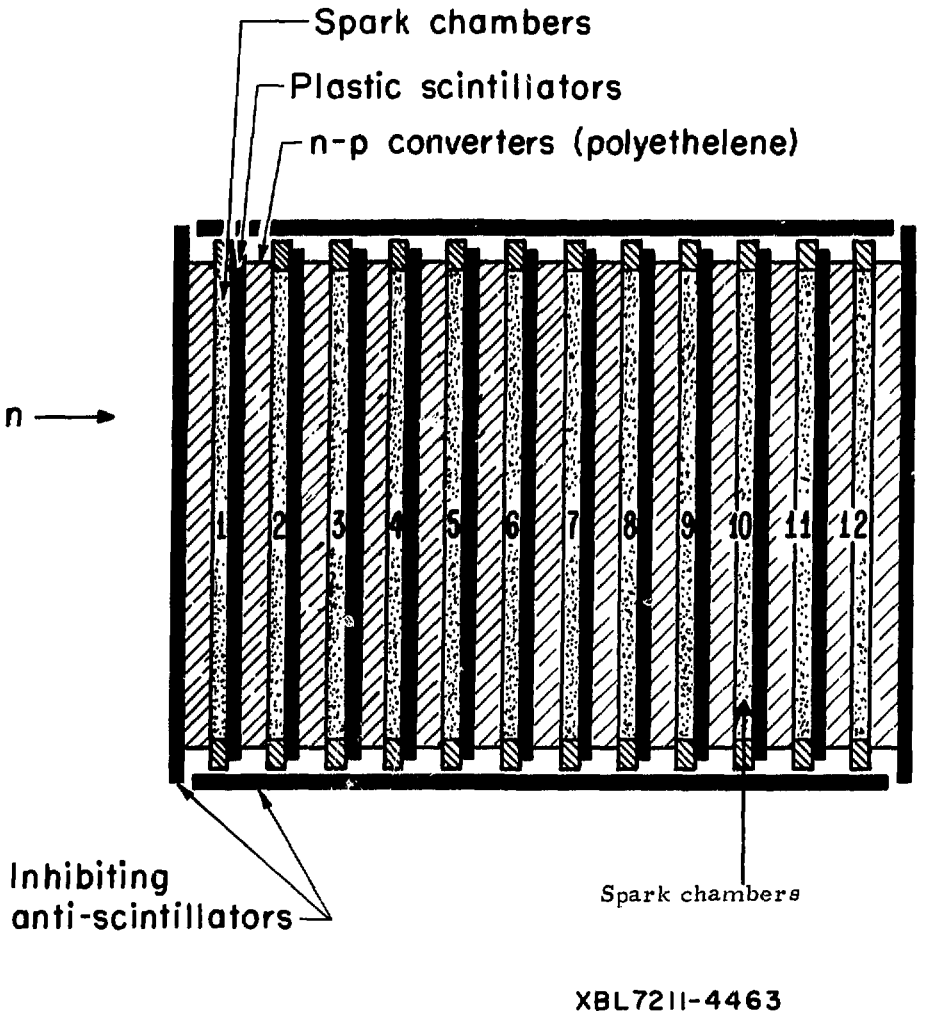

Fig. 8. Spectrometer setup.

Then

$$\Sigma_{np}(E_n) = N_H \sigma_{H,el}(E_n) + N_c \sigma_{c,inel}(E_n) \qquad (2\text{-}24)$$

and

$$\Sigma_{np}(E_n) c_p(E_n) f_p(E_n \rightarrow E_p) = N_H \sigma_{H,el}(E_n) f_H(E_n \rightarrow E_p) + N_c c_p(E_n) \sigma_{c,inel}(E_n) f_C(E_n \rightarrow E_p) \qquad (2\text{-}25)$$

where $c_p(E_n)$ is the average number of emerging proton secondaries per interaction with a carbon nucleus; this number is generally energy-dependent.

The variation of $\sigma_{H,el}(E_n)$ and $\sigma_{c,inel}(E_n)$ with incident energy are shown in figure 1 and the macroscopic cross section in polyethylene is shown in figure 4.

In elastic scattering the neutron scattering angle or proton recoil angle is associated by scattering kinematics with the kinetic energies of the scattered neutron and proton in a one-to-one relationship. Therefore, the energy distributions of the emergent particles are decided by the emergent angular distribution from the reaction. Note that the above statement is true only in elastic scattering. Usually, the emergent angular distribution from a reaction is given in the center of mass system, and the energy distribution in elastic scattering should be referred to it.

The n-p scattering cross section is isotropic in the CM system at low energy below roughly 10 MeV, and as the incident neutron energy increase, it becomes symmetric about 90°. This is true up to roughly 42 MeV. The region is well represented by Gammel's formula[20]:

$$\sigma_{n,p}(\mu_c, E_n) = \frac{\sigma_{tot}(E_n)}{4\pi} \frac{1 + b\mu_c^2}{1 + b/3} \text{ barn/ster.}, \qquad (2\text{-}26)$$

where

$$b = 2\left(\frac{E_n}{90}\right)^2$$

and

$$\sigma_{tot}(E_n) = \frac{3\pi}{A} + \frac{\pi}{B}, \quad \text{in barns} \qquad (2\text{-}27)$$

with

$$A = 1.206\,E_n + (-1.86 + 0.0941\,E_n + 0.0001306\,E_n^{\,2})^2$$

$$B = 1.206\,E_n + (\,0.4223 + 0.13\,E_n)^2.$$

The terms including b are correction factors accounting for the departure from isotropy at higher energies. Here μ_c is the cosine of the neutron scattering angle in the CM system, E_n is the kinetic energy of the incident neutron, in MeV, in the Laboratory system, and the differential cross section is in barns/steradian. The above equation can be converted to one for the differential cross section, as a function of emergent proton energy, using the following two kinematical relationships[21]:

$$\sigma_{np}(\mu_c, E_n)\, 2\pi\, d\mu_c = \sigma_{np}(E_n, E_p) dE_p \tag{2-28}$$

and

$$\mu_c = 1 - 2\,\frac{E_p}{E_n}\,, \tag{2-29}$$

where E_p is the recoil proton energy in MeV in the Laboratory system. Then:

$$\sigma_{np}(E_n, E_p) = \sigma_{np}(\mu_c, E_n)\, 2\pi \left|\frac{d\mu_c}{dE_p}\right|$$

$$= \sigma_{np}(\mu_c, E_n) \cdot 2\pi \cdot \frac{2}{E_n}$$

$$= \frac{\sigma_{tot}(E_n)}{E_n}\left[\frac{1 + b\left(1 - 2\,\frac{E_p}{E_n}\right)^2}{1 + b/3}\right] H(E_n - E_p), \tag{2-30}$$

where $H(E_n - E_p)$ is a heaviside function, defined as

$$H(E_n - E_p) = 1 \quad \text{for} \quad E_p \leq E_n$$

$$= 0 \quad \text{for} \quad E_p \leq E_n.$$

Above 42 MeV, the differential cross section is not symmetrical about 90°, and the expression above is not a good approximation. For the energy range up to 300 MeV, the currently available experimental data have been fitted, using the following expression by the author and his collaborators.

$$\sigma_{np}(\cos\theta_c, E_n) = \frac{\sigma_{tot}(E_n)}{4\pi}\left[A\left(\frac{1 + 2\left(\frac{E_n}{90}\right)\cos^2\theta_c}{1 + \frac{2}{3}\left(\frac{E_n}{90}\right)^2}\right) + B(\cos^3\theta_c)\right. \tag{2-31}$$

$$\left. + C(\cos^4\theta_c) + D(\sin\theta) + E(\sin 2\theta) + F(\sin 4\theta_c) + G\right],$$

where Metropolis formula has been used for $\sigma_{tot}(E_n)$:

$$\sigma_{tot}(E_n) = \frac{34.10}{\beta^2} - \frac{82.2}{\beta} + 82.2 \qquad \text{in mb,} \tag{2-32}$$

with $\beta = \frac{v}{c}$ in the Laboratory system.

A, B, C, D, E, F and G are fitting parameters. Details of additional terms and fitting procedure will be explained in a later chapter.

As for the in-elastic nuclear reaction with carbon nuclei, analytic fits, obtained by the method of linear least squares, to the intranuclear-cascade data generated by H. W. Bertini will be used.[4, 11]

The basic assumption of the method employed in the intranuclear-cascade calculation is that the interactions of high-energy particles with the nucleus can be represented by free particle-particle collisions inside the nucleus, an approach first suggested by Serber.[10] The justification for the assumption is that the wave length of the incident particle is of the order of the internuclear distance ($\sim 10^{-13}$ cm). The deBroglie wave-length of nucleon divided by 2π, $\lambda\!\!\!^-$, at a few energies is illustrated:[4]

Nucleon Energy(MeV)	20	100	500
$\lambda\!\!\!^-$ (cm)	1.02×10^{-13}	4.45×10^{-14}	1.82×10^{-14}.

The physical process that can be approximately described by free-particle collisions within the nucleus is called the cascade. On the basis

of this assumption, one can calculate the reaction with the nucleus by determining the life history of every particle that becomes involved in the individual particle-particle collisions occurring within the nucleus. The point of collision, the type of collision, the momentum of the struck nucleon, and the scattering angles for each collision are determined by statistical sampling techniques. Free-particle experimental data are used whenever cross section data are required.

The basic approach on this model was suggested by Serber, and Goldberger was one of the first to carry out calculations based on his suggestion. His work was done with hand calculations. Later more complete and detailed three-dimensional treatment was performed by Metropolis et al.[3] by assuming the constant nucleon density within the nucleus and a zero temperature Fermi energy distribution to represent the energy distribution of the nucleons inside the nucleus. The latest and most complete calculation of this type is that of Bertini[4] using more realistic nuclear model, recent cross-section data, and an exact statistical sampling technique. Extensive comparisons with experiment were also made by him and the calculations are claimed to reproduce most of the experimental data for the cascade process within or close to the experimental error.

Analytic fits to Bertini's data has been obtained by Alsmiller et al.,[7] and it is these fits that are going to be used in our case. However it is to be noted that the analytic expressions give the energy spectra of emitted cascade protons and neutrons averaged over large angular intervals, and it is these average data which are used; that is, the differential cross section for the cascade protons and neutrons is taken to be constant over the angular intervals 0 to 30, 30 to 60, 60 to 90, and 90 to 180. It is by no means certain that this is an adequate representation of the differential cross section. More details of fitting formula used will be given in a later chapter.

Returning to equation (2-23), we see that it represents the proton generation rate with none escaping. In another words, if we suppose that left side represents the detected proton spectrum, equation (2-23) is true only for an infinite detector. In a practical situation, the

detector size is finite, and the protons escaping out of the detector volume should be taken into consideration in the above expression. The proton-escaping effect is local, and depends on the relationship between the generated proton energy and its range in the medium. Therefore, in the case of finite detector, equation (2-23) should contain a local energy-dependent parameter, $d(\underset{\sim}{r}, E_p)$, in it accounting for the fraction of the protons detected out of the total number of protons generated locally. Then equation (2-23) becomes:

$$\phi_p(E_p) = \int_{V_m} d\underset{\sim}{r} \int_0^\infty dE_n \, \Sigma_{np}(E_n) \, c_p(E_n) \, f_p(E_n, E_p) \, \phi_n(\underset{\sim}{r}, E_n) \, d(\underset{\sim}{r}, E_p). \qquad (2\text{-}33)$$

This represents the proton generation rate being detected inside the detector volume, without escaping out of the finite size detector. Here we rearrange the equation (2-35) slightly:

$$\phi_p(E_p) = \int_{E_p}^\infty dE_n \; c_p(E_n) \, f_p(E_n, E_p) \left[\int_{V_m} d\underset{\sim}{r} \, \Sigma_{np}(E_n) \, \phi_n(\underset{\sim}{r}, E_n) d(\underset{\sim}{r}, E_p) \right], \qquad (2\text{-}34)$$

and pause a moment to analyze the physical meaning of each term under the space integral. Note that the lower limit of the energy integral has been changed to E_p, due to the physical fact that protons of E_p are contributed only from the neutron flux at higher-energy. $\Sigma_{np}(E_n)\phi_n(\underset{\sim}{r}, E_n)$ is the total neutron reaction or collision rate per unit time per unit volume at the position $\underset{\sim}{r}$, irrespective of the generated proton energy, and $d(\underset{\sim}{r}, E_p)$ is the detection rate of the protons of energy E_p generated at the position $\underset{\sim}{r}$. All of the protons generated at the position $\underset{\sim}{r}$ are distributed in energy according to the probability law $f_p(E_n, E_p)$, $c_p(E_n)$ being the number of protons generated per collision.

The left side is the total sum of protons of energy E_p generated and detected inside the detector. Let's focus our attention for the time being on the composition of this quantity. Protons are generated from the collisions with neutrons, and the neutrons at each point in space can be decomposed into the mutually exclusive unscattered and multiply-scattered

neutrons, as was shown in the previous section. Consequently, the generated protons can also be labelled or decomposed into the protons generated from reactions with the unscattered neutrons, singly scattered neutrons, doubly scattered neutrons, and so on. Then each class of protons can be represented as:

$$\phi_i(E_p) = \int_{E_p}^{\infty} dE_n\, c_p(E_n)\, f_p(E_n, E_p) \left[\int_{V_m} d\underset{\sim}{r}\, \Sigma_{np}(E_n)\, \phi_i(\underset{\sim}{r}, E_n)\, d(\underset{\sim}{r}, E_p) \right], \quad (2\text{-}35)$$

and equation (2-34) becomes:

$$\phi_p(E_p) = \sum_{i=0}^{\infty} \phi_i(E_p) = \int_{E_p}^{\infty} dE_n\, c_p(E_n)\, f_p(E_n, E_p) \left[\int_{V_m} d\underset{\sim}{r}\, \Sigma_{np}(E_n) \left(\sum_{i=0}^{\infty} \phi_i(\underset{\sim}{r}, E_n) \right) d(\underset{\sim}{r}, E_p) \right]$$

$$= \sum_{i=0}^{\infty} \int_{E_p}^{\infty} dE_n\, c_p(E_n)\, f_p(E_n, E_p) \left[\int_{V_m} d\underset{\sim}{r}\, \Sigma_{np}(E_n)\, \phi_i(\underset{\sim}{r}, E_n)\, d(\underset{\sim}{r}, E_p) \right]. \quad (2\text{-}36)$$

One should note that for all interactions or proton generations neutrons come out from the reactions, either as scattered neutrons or cascade neutrons, and these neutrons either make additional collisions in the n-p converting medium and eventually escape, or escape directly out of the detector volume without making any further collision. From the experimental point of view, we are interested in the events that make a single collision, or more specifically, a single track inside of the detector volume. It is easy to see that these kinds of interactions have the highest chance of occurrence in the detector, since the detector size is small compared with the mean free path, and escape is a dominant phenomenon. One should also remember that the resolving time of a spark chamber is quite long compared to the mean time spent by a neutron between collisions. The result is that most of the multiple scattering events are recorded as a single event. At any rate, one can again decompose the previously defined class of collisions, such

that the emergent neutrons make no collision before leaving the detector, make one collision before leaving, or two collisions before leaving, etc. Since we are interested in the single track events in the detector, we are interested in the protons that are generated from interactions with unscattered neutrons and the emergent neutrons from the reaction that leave the detector without further scattering. Then the probability, that an emergent neutron from an interaction does not make any further collision before escaping, should be contained in the first term of equation (2-36), and this can be done by attaching the additional probability to $d(\underset{\sim}{r}, E_p)$, denoting the new parameter by $d_0(\underset{\sim}{r}, E_p)$. Then the protons we are interested in can be represented as

$$\phi_0(E_p) = \int_{E_p}^{\infty} dE_n \, f_p(E_n, E_p) \int_{V_m} d\underset{\sim}{r} \, \Sigma_{np}(E_n) \, \phi_0(\underset{\sim}{r}, E_n) \, d_0(\underset{\sim}{r}, E_p), \qquad (2\text{-}37)$$

where $c_p(E_n)$ has been set equal to one, since we are also interested in the interaction producing only one proton from the reaction.

In order to illustrate the above analysis and to give some feeling about the relative magnitude of the unscattered and multiply-scattered neutron flux, the following example of a simple idealized one-dimensional detector will be given: Suppose we have a one-dimensional detector, whose thickness is roughly one third of the mean free path, $\lambda = \frac{1}{\Sigma}$, and the neutrons are incident on one side normal to the surface. Let's assume that the neutron scattering law can be approximated with the straight-ahead emergent direction, namely, that neutrons don't change direction and energy after collision. In this case, we calculate the unscattered and multiply-scattered neutron fluxes and their fractions in which case their emergent neutrons leave the detector without any further collisions.

See the figure below.

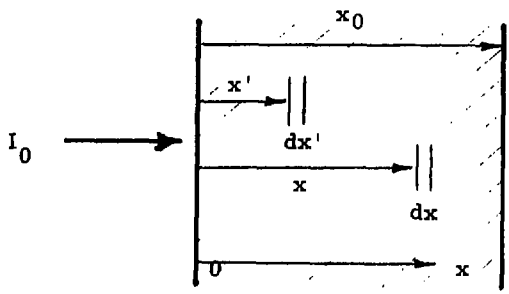

Fig. 9.

Obviously, the unscattered flux at the position x is

$$\phi_0(x) = I_0 e^{-\Sigma x}. \tag{2-38}$$

The singly-scattered flux is made up of neutrons that make one and only one collision before reaching the position x. Hence, the singly scattered neutron flux is made by the sum of the multiplications of two probabilities, i.e., the probability that the neutron will make one collision at an arbitrary point at the position x' before reaching x, and the probability that the scattered neutron will reach the position x without collision. Mathematically this is

$$\phi_1(x) = \int_0^x (I_0 e^{-\Sigma x'} \Sigma \, dx') e^{-\Sigma(x-x')}$$

$$= I_0 (\Sigma x) e^{-\Sigma x}. \tag{2-39}$$

Similarly the doubly-scattered neutron flux is formed from the interactions of the singly-scattered neutrons before reaching x, and we get

$$\phi_2(x) = \int_0^x I_0(\Sigma x')\, e^{-\Sigma x'}\, \Sigma\, dx'\, e^{-\Sigma(x-x')}$$

$$= e^{-\Sigma x} \int_0^x I_0(\Sigma x')(\Sigma\, dx') = I_0 \frac{(\Sigma x)^2}{2} e^{-\Sigma x}. \tag{2-40}$$

Generally, the i-times scattered neutron flux is

$$\phi_i(x) = I_0 \frac{(\Sigma x)^i}{i!} e^{-\Sigma x}, \tag{2-41}$$

and the sum of these fluxes is

$$\sum_{i=0}^{\infty} \phi_i = \sum_{i=0}^{\infty} I_0 \frac{(\Sigma x)^i}{i!} e^{-\Sigma x} = I_0 e^{-\Sigma x} \cdot \left(\sum_{i=0}^{\infty} \frac{(\Sigma x)^i}{i!} \right) = I_0 e^{-\Sigma x} \cdot e^{\Sigma x} = I_0,$$

$$\text{i.e.,} \quad \sum_{i=0}^{\infty} \phi_i = I_0, \tag{2-42}$$

which is the natural result from the physical point of view. One also can expect that each $\phi_i(x)$ has peaks at the position $i\lambda$.

The events, in which the scattered neutrons from the interactions with the unscattered and multiply-scattered neutrons leave the detector without any further collisions, are obtained by multiplying the above fluxes by the non-collision probability in the remainder of the path, $e^{-\Sigma(x_0-x)}$ and Σ, giving

$$\phi_i(x)\, \Sigma\, e^{-\Sigma(x_0-x)} = I_0 \frac{(\Sigma x)^i}{i!} e^{-\Sigma x} \cdot \Sigma\, e^{-\Sigma(x_0-x)}$$

$$= I_0 e^{-\Sigma x_0}\, \Sigma \frac{(\Sigma x)^i}{i!}. \tag{2-43}$$

The above multiply-scattered neutron fluxes $\phi_i(x)$, and their collision

rate producing scattered neutrons that leave the detector without collisions, have been plotted in figures 10 and 11. In order to get the fraction of detected non-escaping protons from the above fluxes, one should calculate the detection probability of protons at the position x, and that should be multiplied by the above collision rate. In the actual case, the scattering tneds to give a forward-peaked proton distribution of emergent angles, and this has the effect of reducing the peak on the right hand side of the equation representing the multiply-scattered fluxes. The figure shows that, as the detector size decreases, the effect of the unscattered neutron flux becomes more and more pronounced, giving the multiply-scattered neutrons negligible importance.

Returning again to our original track, let us consider the angular nature of the incoming neutrons to the detector. Around the high energy accelerators, the particles come from the shielding material mainly as secondaries from reactions with nuclei of the atoms comprising the shielding material, when the very high energy particles from the target impinge on it. The reactions that occur inside the shield, in the above energy range, are cascade reactions, and have a relatively long attenuation length. Additionally, the reaction products from the cascade reaction emerge with a very high peak in the forward direction, and this fact tends to maintain the highly-directional nature of the neutron flux, even after much attenuation of the original flux, inside the shield. Therefore, even at the time the remaining secondaries emerge from the shielding material to form the stray neutrons around the accelerator, emerging neutrons still have a highly directional angular distribution normal outwards from the shielding material. The angular distribution of the emergent neutron flux is much closer to the monodirectional beam outwardly normal to the shield, rather than being close to the isotropic flux, in most of our energy range. Hence, if we position our detector set-up so that it is directed normal to most of the emergent secondary neutrons from the shield, most of the neutrons hitting the detector go into the detector volume through the front face of the detector, and the neutrons going into the detector volume through the lateral sides are small. By putting some

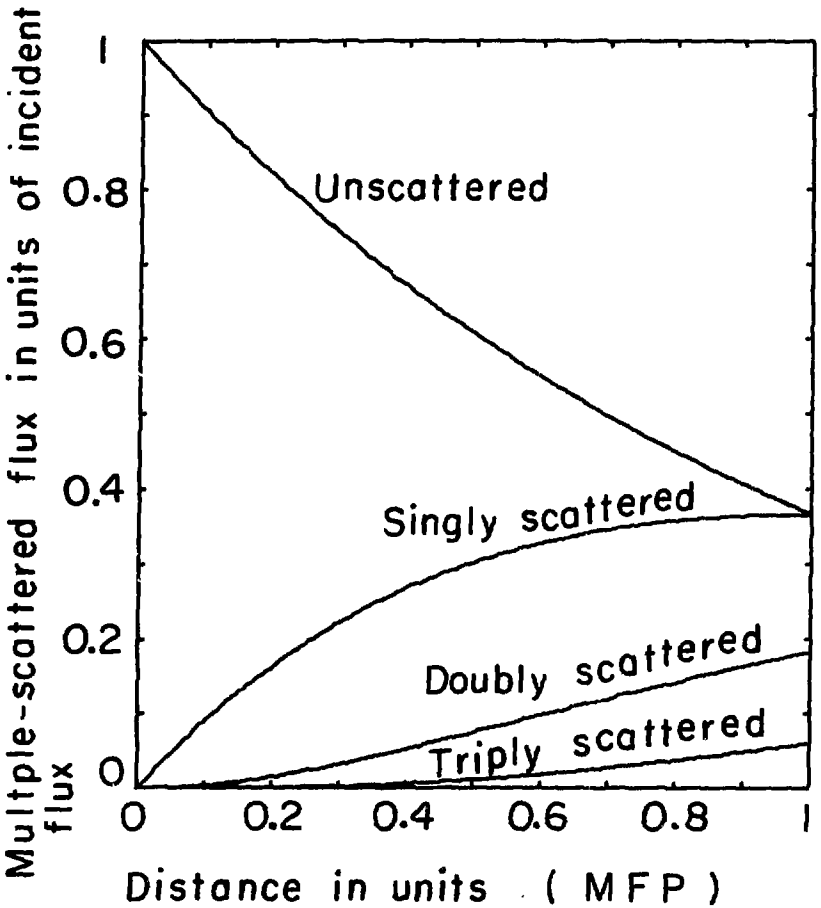

XBL7212-4949

Fig. 10. Variation of unscattered and multiple-scattered neutron flux.

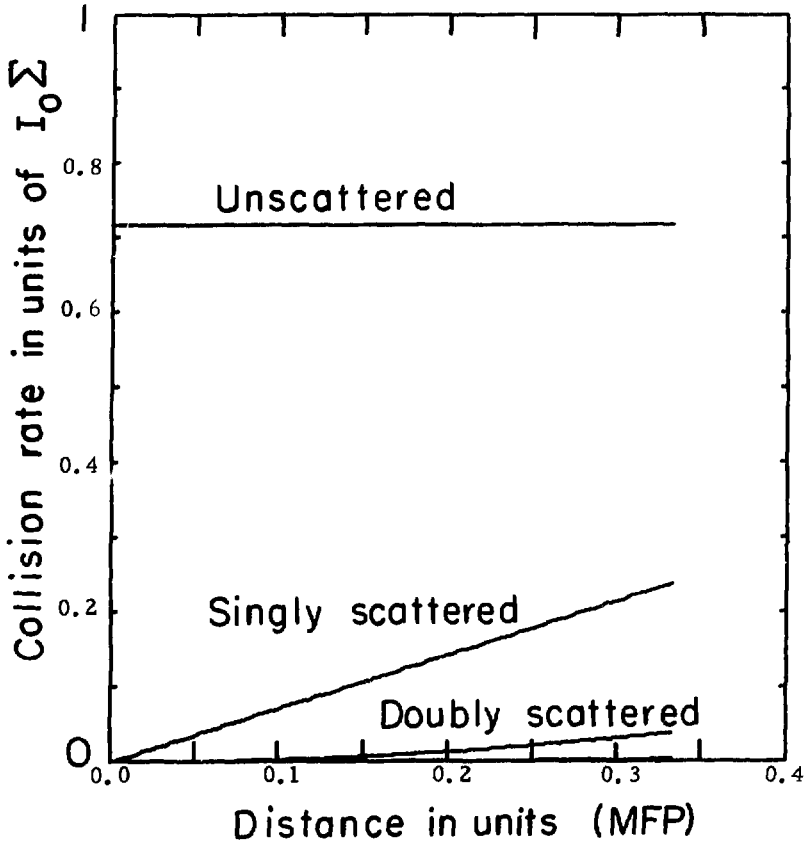

XBL 7212-4950

Fig. 11. Spatial collision rate of unscattered and multiple-scattered neutron flux when their scattered neutrons leave the detector without further collisions in a 1/3 λ size detector.

shielding material around the lateral sides of the detector, and also by putting anti-coincidence plastic scintillator around the lateral sides, the neutrons going into the detector volume through the sides can be further suppressed. Therefore, we shall assume here that the most of neutrons go into the detector through the front face, and the number of neutrons going into it through the lateral sides is negligibly small. Also we shall assume that the incoming flux through the front face is spatially uniform over the front face of the detector set-up and independent of position. In this case, if we represent the incoming neutron flux to the detector volume at the front face by $\Phi(E_n)$ and the front face area by A, then the total number of neutrons of energy E_n going into the detector volume is $A\,\Phi(E_n)$. These neutrons are the neutrons that provide the unscattered and multiple-collision fluxes inside the detector volume. On the other hand, we are interested in events that generate a single proton, leaving a single track in the detector volume. This is represented by the integrand of the energy, integral in equation (2-37), and there must be a definite ratio between the number of single-event protons of energy E_p leaving a single track and the total number of incoming neutrons of energy E_n. If we represent this ratio by $K(E_n,E_p)$, then

$$K(E_n,E_p) = \frac{\int_{V_m} d\underset{\sim}{r}\,\phi_0(\underset{\sim}{r},E_n)\,\Sigma_{np}(E_n) f_p(E_n,E_p)\,d_0(\underset{\sim}{r},E_p)}{A\,\Phi(E_n)}, \qquad (2\text{-}44)$$

or

$$\int_{V_m} dr\;\phi_0(r,E_n)\,\Sigma_{np}(E_n)\,f_p(E_n,E_p)\,d_0(r,E_p) = A\,\Phi(E_n)K(E_n,E_p). \qquad (2\text{-}45)$$

If we substitute $A\,\Phi(E_n)\,K(E_n,E_p)$, instead of the above space integral, into equation (2-37), we get

$$\phi_0(E_p) = \int_{E_p}^{\infty} dE_n\,A\,K(E_n,E_p)\,\Phi(E_n). \qquad (2\text{-}46)$$

This is the desired relation between the detected single-track event proton energy spectrum and the incident neutron spectrum. Since the above quantities are in fluxes, we can multiply by the time measurement interval Δt, and get the relationsip in absolute quantities, namely,

$$N(E_p) \equiv \phi_0(E_p)\,\Delta t = \int_{E_p}^{\infty} dE_n\,\Delta t\,A\,K(E_n, E_p)\,\Phi(E_n). \qquad (2\text{-}47)$$

$N(E_p)$ is the measured quantity and the $\Phi(E_n)$ is the desired quantity, and if we know $K(E_n, E_p)$, we can get $\Phi(E_n)$ by solving the above integral equation. As a matter of fact, the physical process generating the single-event proton flux at energy E_p from the incident neutron flux of energy E_n is relatively a simple one, and $K(E_n, E_p)$ can be evaluated rather accurately by simulating the above physical processes, using a random sampling method with the high speed computer. More specifically, the values $K(E_n, E_p)$ can be evaluated by taking a ratio of the number of generated single-event protons of energy E_p lying within the detector, to the number of injected neutrons of energy E_n, when a specified number of neutrons of energy E_n are injected through the front face of the detector. We then sample the protons from the first collision inside the detector whose track lies within the detector and its scattered neutron leaves the detector without any further collisions. Details of the sampling method are given in later chapter.

Once we have the kernel values at a set of energy points (E_n, E_p) and the measured single-event proton spectrum, the above equation (2-47) is solved for $\Phi(E_n)$ numerically. Due to the random errors inherent in the experimental values, a least squares method is adopted, which minimizes the square sum of the differences between the measured and calculated responses at a certain set of energy mesh points of E_p. Details of this numerical unfolding method are described in Chapter V.

The next chapter explains the experimental spectrometer set-up and the related electronics and hardware which detects the proton tracks, and measures the single-event proton energy spectrum.

III. SPECTROMETER SET-UP AND RELATED ELECTRONICS

1. General spectrometer set-up and triggering logic.

The spectrometer has been set up such that it includes the n-p converting material which provides the nuclear targets to the incoming particles, the spark chambers which detect the locations of the tracks of the emergent protons from collisions, scintillators and logic box which trigger the high voltage to the spark chambers only when protons are present and certain triggering conditions are satisfied, and finally, the part which processes into digital form the track data from the spark chambers and records those in the storage medium. Hence, the whole set-up can be roughly divided into four parts.

For the n-p converter, sheets of polyethylene are used. Of the available materials, polyethylene happens to have the highest concentration of hydrogen atoms in comparison with other organic materials. Thirteen polyethylene sheets of equal thickness, and an area of 50×50 cm^2, are placed symmetrically at the front, back and between the twelve equally-spaced spark chambers (see figure 13). Two thicknesses of polyethylene sheets, 1/4-inch and 1-inch thick, were selected, in order to cover the different range of particle energies. For triggering, twelve plastic scintillators 1/8-inch thick are placed right next to each chamber, in order to sense the passage of a charged particle and trigger the high voltage pulse instantly to each chamber. Light pulses are generated only in the scintillators which are traversed by a proton. The exterior of the whole set-up is covered with inhibiting anti-coincidence scintillators, in order to avoid triggering by charged particles from outside and also by protons escaping from inside, even though they are generated inside. Table (3-1) shows the chemical composition and density of polyethylene and plastic scintillator material used. Nuclear characteristics of these material, as a function of particle energy, have been shown in the previous chapter.

Table 3-1

	Polyethylene	Plastic Scintillator
Chem. comp.	CH_2	$CH_{1.1}$
ρ (gr/cc)	.91	1.02
N_H(atoms/cc)	7.83×10^{22}	5.16×10^{22}
N_C (atoms/cc)	3.91×10^{22}	4.69×10^{22}
Range-Energy formula	$E_p(MeV)=9.0R^{.55}(mm)$	$E_p(MeV)=9.17R^{.55}(mm)$

A comprehensive description of the physical processes inside the detector, and also of the data flow, is as follows: A neutron enters, makes a collision with the nuclei of the n-p converter medium, and produces either a recoil proton or a cascade proton, which travels a certain distance before it stops. The passage of this proton produces light pulses in the plastic scintillators it encounters and leaves ionizati ns in the spark chamber gas along its track. The light pulses from individual scintillators travel upward through lucite light pipes to the photomultiplier tubes, where the light pulses are converted into electrical signal and multiplied. These signals are fed into the triggering logic box, where they pass through the discriminators and the logic circuits. The logic circuits have been designed so that, if any three or more adjacent scintillators inside the spectrometer send out signals, and no signal is received from the outside inhibiting anti-scintillators, then the logic circuit issues one trigger pulse. The time delay through the logic box is approximately 90 nanoseconds. Then this trigger pulse goes to the high voltage pulsing system, where it is first amplified in the spark gap trigger amplifier and goes to the spark gap distribution box, which applies a pulse of high voltage to each of the 12 chambers. The high voltage pulse is produced by discharging the stored energy of the large capacitors in the spark gap distribution box. The optimum high voltage applied to our chambers was found to be 9 kV. As soon as the high

voltage is applied to the chambers across their two wire planes, streamer type sparks appear between the wires where the charged particle passed, by the avalanche of electrons remaining from the ionization along the proton track in the spark chamber gas. This opens a spark channel and causes its current to flow through the wires close to the spark. In addition, the two outside wires of each wire plane, which are called fiducials and spaced 50 cm apart, have been connected to the corresponding wires of the other plane through the resister-capacitor chains, and current pulses also flow through these channels when high voltage is applied. So, there are three current pulses flowing altogether, and these pulses go over the magnetostrictive wires which are placed just beneath and across the chamber wires separated only by 5 mil-thick mylar sheets. From here on, the track location retrieving process begins and it is done in a small gadget called a wand. The above current pulses induce the local deformations in the magnetostrictive wires through magnetic coupling in the parts close to the current pulses. These deformations travel along the wire with sonic speed, and sensed by the pick-up coil installed inside of the small preamplifier box on one end of each wire. The signals are converted into electrical signals, producing three distinct pulses spaced in time. This information is digitized, using 20 Mc pulses and scalers in the Magnetostrictive Readout Unit, and give the spark location with reference to the fiducial distances. Finally, all of this digitized information from the x and y axes of the twelve chambers is recorded on the magnetic tape as one event for future processing, with the CDC 6600 computer, to generate the single event proton energy spectrum. This whole process is repeated as a new proton is produced from a neutron collision inside the spectrometer. A schematic of the flow of the above process is shown in figure 12, and cable connections of the whole set up are shown in figure 13. (See also figures 14 and 15 for the actual set-up and electronics used.)

The specific scintillator material used was plastic scintillator pilot B from the New England Nuclear Co. This material gives the

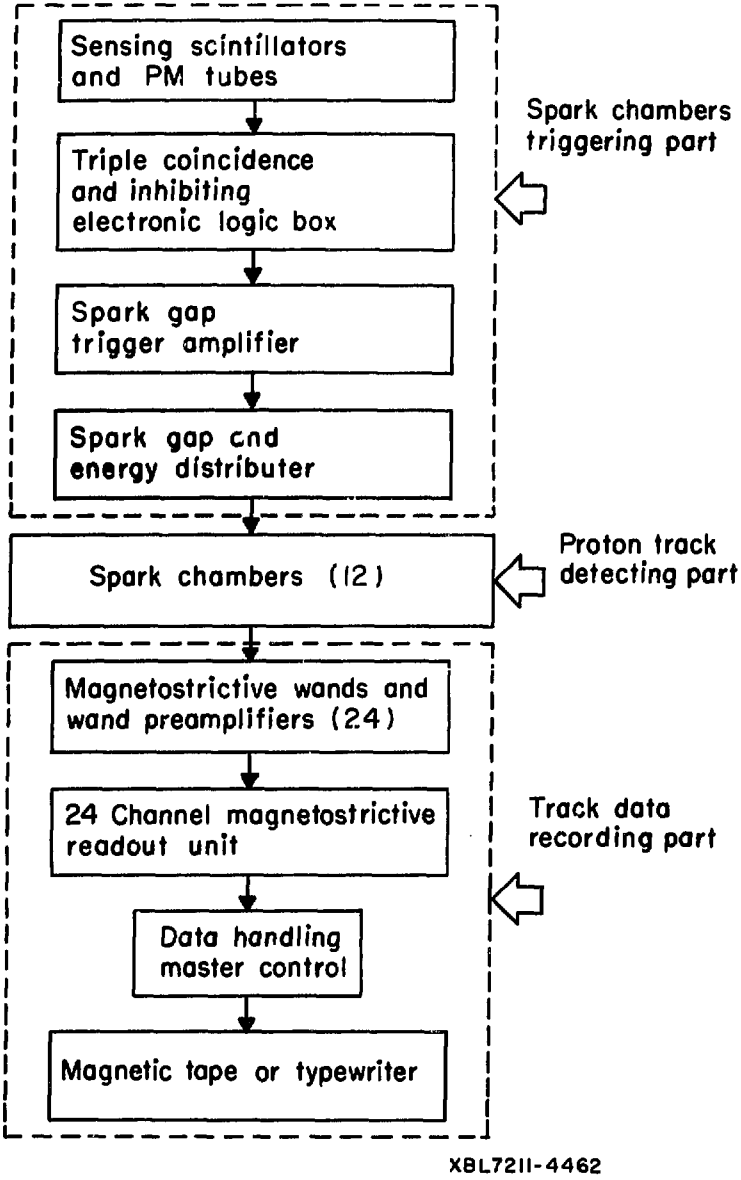

Fig. 12. Flow chart of event processing.

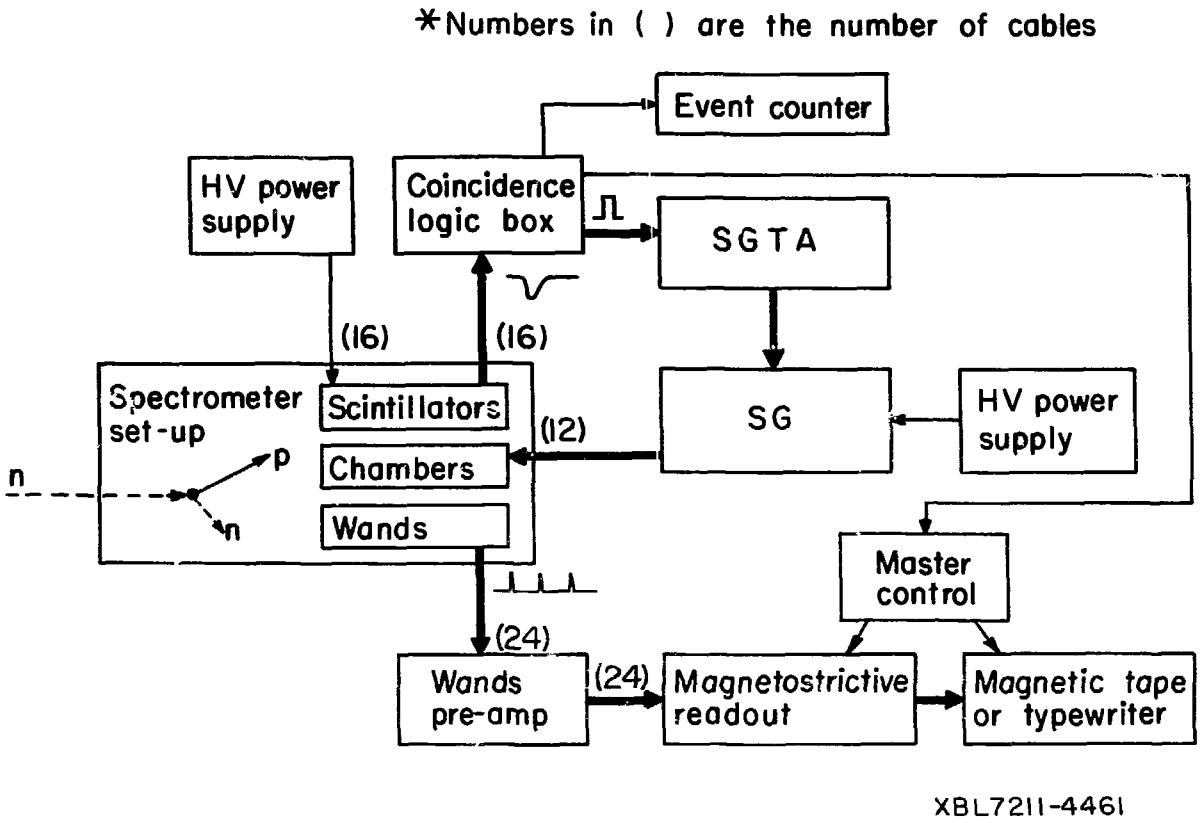

Fig. 13. Cable connections of a spectrometer setup and its electronics.

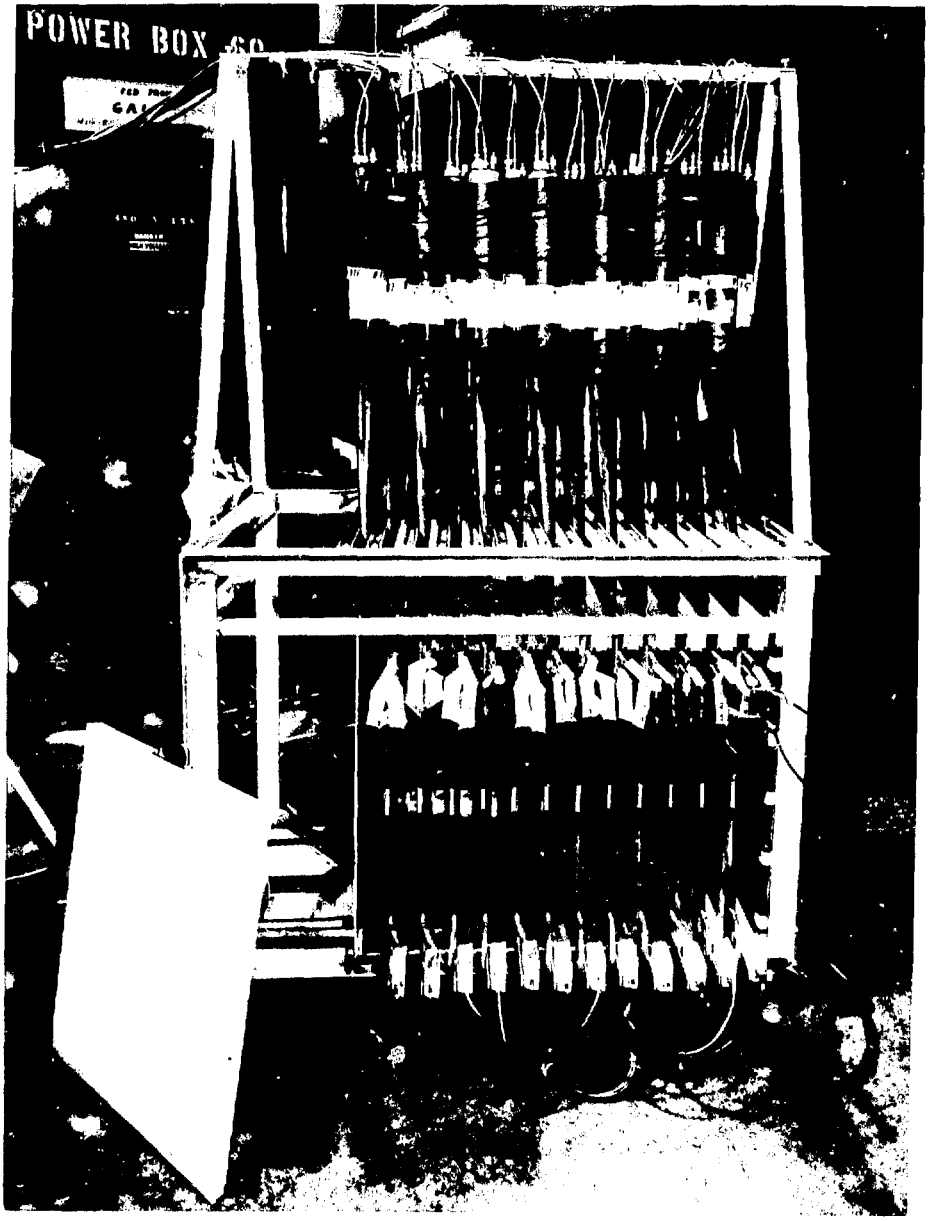

CBB 718-4040

Fig. 14. Spectrometer set-up.

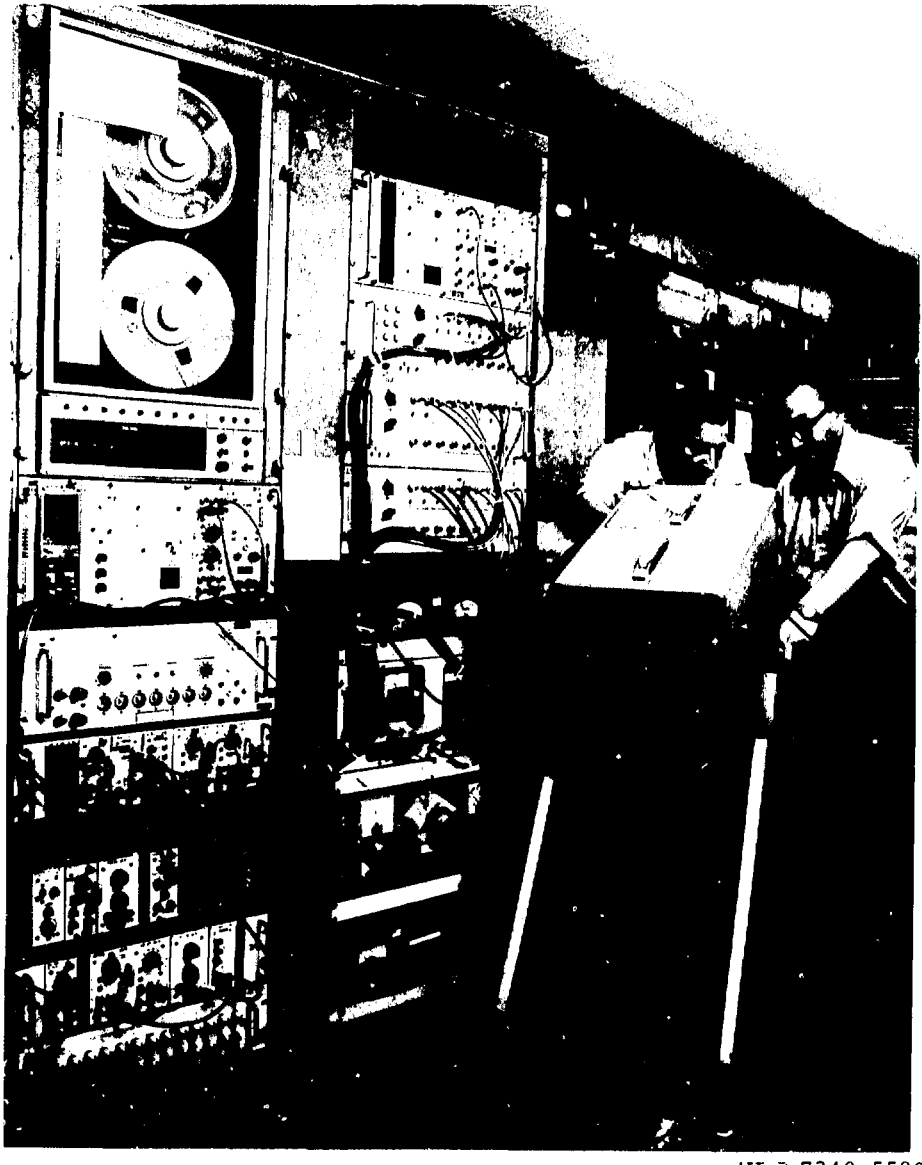

XLB 7210-5580

Fig. 15. Electronics set-up.

highest pulse height and shortest decay time (~2 nanoseconds) of any commercial plastic scintillator, with relatively good light transmission properties, which are good for our purposes. Each scintillator was connected to the triangular lucite light guide on one side of the triangular piece, and the light guide lucite was bonded to the photomultiplier tube RCA 8575 on the other side. Each photomultiplier tube was covered with μ-metal to shield it from the magnetic field, and the PM tube and mounting base were covered with an aluminum metal cylinder to provide shielding from the electrostatic field. The PM tubes have roughly a 31 nanosecond electron transit time at 3000 volts. The output pulse from each scintillator PM tube are fed into the discriminators of the triggering logic box through 50 ft, 50 ohm co-ax signal cables. The triggering logic box was made with fast logic circuit boards, using MECL II integrating circuit chips. (MECL stands for Motorrola Emitter-Coupled Logic.) These circuit boards usually have 5 ns rise time and 5 ns transit time. The triggering logic design, using fast logic circuit boards, is shown in figure 16. The logic was designed to require at least a triple coincidence among the scintillators assigned to each chamber, before it permits the output trigger pulse. The rectangular output pulses from the discriminators connected to the scintillators assigned to each of the chambers were adjusted to be approximately 20 ns wide. This pulse width was selected, based on the consideration of the minimum accidental coincidence rate, while allowing enough time to cover the light arrival time differences and jitters in the PM tubes in coincidence. However, the discriminators connected to the outside anti-coincidence scintillators were set to give ~65 ns-wide output pulses, in order to block the issuance of trigger pulses whenever the pulses come from the outside anti-scintillators. The passage of signals through the logic box takes roughly 30 nanoseconds, from the time of the input to the discriminator to the start of the trigger output pulse, which has 18 ns pulse duration. The elapsed time, from the moment of particle passage in the scintillators to the start of the PM tube output pulse, is usually less than 40 ns. Therefore, from the passage of a charged particle in the scintillator to the start of the trigger pulse,

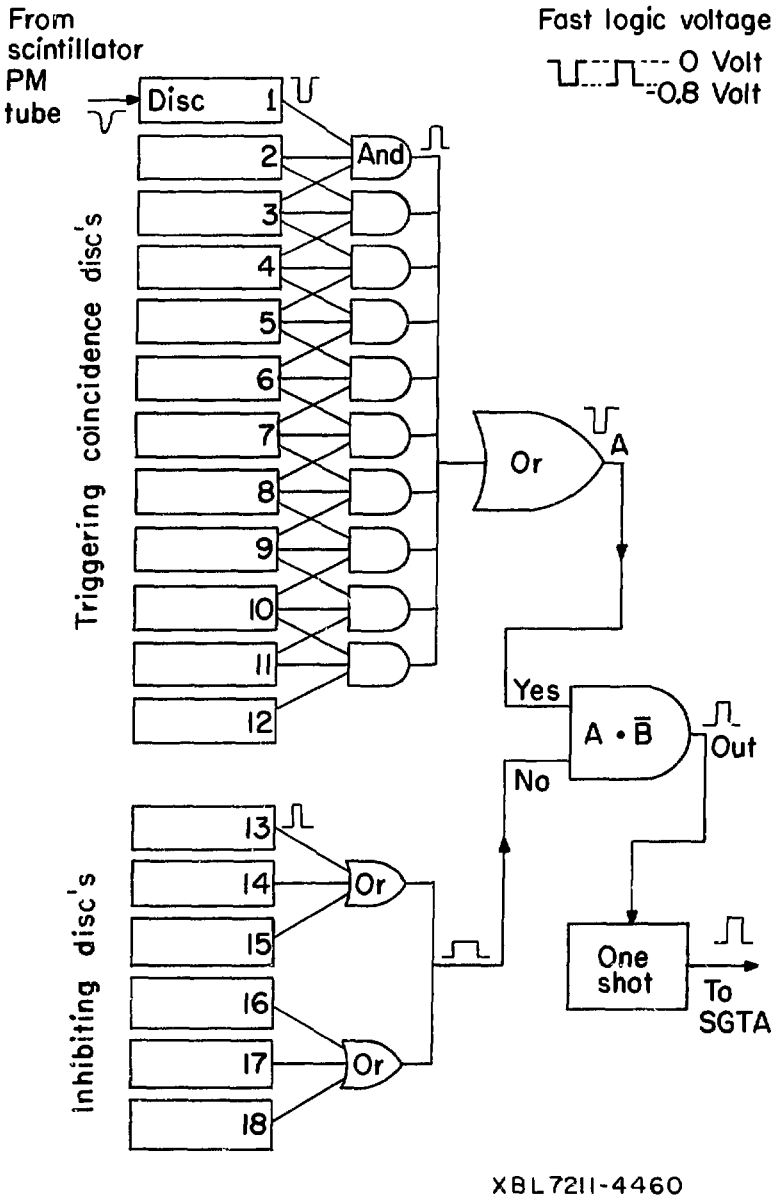

Fig. 16. Triggering logic diagram.

the total delay time, including that of the cables, is ~180 ns. By the way, the output pulse width from the PM tube of each scintillator was reduced to roughly 10 ns by hanging a ~4 ns-long clipping cable on the output end of the PM tube connector.

The trigger output pulse is amplified in the spark gap trigger amplifier, and then goes to the spark gap distributor box, which applies a ~200 ns-duration high voltage pulse of 9 kV between the two wire planes of each chamber. The wire connections that apply the high voltage pulses to the chambers are shown in figure 18 . The delay time in the spark gap trigger amplifier and the spark gap distribution box is roughly 65–75 ns for each channel. This means that the total delay time, from the passage of the charged particle to the moment of high voltage application to the chambers, is ~ 250 ns.

2. Spark chamber construction and operation.

Multi-wire spark chambers are made of planes of closely spaced parallel wires connected to a high voltage pulsing system through a common bus bar. Our spark chamber consists of two wire planes mounted perpendicular to each other with a gap of 1 cm. Each plane is connected to a common bus bar, called the high voltage and ground bus bars, respectively. (See figure 17). The chamber has a sensitive area of 50×50 cm^2, and the gap between the wire planes is spaced by the lucite frame supporting the wires that are glued onto it in tension by epoxy. The wires are 3 mil silver-plated beryllium copper, with 1 mm spacing. However, for the two outside wires of each plane, 5 mil copper wires were used. Each of these two wires on each plane is connected through a capacitor-resistor network to each corresponding wire on the other plane, so that every time a high voltage pulse is applied between the high voltage and ground bus bars, currents flow through these two channels. On each side of the frame, close to the electrode bus bar, a groove was cut, parallel to the electrode bus bar, and perpendicular to the wires of its plane, to slide in the thin aluminum rod carrying a magnetostrictive wire on it. This was covered with 5 mil mylar sheet to separate it from the electrode wires. Therefore, the magnetostrictive wire goes across each electrode wire, separated only by 5 mil thick

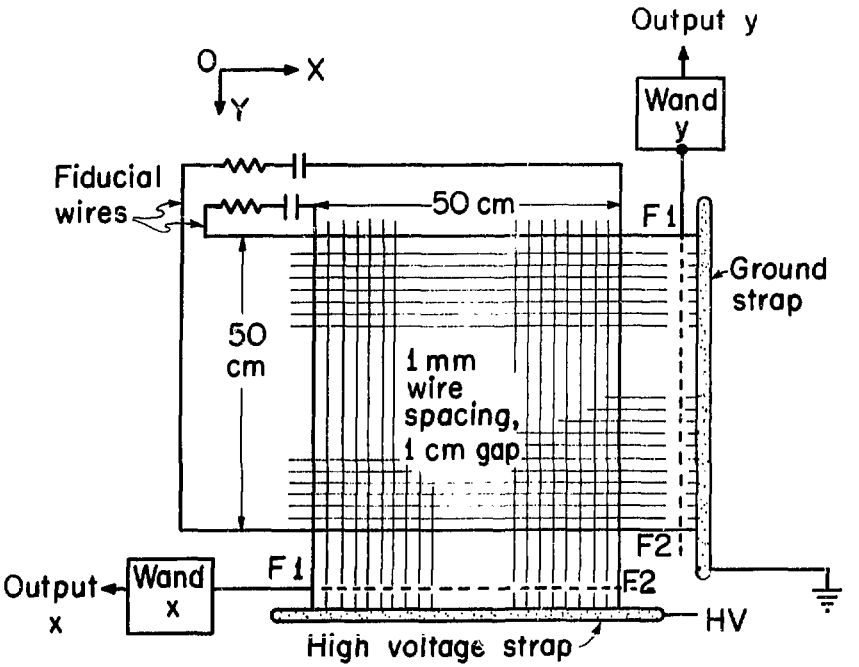

(a) Front view of a spark chamber

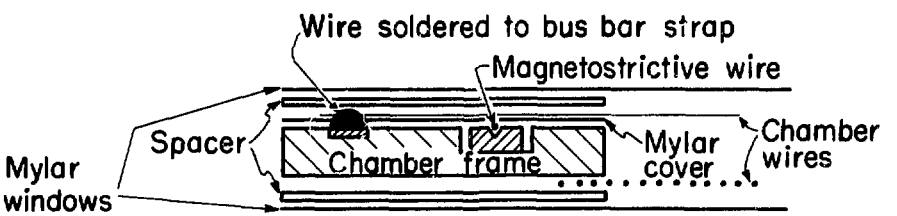

(b) Sectional view of chamber frame with wand

XBL7211-4459

Fig. 17. Spark chamber design.

mylar, and whenever current flows thru any of the electrode wires over it, there is good magnetic coupling to the magnetostrictive wire below it. This magnetic coupling is used to locate the spark position, and will be explained in detail in the next section. The signals from the two magnetostrictive wires determine the x-y coordinates. The chamber is sealed on each side by 3 mil mylar sheets, and is filled to 1 atm. with a gas mixture of 90% neon and 10% helium. The wire connections to each chamber are shown in figure 17.

Figure 18 shows electrical wire connections of each chamber with the external high voltage pulsing system, showing the principle of application of the high voltage pulse across the two electrode planes of the chamber. The principle of operation is as follows: Electric charge flows into the energy storage capacitor C_s through R_c from the high voltage power supply. As soon as the spark gap distribution box receives a trigger pulse from the SGTA, the spark gap breaks down, thus acting like a switch, and discharges the capacitor through the discharge resister R_d. thus producing a high voltage pulse across the chamber wires. The high voltage causes the avalanche of electrons from the ionized track, and a spark is formed between the wire planes.

The basic job of the pulsing system is to supply a high voltage pulse that is distributed uniformly throughout the chamber, of sufficient amplitude and duration to cause sparking in the presence of ionized tracks, but to avoid spontaneous break down. In addition, the pulsing system must provide sufficient energy to the spark, after it has formed, so that it can be reliably detected. In wire spark chambers with magnetostrictive readout, this means that current must flow in the spark for enough time to allow formation of a sufficiently large magnetostrictive pulse, whose amplitude is proportional to the time integral of current. The requirements for a pulsing system depend on the electrical characteristics of the spark chamber, the sparking characteristics of the gas and chamber, and the spark detection method. The numbers in figure 18 are the values which give the best performance in our chambers. Usually, each chamber has its own peculiarities, and for the capacitor-resistor networks in the fiducial chain, a trial-and-error method was used to select the values yielding the best magnetostrictive pulse in

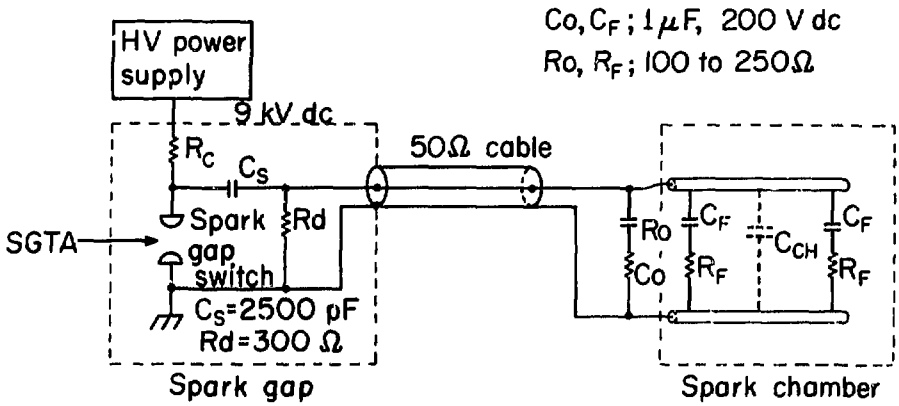

(a) Cable and wiring connections

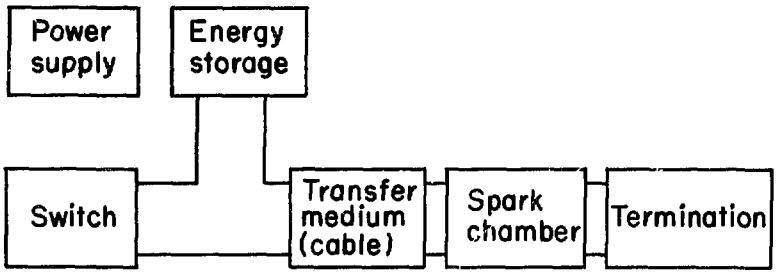

(b) Block diagram

XBL7211-4458

Fig. 18. Spark chamber pulsing system.

each chamber. The high voltage pulse usually has roughly 30 ns rise time and 150 to 200 ns duration.

In addition to the high voltage pulse, a small dc potential, called a clearing field, is always applied, in order to reduce the probability of the presence of random electrons at the time the pulse occurs, and to remove electrons and positive ions quickly after the spark. This field should not be so high as to remove electrons produced by the triggering particle before the high voltage pulse is applied to the electrode wires. Typically, the clearing field is arranged so that the transit time t_1 for an electron to cross the gap, under the action of the clearing field, is about twice the delay time t_2 between the passage of the particle and the initial rise of the high voltage pulse. Since the latter time is ~0.25 μsec, the clearing time should be of the order of 0.5 μsec. Any particles that pass thru the chamber during the interval t_1 immediately prior to the initiation of the high voltage pulse will, in general, produce sparks along their tracks, and t_1 can be called the sensitive time or resolving time of the system.

Another important parameter of a spark chamber system is the recovery time, that is, the time which must elapse after the operation of the chamber before it can satisfactorily be operated again. The high-voltage pulser usually require some time to recharge its storage capacitor, but this time can be made small. In fact, the recovery time is limited by the chamber itself because of the time required to remove all of the products of the previous spark, which might lead to reignition. The electrons are removed rapidly by the clearing field, but positive ions remain for a much longer time, and have a small, but finite, probability of producing electrons by secondary processes.

As to the basic mechanisms of spark formation, the process of the development and maintenance of an electrical discharge in a gas is extremely complicated, and has been discussed in detail by many others.[22] Let us limit ourselves to the mechanisms relevant to the development of a spark discharge in a gas, under the conditions which normally occur in spark chamber operation, as follows:[23] A discharge is normally initiated by one or more primary electrons which are accelerated by the applied field and then produce further electrons by ionizing collisions with atoms of the gas. Thus an electron avalanche builds up,

moving towards the anode with a velocity of the order of 10^7 cm/sec. The positive ions that are produced at the same time move towards the cathode with velocities of the order of 10^5 cm/sec, and therefore may be considered to be almost stationary, in comparison with the electrons. The initial growth of the electron avalanche is usually explained in terms of Townsend's first ionization coefficient. The process continues until the effects of the space charge of electrons and positive ions is sufficient to seriously modify the field and alter the mechanism of growth of the avalanche. Under those conditions, the field at the center of the avalanche head, where the density of both electrons and positive ions is high, becomes reduced and recombination becomes more probable, with the consequent emission of photons. Some of these photons produce photo-electrons in the gas surrounding the avalanche, thus producing fresh avalanches. The greatest multiplication in these auxiliary avalanches occurs along the axis of the main avalanche, where the space charge field augments the applied field. In this way, the process develops as a self-propagating streamer, which rapidly spreads in both directions towards the electrodes and forms the spark channel. The formative time of the above type is much shorter, because it does not involve positive ions. Since the primary avalanche defines the spark channel, the spark is much more closely aligned with the primary ionization, and multiple sparks are less likely to occur. It should also be noted that, since no secondary process at the electrodes is involved the characteristics of the spark are independent of the electrode materials and depends only on the properties of the gas. Usually a positional accuracy of 0.3 mm, for particle trajectories that are within 20 deg of the normal direction, is achieved in the chambers, using a digitizing frequency of 20 Mc.[12]

In the chamber, a gas mixiture (90% neon and 10% helium) is used at a pressure slightly higher than atmospheric pressure. Mixing helium gas with neon tends to reduce the working voltage of chambers below that where neon alone is used. Since this gas mixture is rather expensive, it is cleaned and recirculated through the chambers again, using a gas purifier-recirculator device.[24] The gases are also mixed with alcohol by letting 10% of the flow volume pass through an alcohol bath. Adding alcohol reduces the threshold of operation by about 4 kV dc.[25] This phenomenon, attributed to Penning, is very helpful, as

it allows the chamber to be pulsed at a substantially lower voltage. Another useful property of the alcohol is its ability to suppress spurious sparking.

The working voltage of our chambers has been obtained with the above gas mixture by testing the performance of each chamber with the magnetostrictive readout. The setup for the chamber test is shown in figure 19 with the wire connections. A collimated β-particle source was used, and two scintillator counters, one very small and the other large, provided a double coincidence trigger. Two quantities were counted for each x-and y axis coordinate: the number of event triggers and the number of magnetostrictive pulses falling within a very narrow time window close to the test spot. Each 200 trigger events was observed, and Table 3-2 shows the average number of sparks falling within the small time window for each chamber. The source was moved around the chamber face, and no variation of efficiency was observed. The charging capacitors and resistors shown in figure 18 were used in the test. The minimum voltage that gives uniform efficiency for all twelve chambers is 9 kilovolt, and this voltage has been used in all cases.

3. Magnetostrictive readout and data recording.

As mentioned before, the spark positions are ascertained by the magnetostrictive readout method.[13,14] Figure 17a shows the positions of the magnetostrictive delay lines and the fiducial connections in our chambers. Figure 17b shows the more detailed sectional view indicating the relative position of the magnetostrictive line to the chamber plane wires. When a spark occurs–due to the passage of a charged particle–between the wires of the high voltage (upper) plane and the ground (lower) plane, the spark current flows along the wires close to the spark and through the spark channel. The magentic field surrounding the current-carrying wire produces a local deformation in tne magnetostrictive lines, one on the high voltage plane side and the other on the ground plane side. These deformations travel along the line with the velocity of sound which is ~5000 m/sec. This is a velocity of 5 mm/μsec, or a dealy time 0.2 μsec/mm. (Note that wire density of

Table 3-2

Detected spark pulses within the window for every 200 events recorded.

H.V.	X-axis			Y-axis		
Ch. No.	8.0 KV	8.5 KV	9.0 KV	8.0 KV	8.5 KV	9.0 KV
1	198	194	199	197	194	199
2	194	199	200	181	199	199
3	190	198	199	178	196	199
4	181	197	200	147	197	198
5	196	200	200	191	197	200
6	191	200	200	10	188	196
7	172	196	197	144	196	196
8	191	198	200	112	194	198
9	193	198	199	177	196	199
10	190	199	199	65	191	196
11	195	198	199	0	130	195
12	197	200	200	175	195	195

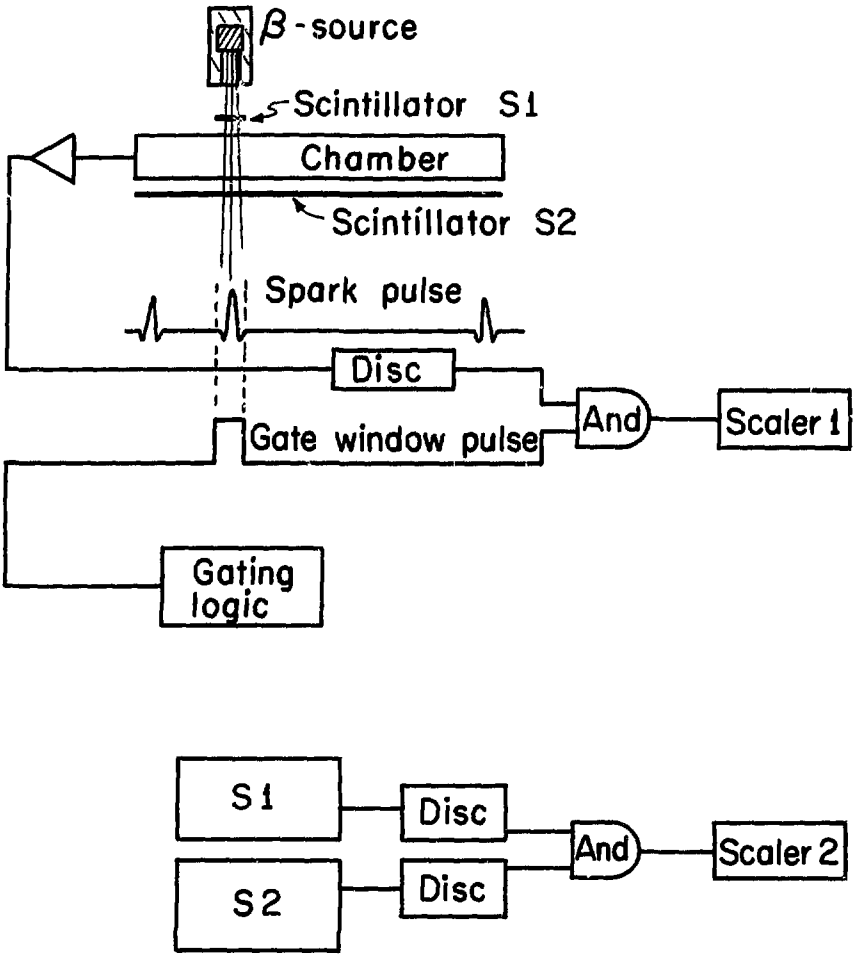

XBL7211-4457

Fig. 19. Sparking efficiency test logic of spark chambers.

the ordinary spark chamber is one per mm.) The deformation produces a voltage pulse in a pickup coil at the end of the dealy line, and then is amplified and clipped by an amplifier mounted on the same support that holds the magnetostrictive line. This assembly is called a wand. The signals then go to the next magnetostrictive readout unit, where they are differentiated; the zero-crossing point is used to generate a timing pulse for digitization. Figure 20 shows the process up to this stage. The logic for digitizing the wand data is shown in Fig. 21. Usually there are three magnetostrictive pulses, one from the spark channel and two from the fiducials on each end. The first fiducial signal starts two scalers which count the number of pulses produced by a 20 Mc pulse generator. The second signal (usually the spark signal) stops the first scaler, and the third signal stops the second scaler (usually the second fiducial). These two scaler numbers are then sent either to magnetic tape or to the selectric typewriter. Note that the 20 Mc pulser produces about four counts per mm of signal propagation, according to the above speed, which represents a position accuracy of 0.25 mm. This is compatible with the spark position accuracy of the spark chambers.

The fiducial signals serve two purposes: First, their spatial location makes it possible to determine the spark location with respect to a coordinate system external to the chamber. Second, the first and second fiducial signals produce a normalizing number that is used to correct for variations in the propagation velocity of the signals, due to changes in temperature, composition, density, etc.

The distance between the fiducial wires in each plane in our spark chambers is 500 mm and, assuming the approximate signal propagation mentioned above (corresponding to 0.2 μs/mm), we expect to have ~2000 counts in the 20 Mc scaler between the two fiducial pulses. In fact, we get fiducial numbers ranging grom 1870 to 1890 in actual cases, corresponding to 3516 to 3537 in octal numbers. Note that we have 24 wands, 2 wands from each of 12 chambers, and therefore 48 scaler numbers. Note also that in an actual measurement situation the magnetization in the magnetostrictive line in the wand is gradually destroyed by the magnetic field present around the accelerator, unless one magnetizes the wands with reasonable frequency. In our particular magneto-

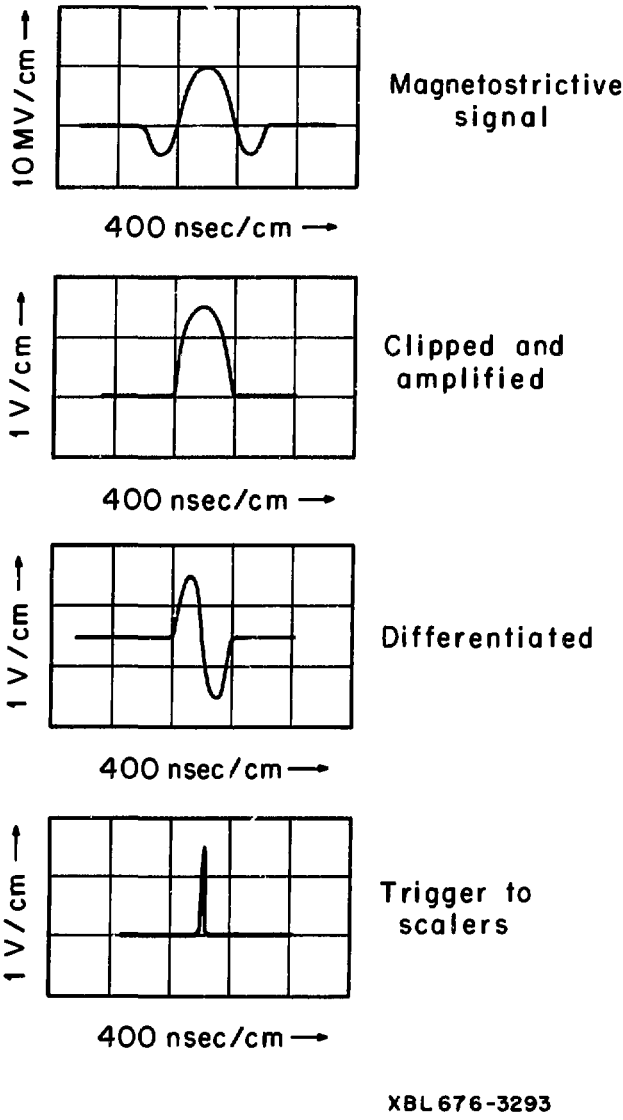

Fig. 20. Magnetostrictive pulse treatment with zero crossing.

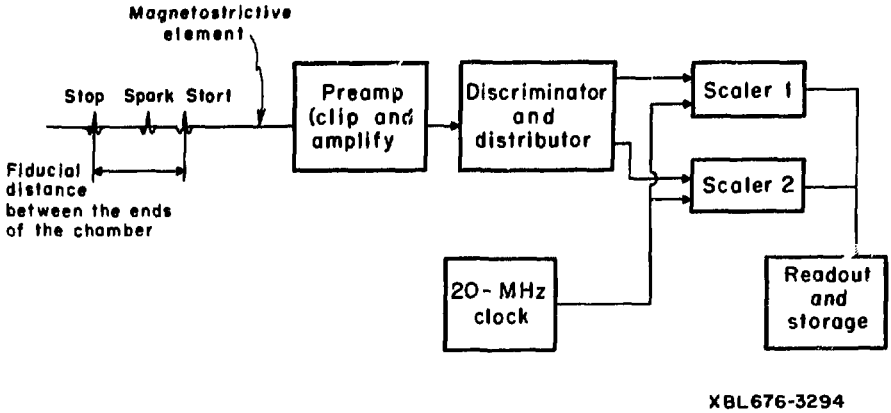

Fig. 21. Digitization logic.

strictive readout unit, all of the scalers were wired so that if they count more than the expected fiducial count number, they overflow and stop after recounting a very small number, usually 12 or 13 in octal. This is helpful in the later computer analysis for checking the presence of a spark in the chamber.

One more comment should be made in connection with the cycling time or dead time of our spectrometer. Usually the spark chamber magnetostrictive readout system is connected to the small computer, which processes the events and stores only good events in its buffer temporarily,[26] and later transfer the stored events to the magnetic tape periodically. This makes the data handling very fast, and the cycling time or dead time of the whole unit is decided by the recharging time of the high voltage pulsing system to the chamber. However, at the present stage, we couldn't connect a computer to our data handling unit for economic reasons, and the magnetostrictive readout was directly connected to the magnetic tape. The recording speed of the magnetic tape unit is extremely slow, and therefore this part determines the cycling time of the whole unit. The cycling speed of only one event per second (or slightly less) has been achieved with just the magnetic tape. Eventually a small computer should be connected to the spectrometer setup to increase the data handling speed and better cope with the event occurrence rate in the stray neutron radiation field.

4. Test of the complete spectrometer setup.

The complete spectrometer setup and electronics has been subjected to test as an integral unit. This was done in two stages. First, a test was made with a strong energy β source (^{106}Ru), mainly to test the simultaneous sparking of 12 chambers. Two scintillators, one small (2×2 cm^2) and the other large (50×50 cm^2), were placed on both sides of the 12 spark chamber setup, without converters. Electrons from the β source passed through the small scintillator, a stack of 12 chambers, and hit the large scintillator. In this case, more than 94% of the observed events produced simultaneous healthy sparking along their path. Even though this does not give the positional accuracy, because electrons make a zig-zag path along their track, even in the gas, this is

a meaningful result in the following sense: Suppose that each chamber has 99% sparking efficiency, then the probability that all of the 12 chambers will spark at the same time along the track is roughly 88%, since the simultaneous sparking probability is the product of the 12 chamber sparking efficiencies. Therefore, 94% simultaneous sparking efficiency means that the sparking efficiency of each individual chamber is better than 99%, which is a very good result. In the test, much bending of the electron path was observed.

Next the spectrometer setup was tested with the proton beam of the 184" cyclotron at the Lawrence Berkeley Laboratory. Figure 22 shows the spectrometer setup and triggering scintillators. The chambers were triggered only when the proton beam passed through the tiny hole of the anticoincidence scintillator, after passing through the small telescoping coincidence scintillator, and hit the large coincidence scintillator. In this experiment, all of the chamber triggering scintillators were inserted, and timing between their scintillator pulses was aligned within a few nanoseconds. The scintillator pulses, using the proton beam, were stronger than those with the β source. Data were observed in a batch of 500 events at various locations and directions. All of the runs gave similar results, showing that the spatial efficiency of the spectrometer setup is uniform throughout its front face. Among 500 events recorded in each run, ~ 5 events gave double tracks or double scattering-like events, ~25 events were discarded in the computer processing due to various random machine irregularities, ~50 events could not pass through the least square fit stage in the straight line checks, and ~400 events made good straight line tracks along the chambers when 2 or 3 mm average positional deviation from the fitted line were required in the least square fit line check. Positional accuracy of 2 or 3 mm is a very stringent requirement if one considers the possible small misalignments between the 12 chambers in actual mounting of the chambers. However, some variations of spark position accuracy were observed with the change of injection angle, even though they were small. These are shown in Table 3-3 and 3-4. In the normal injection case the average spark position accuracy was ~.4 mm and for the ~25° angular

injection case it increased to ~.5 mm. See figures 22-a and 22-b for typical cases. Figure 22-c shows the variation of the number of successful events in the least square line fit check when the average deviation requirement of the track data were changed. Here you can see the broadening of positional accuracy more clearly with the angular injection. The results were as expected.

The entire test above was made during two operating shifts of cyclotron time (16 hours). The overall results of the above test confirms that the whole system, as an integral unit, is very reliable and can give very accurate measurements of the proton track events.

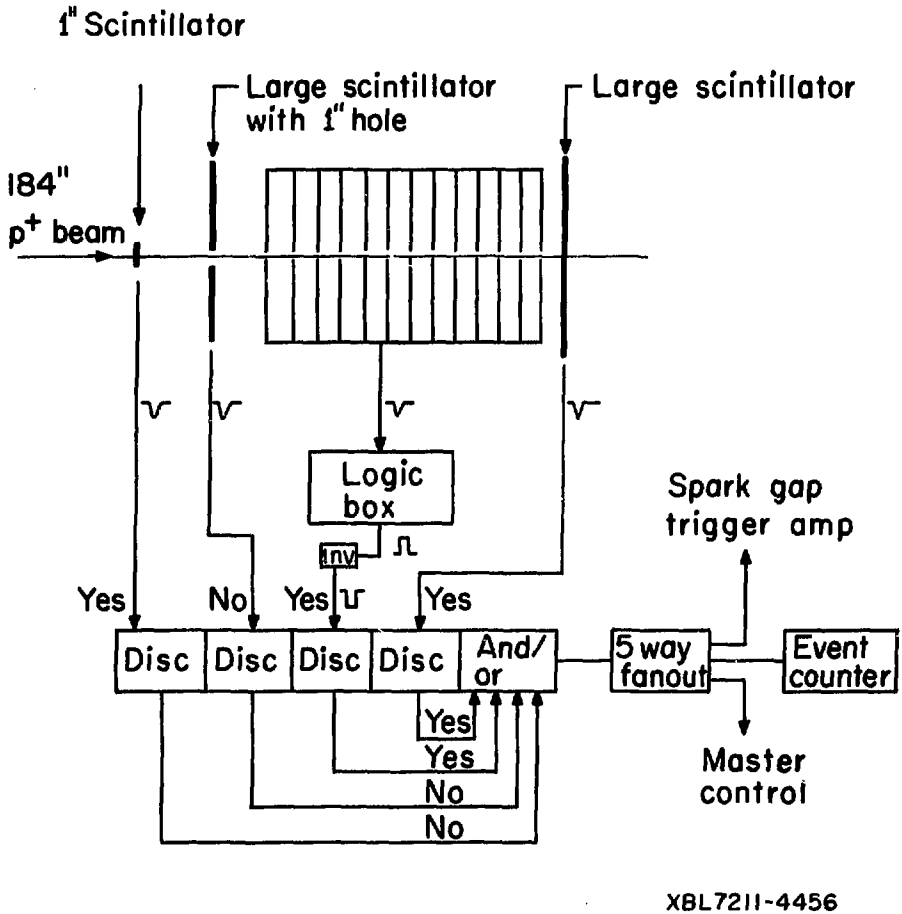

Fig. 22. 184-Inch Cyclotron proton beam test diagram of the spectrometer setup.

Table (3-3) Normal injection case.

STATISTISTICS OF DEVIATIONS FROM THE FITTED LINES

TOTAL EVENTS OBSERVED -------- 380
AVERAGE DEVIATION AMONG THEM-- .40

DETAILS OF DEVIATIONS IN EACH WAND IN UNITS OF .25MM

CH NO	AXIS	OFF	-5	-4	-3	-2	-1	FIT	1	2	3	4	5	OFF	TOTAL
1	X-AXIS	0	0	0	1	3	9		39	96	116	66	38	12	380
1	Y-AXIS	1	0	0	2	9	37		76	114	97	37	7	0	380
2	X-AXIS	1	5	24	83	98	91		60	10	5	2	1	0	380
2	Y-AXIS	0	0	0	4	33	135		145	55	6	1	0	1	380
3	X-AXIS	1	4	25	69	116	92		52	18	3	0	0	0	380
3	Y-AXIS	2	35	132	148	53	0		2	0	0	0	0	0	380
4	X-AXIS	0	0	3	10	46	100		115	76	20	8	1	1	380
4	Y-AXIS	6	0	0	2	23	97		174	77	7	0	0	0	380
5	X-AXIS	0	0	2	9	24	53		103	92	64	25	6	0	380
5	Y-AXIS	0	0	3	31	100	128		82	29	6	1	0	0	380
6	X-AXIS	2	22	67	90	83	65		31	16	3	1	0	0	380
6	Y-AXIS	0	0	1	4	46	124		144	41	18	2	0	0	380
7	X-AXIS	2	7	30	86	116	86		35	15	1	1	0	1	380
7	Y-AXIS	1	0	8	27	101	129		87	22	4	1	0	0	380
8	X-AXIS	0	0	1	12	40	99		117	72	31	7	1	0	380
8	Y-AXIS	0	0	0	1	2	32		102	153	70	17	3	0	380
9	X-AXIS	0	0	5	24	78	124		93	43	9	1	0	3	380
9	Y-AXIS	0	0	0	0	2	15		96	171	83	12	1	0	380
10	X-AXIS	0	0	0	0	0	15		56	106	105	76	15	6	379
10	Y-AXIS	0	0	0	0	0	0		33	142	165	37	2	0	379
11	X-AXIS	2	0	20	84	111	98		37	9	3	0	0	0	379
11	Y-AXIS	0	16	77	154	107	24		1	0	0	0	0	0	379
12	X-AXIS	0	1	2	5	18	62		112	90	61	24	2	1	378
12	Y-AXIS	0	0	0	28	100	116		87	35	3	1	0	0	378

Table (3-4). ~25° angular injection case.

STATISTISTICS OF DEVIATIONS FROM THE FITTED LINES

TOTAL EVENTS OBSERVED -------- 312
AVERAGE DEVIATION AMONG THEM-- .54

DETAILS OF DEVIATIONS IN EACH WAND IN UNITS OF .25MM

CH NO	AXIS	OFF	-5	-4	-3	-2	-1	FIT	1	2	3	4	5	OFF	TOTAL
1	X-AXIS	0	0	0	6	8	15		24	69	57	71	37	24	311
1	Y-AXIS	1	0	0	3	11	45		72	65	68	34	11	1	311
2	X-AXIS	7	10	25	59	83	58		45	17	5	2	0	0	311
2	Y-AXIS	1	0	1	9	63	120		93	19	4	0	0	1	311
3	X-AXIS	7	11	31	45	83	61		37	21	11	2	1	1	311
3	Y-AXIS	5	28	98	133	46	7		2	0	0	0	0	0	311
4	X-AXIS	3	2	7	14	48	64		64	71	36	7	3	0	311
4	Y-AXIS	0	0	1	0	18	99		121	57	15	0	0	0	311
5	X-AXIS	1	5	9	22	46	58		64	52	36	14	3	1	311
5	Y-AXIS	0	0	7	15	57	115		77	36	4	0	0	0	311
6	X-AXIS	16	33	34	66	78	34		32	20	2	0	2	0	311
6	Y-AXIS	0	0	0	17	34	69		189	58	23	1	1	0	312
7	X-AXIS	9	7	12	47	52	67		65	35	18	4	4	0	312
7	Y-AXIS	0	1	7	31	64	94		74	33	7	1	0	0	312
8	X-AXIS	1	1	9	9	13	41		62	72	65	31	6	2	312
8	Y-AXIS	0	0	0	0	3	21		73	113	68	29	4	1	312
9	X-AXIS	1	0	12	14	46	69		67	48	39	12	1	1	311
9	Y-AXIS	0	0	0	0	0	11		49	118	106	30	5	0	311
10	X-AXIS	2	0	1	7	9	23		31	62	77	69	21	9	311
10	Y-AXIS	0	0	0	0	0	1		14	84	132	72	7	1	311
11	X-AXIS	7	16	42	61	74	66		31	10	3	0	0	1	311
11	Y-AXIS	0	21	91	107	71	19		2	0	0	0	0	0	311
12	X-AXIS	1	4	8	15	36	56		73	64	28	14	9	1	311
12	Y-AXIS	0	0	20	78	72	84		35	10	3	0	1	0	311

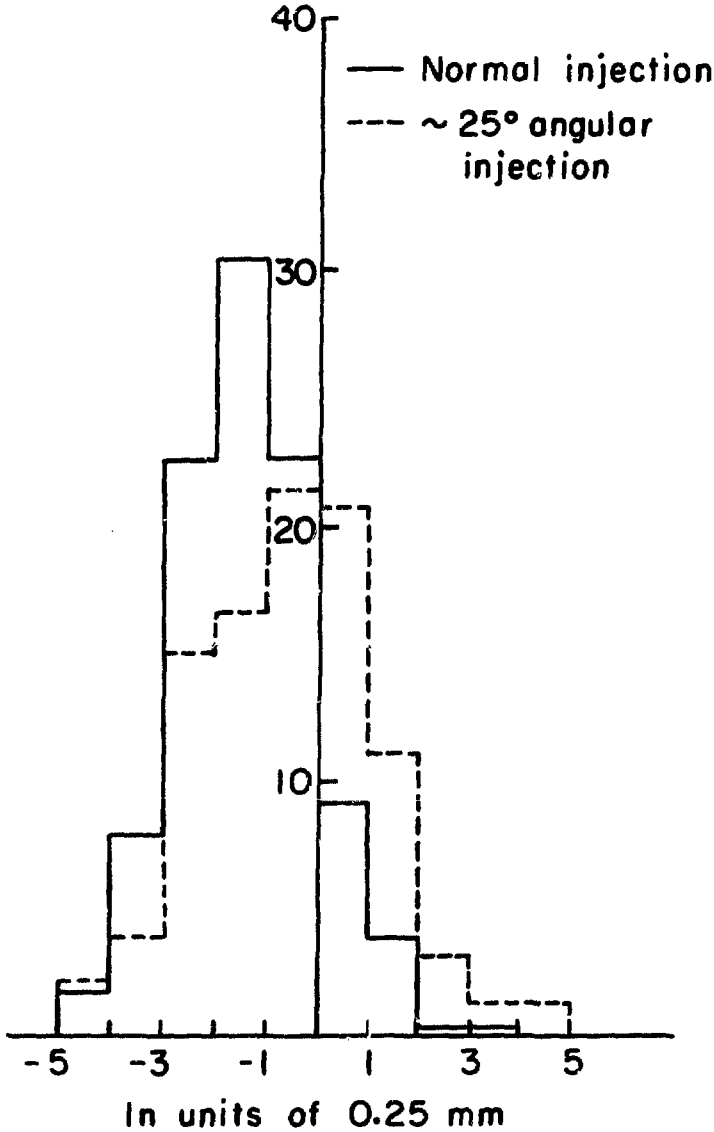

XBL7212-4952

Fig. 22-a. Deviations of measured coordinates from the fitted line for chamber 7, x-axis, normalized to 100 events.

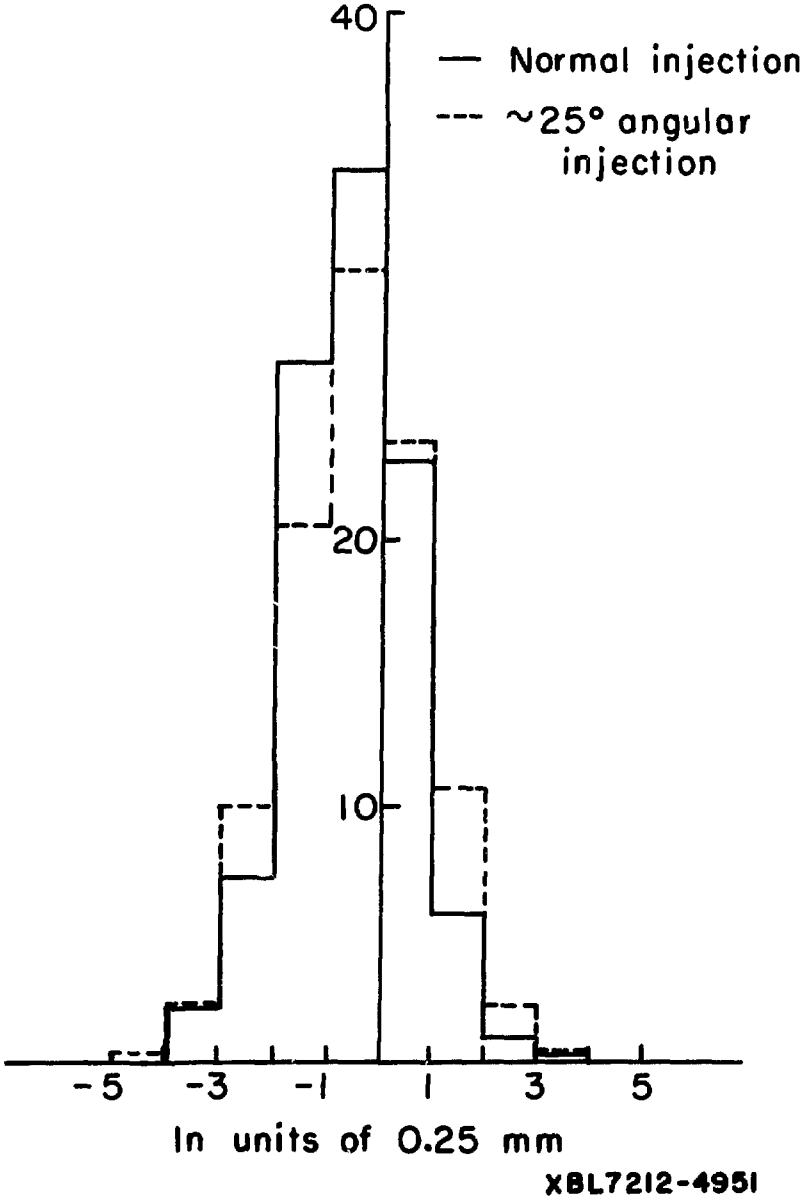

Fig. 22-b. Deviations of measured coordinates from the fitted line for chamber 7, y-axis normalized to 100 events.

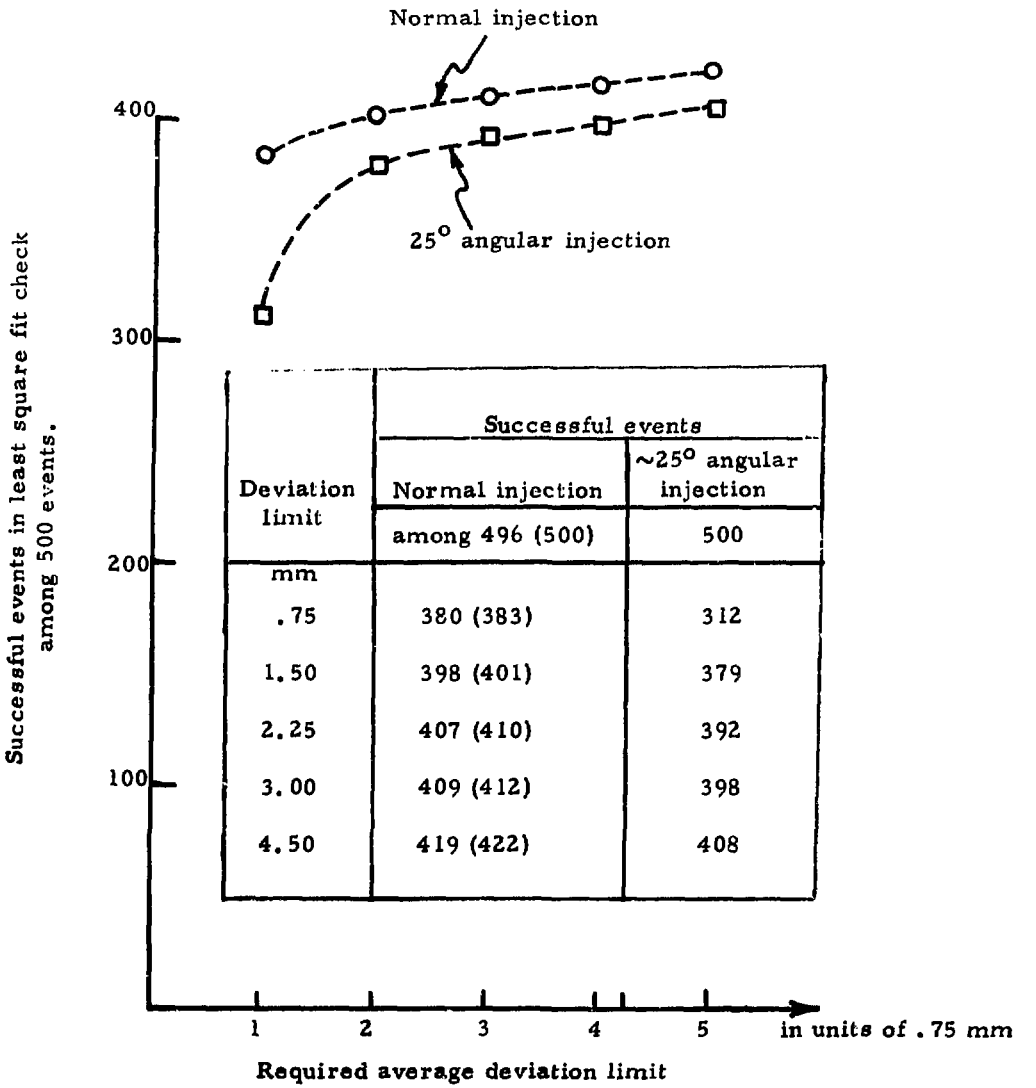

Deviation limit	Successful events	
	Normal injection	~25° angular injection
	among 496 (500)	500
mm		
.75	380 (383)	312
1.50	398 (401)	379
2.25	407 (410)	392
3.00	409 (412)	398
4.50	419 (422)	408

XBL7212-4948

Fig. 22-c. Variation of successful events in least square fit check with the given average deviation limit.

IV. DATA PROCESSING

This chapter deals with the processing of the data in the magnetic tape collected from the spectrometer setup. This was done with the CDC 6600 fast electronic computer, and a fairly large program was developed for the task. This chapter essentially explains this program, whose main purpose was to generate the single-event proton energy spectrum out of the raw track data after the data were processed. However, because the sparking activity in the chambers are basically probabilistic phenomena, and it is always possible for some part of the whole instrument setup to go wrong and spoil the acquisition of correct information, inspection of individual chamber performance and checking of the proper functioning of the whole setup as an integral unit was an equally important job of the program. This was done by accumulating statistics of the performance of each chamber and also detecting irregularities among the twelve chambers as an integral unit, as part of the processing. Figure 23 shows the flow chart of the blocks in the program.

1. Method of recording and unpacking data.

In each event, the data are transmitted in the following order from the spectrometer setup to the recording device: horizontal wand (x-axis) of chamber 1, vertical wand (y-axis) of chamber 1, then horizontal and vertical wands of chambers 2 through 12. Chambers were numbered from the front face of the spectrometer setup. Each wand gives two items of digital information, e.g., spark position and fiducial distance, in the single spark case. Each information set is digitized in a 12-bit or 4-digit octal number, which will be called a word from now on. Since there are 24 wands and each wand produced two digitized octal words, there are 48 octal words. To this set, two other 4-digit octal words, 7777_8 7777_8 are added as check bits at the beginning of each set to identify the beginning of each event, making a total of 50 4-digit octal words, or 600 bits, per event. (Note that this corresponds to ten CDC-66 words, since a CDC 6600 word is a 60-bit

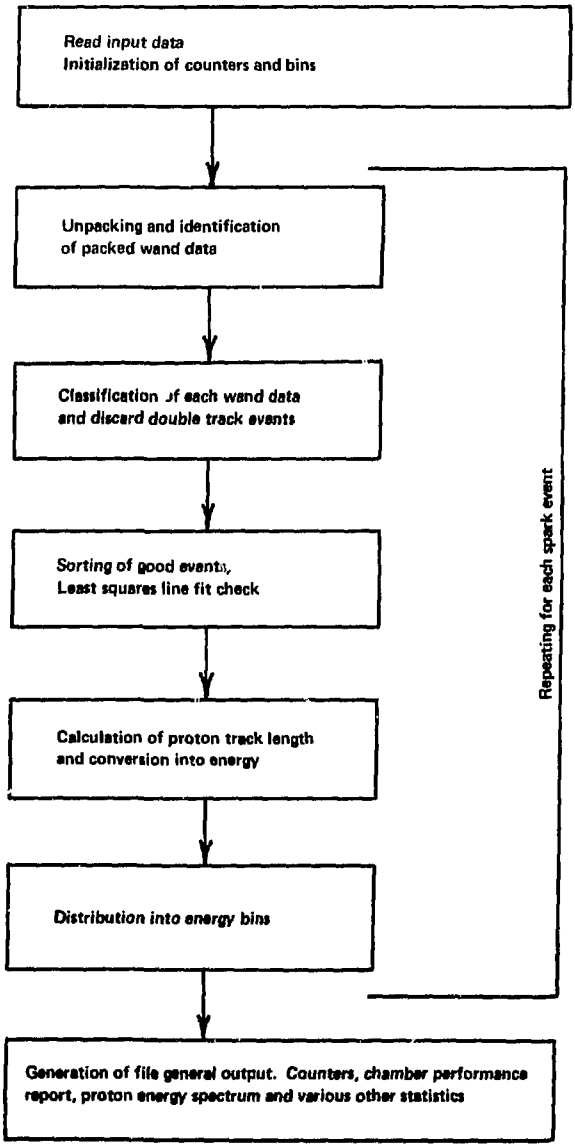

Figure 23, Flow chart of blocks in track data processing

XBL7212-4947

a) packed form of data

7777777735360013352600123533001135243561177035360016351716163535
0440352114523536105335211266131635240012114635362107352607623537
2511352505460556352600110270030335240012353400113524001135400012
35230012

b) unpacking of data

7777 7777 3536 0013 3526 0012 3533 0011 3524 3561 1770 3536 0016 3517
1616 3535 0440 3521 1452 3536 1053 3521 1266 1316 3524 0012 1146 3536
2107 3526 0762 3537 2511 3525 0546 0556 3526 0011 0270 0303 3524 0012
3534 0011 3524 0011 3540 0012 3523 0012

c) identification of data

Chamber Number	X-axis D1	X-axis D2	Y-axis D1	Y-axis D2
1	3536	0013	3526	0012
2	3533	0011	3524	3561
3	1770	3536	0016	3517
4	1616	3535	0440	3521
5	1452	3536	1053	3521
6	1266	1316	3524	0012
7	1146	3536	2107	3526
8	0762	3537	2511	3525
9	0546	0556	3526	0011
10	0270	0303	3524	0012
11	3534	0011	3524	0011
12	3540	0012	3523	0012

Figure 24. Unpacking and identification of data.

word.) These numbers were recorded on the magnetic tape listed as a series of numbers without interruption, namely, in packed form (see figure 24a). A specified number of events were listed in packed form as a group partitioned by a mark called a record mark on the tape. So the first operation then in the processing was to unpack the above series of numbers and identify the numbers with the axis of each chamber in the spectrometer setup. This is done at the start of the program, as shown in figures 24b and c.

2. Classification of digitized wand data.

After the unpacking and identification of the wands, each wand output goes through the stage that classifies the spark type and checks the existence of any possible irregularities in connection with the fiducial distance. The possible regular spark types in each wand in our case are: no spark, single spark, and double spark. However, in order to cope with various machine irregularities, every possible case anticipated out of the two-scaler output from each wand was included. Of each two digitized numbers of the wand, the first number will be called D1 and the second number D2. There are largely three possible cases between these two numbers: D1 and D2 can be equal; D1 can be larger than D2; or D1 can be smaller than D2. The second case is possible because the second scaler overflow and recounts from zero, if it counts up to the number slightly larger than the expected fiducial number. This recounting after overflow was designed to stop after counting a small number, usually 12_8 or 13_8. Note that the expected fiducial number ranges roughly to 3530_8. The first possibility is divided into two cases, i.e., either D1 and D2 are both zero or finite and equal. The both-zero case means that no pulses came from the wand, and this usually means the high voltage wasn't pulsed on. The event containing this kind of case do not need further processing, and is discarded after completing the check of the remaining wand data for the event. On the other hand, a non-zero equal case is possibly caused by clock error, and the event containing this kind of case is saved and regarded as a single spark event, although it is registered as an irregularity for the wand.

The second category, in which D1 is larger than D2, is also further divided into three sub-possibilities, if we consider a small region around the expected fiducial number F, (FL, FU), so that any number which falls within this region is regarded as a fiducial number. Ordinarily, the fact that D1 is larger than D2 means that D2 must have overflowed, and accordingly, D1 would be expected to be a fiducial. So if D1 fall within FL and FU, the event is a regular no-spark case. If D1 is smaller than FL, the fiducial pulse must have been missing in this wand, and this is registered as an irregularity in the wand performance statistics, but is also regarded as a single spark, and the event containing this it is saved. The third case means that the second clock must have been stopped by a spurious pulse slightly beyond the fiducial position while the fiducial pulse was missing with no spark. This is regarded as no spark and registered as an irregularity in the chamber performance report.

The third category is also divided into several sub-cases: If D2 is smaller than FL, it must have been a double spark. If D2 is within FL and FU, it is a single spark. The case where D2 is larger than FU is subdivided into three cases depending on D1. If D1 is smaller than FL, it must have been a single spark while the fiducial pulse was missing. If D1 is within FL and FU, there must have been no spark, and second clock must have been stopped by some spurious spark beyond the fiducial pulse before overflow of the scaler. The third case, where D1 and D2 are larger than FU without overflow, must be a very rare case. There must be no spark and D1 and D2 must have been stopped by two spurious pulses beyond the fiducial pulse, while there was no fiducial pulse at the expected place. The above three subcases are saved, but they are registered as irregularities in the chamber performance report.

All of the above divisions are shown in Fig. 25. Although each wand output of an event goes through the above classifying process, those events are discarded if any three adjacent chambers have double sparks. Very probably those must be double track events, which are of no importance to our objective, and early rejection saves a lot of

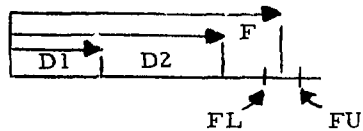

Cases	Possibilities	Decision
D1 = D2;		
1) D1 = D2 = 0	No fire	I(R)
2) D1 = D2 ≠ 0	Possible clock error	I(S)
D1>D2; (D2 is overflow and only D1 is meaningful.)		
1) D1 > FU	Fiducial pulse missing	I(S)
2) D1 < FL	Fiducial pulse missing	I(S)
3) FL ≤ D1 ≤ FU	Regular no spark	G
D1 < D2; (Both D1 and D2 are meaningful.)		
Check D2 first		
1) D2 < FL	Regular double spark	G
2) D2 ≤ FU	Regular single spark	G
3) D2 < FU		
if D1 > FU	Fiducial missing	I(S)
if D1 < FL	Fiducial missing	I(S)
if FL ≤ D1 ≤ FU	No spark	I(S)

G = regular event

I = irregularity

S = save

Figure 25. Classification of each wand data.

computer time.

One more comment to be made is that, even though the fiducial pulses are very stable, the second fiducial is generally less stable, and every once in a while it is missing in some chambers. However, we don't have to discard the whole event in the cases where only one or two fiducials are missing, if we think in terms of maximum use of the collected data. This is the underlying idea in the above treatment of event data. The passage of the group of events in a file gives a report of the statistics of the spark types registered in each wand and the irregularities detected in the process. This information is very useful in estimating the chamber performances after the experiment, and gives an indication whether the whole experimental setup functions properly during data-taking.

3. Sorting of good events and least squares line fit.

After the wand data passes through the classification group; each event goes through the stage that extracts the information about the track, based on wand data obtained from the previous group, sorts out good events while discarding the events which do not meet the triple coincidence rule, and finally checks whether the least squares fit with the wand data makes a straight line plot. Note that in this section we are looking at the wand data collectively, in order to find possible charged particle tracks. Also note that our eventual goal is to determine the single-collision proton spectrum.

Since there are many possible cases in the collected data, in connection with the tracks along the twelve chambers, such as a single collision producing a single track, a double collision giving two separate tracks, a double track involving the same chambers, false triggering by gammas, accidental coincidences, and failures to detect some weak sparks along the tract, etc., the first thing to be done is to distinguish events by the continuity of sparking along the chambers. This is done in the first part of this block. A single track is formed when some number of adjacent chambers are involved. Double scattering usually involves two distinct groups of adjacent chambers. See

figure 26 for the various possible kinds of tracks. Matching conditions between the x-z and y-z planes in sparking should be checked. Since, in the computer, the x-z plane and y-z plane are seen separately to check the tracks, the x-z plane and y-z plane processing is done separately and later compared as to whether the results of the two planes are compatible with each other. Since there occasionally may be some missing sparks along a track due to weak current, the x-z plane sometimes may register a single continuous group of sparking, while the y-z plane forms two continuous groups of sparking along chambers with a middle group of non-sparking chambers and vice versa. These types of events are saved for further test of their linearity by filling the middle sparks in the missing plane by interpolation. However these events that had two compatible, distinct groups of continuous sparking in both planes are discarded at this stage. In the program, this is done as an option, and one can also try these events for a linearity check by interpolation-filling of the middle part. Any events that had less than three chambers sparked in both planes are also rejected at this stage. Therefore only these events that have a high possibility of making a single straight line remain after this processing.

After the above processing, successful events go through a least squares fit check for a straight line plot. However, in a group of chambers which registers continuous sparking, some chambers have double sparks, and it is not known which spark makes the straight line before the fit. Therefore, every possible combination of sparks from each chamber is tried in the least squares line fit and only the combination that gives the minimum deviation from a straight line is tested as to whether it is within the given acceptable error limit for the straight line. This is done separately in the x-z and y-z plane. Those events that give an unacceptable error in any of the two-plane fits are rejected as unwanted events.

The least squares line fit is done in each plane in the following manner: Suppose N continuous chambers sparked as shown in figure 27b. Then the least squares line approximating the set of points $(Z_1, Y_1), (Z_2, Y_2), \cdots, (Z_N, Y_N)$ has the equation

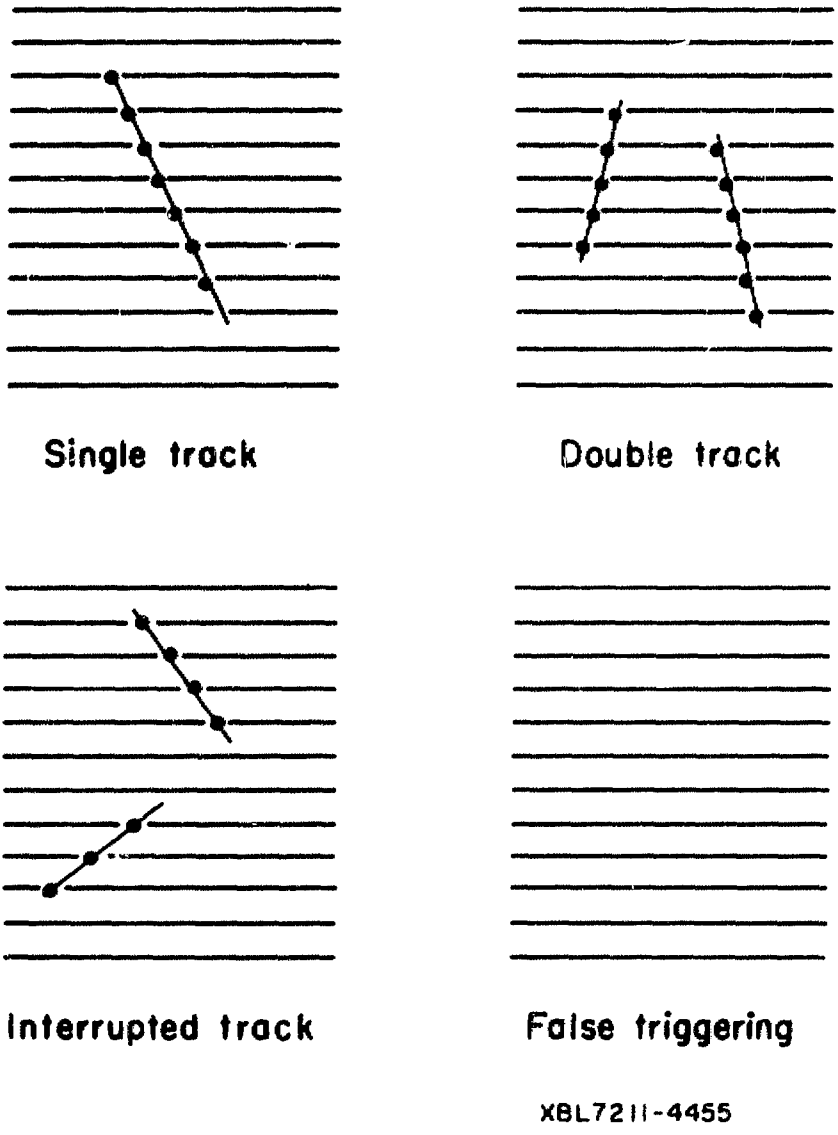

Fig. 26. Cases of tracks detected in the spectrometer.

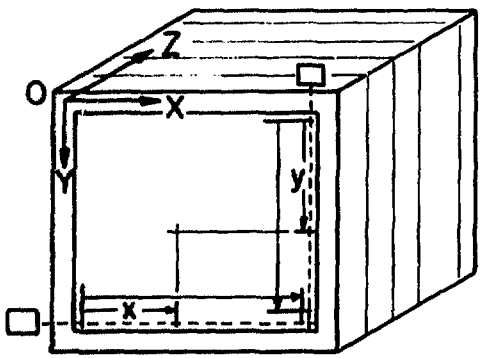

(a) Spectrometer reference coordinate

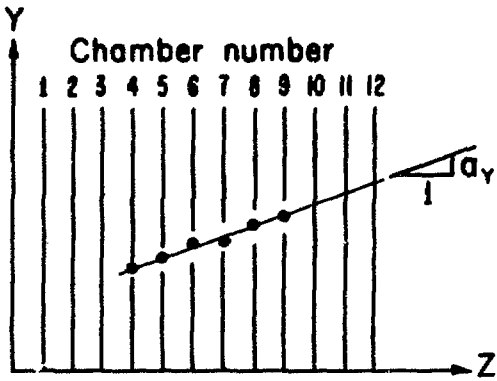

(b) One plane in line fitting

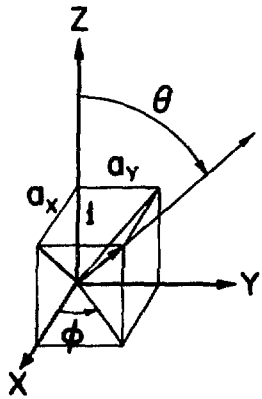

(c) Angle relations with the fitted line slopes

XBL7211-4454

Fig. 27. Spectrometer reference frame and least square line fit.

$$Y = a + b x, \tag{4-1}$$

and the constants a and b are determined by solving the following simultaneous equations requiring a minimum least squares sum,

$$\begin{aligned} \Sigma Y &= a N + b \Sigma Z \\ \Sigma Z Y &= a \Sigma Z + b \Sigma Z^2, \end{aligned} \tag{4-2}$$

which are called the normal equations for the least squares line. The constants a and b of the above equations can be found from the formulas:

$$a = \frac{(\Sigma Y)(\Sigma Z^2) - (\Sigma Z)(\Sigma Z Y)}{N \Sigma Z^2 - (\Sigma Z)^2}$$

$$b = \frac{N(\Sigma Z Y) - (\Sigma Z)(\Sigma Y)}{N(\Sigma Z^2) - (\Sigma Z)^2} \tag{4-3}$$

and the error of the fit is represented as

$$s \sqrt{\frac{\Sigma(Y - Y_{est})}{N}} < \epsilon . \tag{4-4}$$

The error s is a measure of deviations of the data from the fit, and represents only those events which have smaller error than the specified error ϵ are accepted as valid track data.

Once an event is accepted as a line track, the polar and azimuthal angles relative to the spectrometer setup, as shown in figure 27a, are calculated in the following way:

$$\theta = \cos^{-1} \mu = \cos^{-1} (1/\sqrt{(1 + a_x^2 + a_y^2)}); \tag{4-5}$$

$$\phi = \begin{cases} \cos^{-1}(a_x/\sqrt{a_x^2 + a_y^2}) & \text{if } a_y \geq 0 \\ 2\pi - \cos^{-1}(a_x/\sqrt{a_x^2 + a_y^2}) & \text{if } a_y < 0, \end{cases} \tag{4-6}$$

where a_x and a_y are the slopes of the least squares line fits in the x-z and y-z planes, respectively.

4. Proton track length and conversion to energy.

The next step is to calculate the range of the particle track lying within the spectrometer converter medium, and then to calculate its energy from the track length, using range-energy formula. Suppose N sparks are recorded for the track of a proton, and the converter medium thickness of each chamber is ℓ. Then the particle range must lie somewhere between the following two limits:

$$\begin{aligned} R_1 &= (N-1)\,\ell/\cos\theta \\ R_2 &= (N+1)\,\ell/\cos\theta, \end{aligned} \tag{4-7}$$

where θ is the polar angle of the track normal to the chambers. The fact that the spectrometer measurements cannot determine a definite range of the track for the charged particle, but instead only define the region within which the particle range might lie, is clearly a disadvantage, and tends to give a less reliable energy spectrum in the overall result.

Two methods can be used to convert the track information into proton energy. The first method is obviously to use the arithmetical average of the two limits above as the value of the total range of the particle:

$$\overline{R} = \frac{R_1 + R_2}{2} = N\ell. \tag{4-8}$$

In this case, the maximum error is given by $\Delta R_{max} = \ell$. The relative error in energy is obviously dependent on the number of chambers

involved in sparking. The range-energy relationship of protons in polyethylene and in plastic scintillators can be expressed with good accuracy by

$$E = K R^{0.55}. \tag{4-9}$$

Then the relative maximum error in energy will be

$$\frac{\Delta E_{max}}{\bar{E}} = \frac{0.55\, K R^{0.55-1}\, \Delta R_{max}}{K R^{0.55}} = 0.55\, \frac{\Delta R_{max}}{\bar{R}} = \frac{0.55}{N}. \tag{4-10}$$

Therefore, the maximum error for $N = 3$ will be 18%, and for $N = 10$, 5.5%. These errors look rather large, but one should remember that they are maximum possible errors, and the actual errors involved are smaller in most of cases. In this method a "one" is registered in the particular storage bin that represents the energy corresponding to the average track length.

The second method is to distribute the scoring contribution among the energy bins within the above two energy limit corresponding to R_1 and R_2. The error bound by R_1 and R_2 around $\bar{R}$ usually involves several energy bins, and it may be reasonable to distribute the score among those energy bins in proportion to the chance that the proton energy might fall in those energy bins. If one assumes that the protons are equally available in the above energy region, the probability that a certain length track will be detected, when only N chambers are involved, has a triangular shape with the peak at the average range $\bar{R}$ and zeroes at the two limits R_1 and R_2. The contribution into each energy bin is calculated in proportion to the area in its energy interval. In overall result, this method has a tendency to smooth out the energy spectrum. This effect is good in the region around the central part of the spectrum, but it is bad at the edges of the energy spectrum. The program gives both spectrums in the output, and the choice of method depends on the situation and the user. For the proton range-energy formula in the medium, it could be calculated from the well-known Bethe-Bohr stopping formula[27,28] for the specific medium:

$$-\frac{dE}{dx} = \frac{4\pi e^4 z^2 ZNB}{mv^2} \tag{4-11}$$

Table (4-1) shows the stopping power and range of protons in polyethylene, but in the program the previously mentioned approximating formula has been used, with the coefficients shown in Table (3-1) fitted from ref. 29.

Our chambers have frames made with lucite to support the grid wire planes. This lucite supplies unwanted nuclear targets for the neutrons around the edges of the chambers, and also has stopping power for the protons. Even though our spectrometer is surrounded by anti-coincidence scintillators, they are separated by frames from the sensitive area, and presumably many protons from inside the spectrometer are stopped in the frames. Therefore, the effects of the chamber frames must be considered in connection with the acquisition of the proton energy spectrum. Also, many protons are generated inside the frames and go into the spectrometer. These kinds of tracks are not really a major part, but they must be considered. The chambers haven't the ability to distinguish the beginning or end of a charged particle track. Whether the track involves the frames or not can partially be checked by extending the tracks one more chamber distance—both in the forward and backward direction—and checking whether any extended end falls in the frame region. If both extended ends fall inside the sensitive area, there is no doubt that the track was generated and shaped within the sensitive region. However, if the extended end falls in a chamber frame, one cannot be sure whether the track really involved the chamber frame, or if it was stopped or generated before the frame. If one sacrifices the events of the latter type he can, in forming the energy spectrum, reject all of the events whose extensions involve the frame. This action tends to cause the loss of some of the good track events in the data tape, but increases the reliability of the obtained proton energy spectrum. In the program, the forward and backward extensions are options. One should note that, if one uses the above extension and rejection options he should also include the same thing in the particle transport simulation, to be used later for the kernel generation.

Table 4-1

Range of protons in CH_2. (From UCRL-2301.) $\rho = .91$ gr/cc

T MeV	R gm/cm^2	$-\frac{dT}{d\xi}$ MeV-cm^2/gm	T MeV	R gm/cm^2	$-\frac{dT}{d\xi}$ MeV-cm^2/gm
1	1.911×10^{-3}	305.9	200	2.396×10^{1}	4.849
2	6.258	184.8	250	3.507	4.217
3	1.268×10^{-2}	134.6	300	4.762	3.792
4	2.109	107.0	350	6.139	3.489
5	3.136	89.37	400	7.621	3.262
6	4.344	77.10	450	9.198	3.080
7	5.728	68.00	500	1.086×10^{2}	2.949
8	7.284	60.97	600	1.438	2.745
9	9.008	55.36	700	1.812	2.604
10	1.090×10^{-1}	50.77	800	2.205	2.503
12	1.516	43.69	900	2.611	2.428
15	2.272	36.34	1000	3.028	2.371
20	3.834	28.66	1500	5.210	2.229
25	5.756	23.84	2000	7.482	2.189
30	8.023	20.53	2500	9.766	2.184
35	1.062×10^{0}	18.10	3000	1.206×10^{3}	2.194
40	1.355	16.23	3500	1.432	2.210
45	1.678	14.76	4000	1.658	2.229
50	2.032	13.56	4500	1.881	2.250
60	2.828	11.72	5000	2.103	2.270
70	3.736	10.38	6000	2.539	2.312
80	4.752	9.360	7000	2.968	2.348
90	5.872	8.552	8000	3.391	2.383
100	7.090	7.898	9000	3.808	2.415
125	1.054×10^{1}	6.700	10000	4.219	2.445
150	1.454	5.886			

5. Proton energy spectrum generation.

At the start of the program, energy bins are setup according to the given energy interval for a certain range of proton energy. Processing of each event in the raw data tape, as explained above, extracts only the good single-track events, converts track length into energy and distributes the information among the energy bins. Eventually, this process generates a proton energy spectrum as a histogram, which is produced at the end of the processing of each data file.

In addition to the proton energy spectrum histogram, the final output also gives a report on the statistics of chamber performance, spark types, and various irregularities detected in each chamber. It also gives the angular and energy distributions of the detected tracks in terms of the polar-azimuthal angle and the polar and azimuthal angle-energy distributions, in order to help orient the spectrometer setup to the incoming neutrons. Table (4-2) shows some output items from a batch of 500 events, obtained from tests of the spectrometer setup with the 184" cyclotron proton beam.

Table 4.2.-a

```
DATA READ IN ARE--

CARD1-CTINCH,NLIM,NDBLOP,NPEBIN,PELB,PEMA,VV,EROLIM,FCCEK,FCRRTO,IPUNCH,BEXTOP,FEXTOP ARE

   1.0001000   2  27    55.000   305.000    60.610     3.000      .100    10.000
    0  1.0  1.0

CARD2- (IGRAF(I),I=1,9),((IFID(I,J),I=1,12),J=1,2),IDVMU,IDVPHI   ARE

444444444
3535 3531 3535 3534 3535 3536 3535 3536 3531 3536 3533 3537

3524 3522 3516 3520 3520 3523 3525 3524 3525 3523 3524 3523

  10   12


CONVERTER DIMENSIONS IN MM AND EQUIV. PROTON ENERGY IN MEV. ARE --
          CT        CST     THNORM     THDIAG     THPEMA   TH(NPEB)
       25.400    28.685    344.278    480.081    597.769  18253.406

          CTE       CSTE     TNORME     TDIAGE       PEMA PEB(NPEB)
        53.32      57.01     223.92     268.91     305.00   2000.00


A. VARIOUS COUNTERS REPORT.

      NREC     =      100 ---( NO. OF RECORDS IN FILE )

        NPARF  =        1 ---( NO. OF PARITY ERRORS IN FILE )

      LENBIN(  1 ) =        1--(NO. OF RECORDS WHICH HAD EVENTS NUMBER   1 )

      LENBIN(  5 ) =       99--(NO. OF RECORDS WHICH HAD EVENTS NUMBER   5 )
      ------------------------------------------------------------------------

    ERROR COUNTERS IN ORDER OF DETECTIONS

      NEVTF    =      496 ---( NO. OF EVENTS IN FILE )

        NBRITE =-       0 ---( NO. OF BAD LEADING 7 CHECK )

      NGRITE   =      496 ---( NO. OF GOOD LEADING 7 CHECK )

        NFSTPS =-       0 ---( NO. STOPPED BY FID CHECKS. SEE C-1)

        NDTRST =-      26 ---( NO. STOPPED BY DOUBLE TRACK EVENTS)

      NFPASS   =      470 ---( NO. PASSING FID CHECK. SEE C-2 )

        MULSPK =-       1 ---( MULTIPLE SCAT.-LIKE EVENTS )
        NDRSCH =-       0 ---( EVTS. HAVING LESS THAN TWO CH SPARKED
        JWHDIF =-      20 ---( DIFF. JSWICH NO. EVENTS )
        NSAVE  =-      17 ---( SAVED FROM THE ABOVE. )
        INCON1 =-       2 ---( INCON. IN SINGLE SCAT. PASS. SEE C-3)
        NSAVE1 =-       2 ---( SAVED FROM THE ABOVE. )
        INCON2 =-       1 ---( DOUBLE SCAT-LIKE CASE )
        NDDBLS =-       4 ---( DBL SCAT-LIKE EVENTS. SEE C-4 )
        NMPASS =-       0 ---( EVTS. PROCESSED AMONG DBL-LIKE EVTS

      NPASS    =      461 ---( EVENTS PASSED THE CHECKS SO FAR)
        NOLINE =-      52 ---( NO. THAT HAD NO TRACK LINE IN LSQFIT

        NPESCB =-       0 ---( ESCAPED EVENTS BY BACKWARD EXTENTION
        NPESCF =-       2 ---( ESCAPED EVENTS BY FORWARD EXTENTION

      NLINE    =      407 ---( TOTAL EVTS. HAVING TRACK LINES IN LSQ FIT )
      ------------------------------------------------------------------------

   NOTE. CUMULATIVE REPORT INCLUDING THE PREVIOUS FILES ARE--

        NO. OF FILES READ ----       1
        NO. OF RECORDS READ --     100
        NO. OF PARITY-ERRORS -       1
        NO. OF EVENTS READ ---     496
        NO. OF RECORD LENGTH ERROR---       1
```

Table 4.2 - b

B: FIDUCIAL PULSE DISTANCE REPORT IN OCTAL:

1. WHEN FILE PROCESSING STARTS.

CHAMBER NUMBERS	1	2	3	4	5	6	7	8	9	10	11	12
X-AXIS(HORIZONTAL)	3535	3531	3535	3534	3535	3536	3535	3536	3537	3536	3533	3537
Y-AXIS(VERTICAL)	3524	3522	3516	3520	3524	3523	3525	3524	3524	3523	3524	3553

2. WHEN FILE PROCESSING ENDS.

CHAMBER NUMBERS	1	2	3	4	5	6	7	8	9	10	11	12
X-AXIS(HORIZONTAL)	3534	3531	3535	3534	3535	3536	3535	3536	3537	3534	3533	3537
Y-AXIS(VERTICAL)	3524	3523	3517	3520	3524	3523	3524	3524	3525	3522	3523	3552

C: SPARK CHAMBERS PERFORMANCE REPORT.

C-1. FIDUCIAL CHECK ERROR FREQ: IN EACH CHAMBER --- NFDER(I,J,K)

1. X-AXIS (HORIZONTAL)

CHAMBER NUMBERS	1	2	3	4	5	6	7	8	9	10	11	12
NO FIRE	0	0	0	0	0	0	0	0	0	0	0	0
CLOCK ERROR	0	0	0	0	0	0	0	0	0	0	0	0
TOO LONG FID.	0	0	0	0	0	0	0	0	0	0	0	0
TOO SMALL FID.	0	0	0	0	0	0	0	1	0	0	0	0
TOTAL	0	0	0	0	0	0	0	1	0	0	0	0

2. Y-AXIS (VERTICAL)

CHAMBER NUMBERS	1	2	3	4	5	6	7	8	9	10	11	12
NO FIRE	0	0	0	0	0	0	0	0	0	0	0	0
CLOCK ERROR	0	0	0	0	0	0	0	0	0	0	0	0
TOO LONG FID.	0	0	0	0	0	0	0	0	0	0	0	0
TOO SMALL FID.	0	0	1	0	1	0	2	1	2	0	0	1
TOTAL	0	0	1	0	1	0	2	1	2	0	0	1

NOTE-- CLOCK AND TOO SMALL FID ERRORS ARE SAVABLE.

C-2. STATISTICS OF REGULAR DATA IN EACH CHAMBER---CNWND(I,J,K).

1. X-AXIS (HORIZONTAL)

CHAMBER NUMBERS	1	2	3	4	5	6	7	8	9	10	11	12
NO. OF ONE SPARK	447	453	443	446	444	457	447	441	449	438	451	421
NO. OF TWO SPARKS	23	15	25	24	26	13	21	29	19	27	11	43
NO. OF NO SPARK	0	2	2	0	0	0	2	0	2	5	8	6
TOTAL	470	470	470	470	470	470	470	470	470	470	470	470

2. Y-AXIS (VERTICAL)

CHAMBER NUMBERS	1	2	3	4	5	6	7	8	9	10	11	12
NO. OF ONE SPARK	457	462	450	450	455	464	456	453	442	452	408	394
NO. OF TWO SPARKS	13	4	11	20	14	3	14	16	19	12	57	68
NO. OF NO SPARK	0	4	1	0	1	3	0	1	9	6	5	8
TOTAL	470	470	470	470	470	470	470	470	470	470	470	470

V. NEUTRON SPECTRUM UNFOLDING

This chapter describes the method of unfolding the neutron energy spectrum from the proton energy spectrum measured from the spectrometer. The first section explains the general nature of the kernel matrix element which is generated, using a random sampling method, followed by brief introduction to the Monte Carlo principles. The third section gives the detailed sampling procedure, with all of the equations and probability functions used in it, and the second section gives a general description of the differential cross sections which are used in sampling. The fourth section gives some analysis of Monte Carlo results, and the fifth section describes the details of the calculational aspect of the direct least squares method that is used in the numerical unfolding of the neutron energy flux from the measured proton energy spectrum, using the generated kernel matrix.

1. Process simulations

This section explains the detailed procedure involving particle transport and evaluation of the kernel matrix element in the random sampling process, with a brief account of the Monte Carlo principle.

The basic quantity we are going to estimate, using the random sampling method, is the kernel matrix element K for each set of neutron and proton energy points E_n, E_p, which are needed in the numerical procedure of the unfolding process. The kernel matrix element for a set of E_n, E_p is represented from Chapter II as

$$K(E_n, E_p) = \frac{\int_{V_m} d\underset{\sim}{r}\, \phi_0\,(\underset{\sim}{r}, E_n)\, \Sigma_{np}(E_p) f_p(E_n, E_p) d_0(\underset{\sim}{r}, E_p)}{A\,\Phi\,(E_n)} \quad . \qquad (5\text{-}1)$$

Here the denominator on the right hand side represents the total number of neutrons coming into the spectrometer volume through its front face, and the numerator represents the total number of protons detected inside the spectrometer volume without escaping among the protons generated by collisions of the unscattered neutrons within the spectrometer. Particle transport inside the spectrometer volume, when neutrons of

of energy E_n come into it through its front face, can be simulated exactly, using known nuclear parameters and scattering kinemetics. The above quantity can be obtained by collecting the non-escaping single track events whose energy is E_p and lies within the detector volume when neutrons of energy E_n are injected, and forming the ratio to the number of injected neutrons $A\Phi(E_n)$. The chance that each injected neutron will form a non-escaping single proton track is formed in principle by the product of four probabilities, when the neutrons are injected into the spectrometer volume:

a) the probability that an injected neutron will make a collision inside the spectrometer volume;

b) the probability that the above collision will eject a proton of energy E_p, i.e., $f_p(E_n, E_p)$;

c) the probability that the range of the above ejected proton will lie within the spectrometer volume, i.e., the non-escaping probability (in the actual case, the additional condition that a minimum of 3 chambers must spark is also imposed);

d) the probability that the scattered neutron, which emerges from the collision together with the proton, will make no further interactions inside the spectrometer volume before leaving it.

Note here that in item (b) $f_p(E_n, E_p)$ has a constant value for a fixed set of energies (E_n, E_p) and can be multiplied later, if the sampling is designed so that in the first neutron collision of energy E_n, only protons of energy E_p are ejected. This trick of using expected values usually reduces sampling variance and saves computer time in actual sampling, and was used to advantage in this case, where actual sampling was done by injecting neutrons into the spectrometer through its front face and collecting only the above type events. Before we go into more specific details of sampling procedure, a brief account of the fundamental principles of the random sampling method will be described.

The usual applications of the Monte Carlo method lead to the evaluation of integrals and depend on the following two theorems:[30]

Theorem I (The Strong Law of Large Numbers)[31]

If a sequence of N random variables x_1 to x_N are picked from the probability density function (p. d. f.) f(x), and a random variable $\mathfrak{z}_N$ is defined by the equation

$$\mathfrak{z}_N = \frac{1}{N} \sum_{1}^{N} z(x_i), \tag{5-2}$$

and if the integral

$$z = \int_{-\infty}^{\infty} z(x)f(x)dx \tag{5-3}$$

exists in the ordinary sense, $\mathfrak{z}_N$ almost always will approach $\bar{z}$ as a limit as N approaches ∞ .

The integral (5-3) is called the expected value of the function z(x), and $\mathfrak{z}_N$ is called an estimate of $\bar{z}$. If $\overline{z^2}$, the expected value of $z^2(x)$, also exists, an estimate can be made about the amount that $\mathfrak{z}_N$ deviates from $\bar{z}$ for large N. Denote the variance of z(x) by either σ^2 or V, which is then defined by the equation

$$\begin{aligned}
\sigma^2 = V &= \overline{(z - \bar{z})^2} \\
&= \int (z-\bar{z})^2 f(x)dx \\
&= \int z^2 f(x)dx - 2\bar{z}\int zf(x)dx + \bar{z}^2 \int f(x)dx \\
&= \overline{z^2} - 2\bar{z}^2 + \bar{z}^2 \\
&= \overline{z^2} - \bar{z}^2
\end{aligned} \tag{5-4}$$

and then apply the following Theorem II.

Theorem II (The Central Limit Theorem)[32]

For large N the probability that the event $\bar{z} - \delta \leq \mathfrak{z} \leq \bar{z} + \delta$ occurs is assymptotically independent of the exact nature of z(x) or f(x), but depends only on N and σ^2. In fact,

$$\text{Prob.}\left\{\mathfrak{z} \le \bar{z} + \delta\right\} = \sqrt{\frac{1}{2\pi}} \int_{-\infty}^{\frac{\delta}{\sigma}\sqrt{N}} e^{-x^2/2}\, dx$$

$$+ \text{ terms of order } \frac{1}{\sqrt{N}}. \qquad (5\text{-}5)$$

The probability that the deviation of $\mathfrak{z}$ from $\bar{z}$ will exceed $\pm\lambda(\sigma/\sqrt{N})$ is given in the following abbreviated table of

$$\sqrt{\frac{2}{\pi}} \int_{\lambda}^{\infty} e^{-x^2/2}\, dx:$$

λ	Probability
0.6745	0.5000
1.0000	0.3173
2.0000	0.0455
3.0000	0.0027
4.0000	0.0001

It can be seen from the table that deviations greater than $\pm\sigma/\sqrt{N}$ will be frequent, deviations greater than $\pm 2\sigma/\sqrt{N}$ not common, and deviations greater than $\pm 3\sigma/\sqrt{N}$ so uncommon that, if the table applies, the probability that this last event might occur can usually be ignored. $\sigma/\sqrt{N}$ is called the standard deviation of the estimate $\mathfrak{z}_N$.

However, one should note that in actual practice it is rarely efficient to use Monte Carlo methods unless the integral is very complicated or highly multidimensional. On the whole, it is admitted that the Monte Carlo method has not shown up very well in competition with standard techniques, when the standard techniques were at all reasonable. However, it has been used very successfully where the standard numerical techniques completely fail. In this sense it is generally a method of last resort.

The results of Theorem II depend on N being large enough and the variance being known. The variance can be estimated by

$$\hat{V} = \frac{N}{N-1} (\widehat{z^2} - \hat{z}^2) , \tag{5-6}$$

where of course

$$\hat{z}^2 = \frac{1}{N} \sum_{1}^{N} z^2(x_i)$$

$$\hat{z} = \frac{1}{N} \sum_{1}^{N} z(x_i) . \tag{5-7}$$

In general, whenever it is desirable to estimate values of a formula in which $\overline{z^2}$ and $\overline{z}$ are involved, the expected values can be replaced by $\widehat{z^2}$ $\hat{z}$, respectively. While the estimate will almost always be biased, the amount of the bias is usually proportional to $1/N$, and can be ignored if N is reasonably large.

The error in the estimate of $\overline{z}$ is measured by $\sigma/\sqrt{N}$. There are two ways to make this error small—to increase N, i.e., the number of samples, or to change the sampling technique to make σ small. The extent to which each of these alternatives should be used depends on the relative cost of each for the problem to be done. Even though there are numerous sampling techniques available for reducing σ,[33] we shall use a more or less straight forward sampling method, occasionly combined with the systematic sampling technique, use of expected values and a splitting technique in some parts of the program.

2. Cross sections

As a preliminary step to explain the specific sampling procedure in the next section, this section will deal with the various cross sections of n-p and n-C interactions. Generally, we need two pieces of information about the individual interactions, namely, the total cross section $\sigma(E')$ which gives the probability of interaction size per nucleus, depending upon the energy of the incoming neutron E', and the function $c(E')f(\underset{\sim}{E}' \rightarrow \underset{\sim}{E})$ which gives the probability of the energy and direction of the outcoming particles from the interaction, relative to the incoming particle direction when c particles come out from the interaction. Here also we shall

use the energy variable E as a kinetic variable of the particle. The notation $\underset{\sim}{E}$ is used as shorthand for $(E, \underset{\sim}{\Omega})$, thus $d\underset{\sim}{E}$ denotes $dEd\underset{\sim}{\Omega}$. Note that $f(\underset{\sim}{E}' \rightarrow \underset{\sim}{E})$ is a purely probabilistic density function which satisfied the usual normalization condition over $dEd\underset{\sim}{\Omega}$. Then the unit of the function $c(E')f(\underset{\sim}{E}' \rightarrow \underset{\sim}{E})$ is the number of emitted particles per MeV per steradian per collision. Sometimes $c(E')f(\underset{\sim}{E}' \rightarrow \underset{\sim}{E})$ will be denoted as $F(\underset{\sim}{E}' \rightarrow \underset{\sim}{E})$.

From the standpoint of statistics, if one assumes azimuthal symmetry in interaction, the function $f(\underset{\sim}{E}' \rightarrow \underset{\sim}{E})$ is a joint probability density function of two random variables with a parameter E', and it can generally be decomposed into a product of two probability density functions, i.e., marginal p.d.f. and conditional p.d.f., as

$$f(\underset{\sim}{E}' \rightarrow \underset{\sim}{E}) = f_1(E;E')\, f_2(\underset{\sim}{\Omega}\cdot\underset{\sim}{\Omega} \mid E;E'), \tag{5-8}$$

where

$$f_1(E;E') \equiv \int_{4\pi} f(\underset{\sim}{E}' \rightarrow \underset{\sim}{E})\, d\underset{\sim}{\Omega} = \int_{-1}^{1} d\mu \int_0^{2\pi} d\phi\, f(E', \underset{\sim}{\Omega}' \rightarrow E\underset{\sim}{\Omega})\, d\phi\, d\mu \tag{5-9}$$

$$f_2(\underset{\sim}{\Omega}\cdot\underset{\sim}{\Omega} \mid E;E') = \frac{f(\underset{\sim}{E}' \rightarrow \underset{\sim}{E})}{f_1(E;E')} = \frac{f(E', \underset{\sim}{\Omega}' \rightarrow E, \underset{\sim}{\Omega})}{f_1(E;E')}, \tag{5-10}$$

and of course f_1 and f_2 satisfy the following normalization conditions:

$$\int_0^{\infty} f_1(E;E')\, dE = 1 \tag{5-11}$$

$$\int_{4\pi} f_2(\underset{\sim}{\Omega}'\cdot\underset{\sim}{\Omega} \mid E;E')\, d\underset{\sim}{\Omega} = 1\,. \tag{5-12}$$

Here $f_1(E;E')$ is the marginal p.d.f. of E irrespective of the emerging direction, and $f_2(\underset{\sim}{\Omega}'\cdot\underset{\sim}{\Omega} \mid E;E')$ is the conditional p.d.f. that the emerging direction will be $\underset{\sim}{\Omega}$, given that the emerging particle energy is E.

n-p interaction

The basic physics of n-p interactions has been described in Chapter II, and elastic scattering was said to be the only mode of interaction in our energy range. The total n-p scattering cross section in this energy range is well represented by the following two formulas: Gammel's semiempirical formula:[20]

$$\sigma_G(E'_n) = \frac{3\pi}{A} + \frac{\pi}{B} \text{ barns for } E_n \leq 42 \text{ MeV}, \tag{5-13}$$

with

$$A = 1.206\ E'_n + (-1.86 + 0.09415 + 0.000\ 1306\ E'^2_n)^2$$
$$B = 1.206\ E'_n + (0.4223 + 0.13\ E'_n)^2$$

and

Metropolis' empirical formula:

$$\sigma_M(E'_n) = \frac{34.10}{\beta^2} - \frac{82.2}{\beta} + 82.2 \text{ millibarns} \tag{5-14}$$

$$\text{for } 25 \text{ MeV} \leq E_n \leq 630 \text{ MeV}$$

with $\beta = \frac{v}{c}$,

where E'_n is in MeV in the Laboratory system and β is the corresponding neutron velocity in velocity of light units. Gammel's formula fits the

experimental values within ~ 1% below 42 MeV and Metropolis formula gives about 6% accuracy between 25 and 630 MeV. Figure 28 shows how well these formulas fit the experimental data in the above energy ranges. As to the n-p differential scattering cross section, as explained in Chapter II, Gammel's representation in the center of mass system, equation (2-26), is assumed to be true below 42 MeV. Then

$$\sigma_H(\mu_c, E'_n) = \sigma_H(E'_n)\, f_{1H}(\mu_c; E'_n)$$

$$= \sigma_G(E'_n) \cdot \left[\frac{1}{4\pi} \cdot \frac{1 + 2\left(\frac{E'_n}{90}\right)^2 \mu_c^2}{1 + \frac{2}{3}\left(\frac{E'_n}{90}\right)^2} \right] \text{ barn/ster for } E_n \lesssim 42 \text{ MeV}, \tag{5-15}$$

with $b = 2\left(\frac{E'_n}{90}\right)^2$,

where E'_n is the incident neutron energy in MeV in the Laboratory system and μ_c is the cosine of the neutron scattering angle θ_c in the CM system. However, above 42 MeV the above expression is not adequate for the representation of n-p differential scattering cross sections, and there is no simple formula in this energy region. Nonetheless there are a large amount of experimental data available from the literature in this energy range, and the author and his collaborators have tried to fit the above experimental data by a least squares method, using the following functional form at those discrete points of incident neutron energy where experimental data are available.

$$\sigma_{np}(\theta_c, E'_n) = \frac{\sigma_M(E'_n)}{4\pi}\left[A\left(\frac{1 + 2\left(\frac{E'_n}{90}\right)\cos^2\theta_c}{1 + \frac{2}{3}\left(\frac{E'_n}{90}\right)^2}\right) + B\,(\cos^3\theta_c)\right.$$

$$\left. + C(\cos^4\theta_c) + D(\sin\theta_c) + E(\sin 2\theta_c) + F(\sin 4\theta_c) + G\right], \qquad (5\text{-}16)$$

where $\sigma_M(E'_n)$ is the Metropolis formula in equation (5-14) and E'_n and θ_c are the same as in equation (5-15). The experimental data of differential n-p scattering cross sections used in our fittings were obtained from the Experimental Cross Section Information Library of the Lawrence Livermore Laboratory. In the above fitting expression, Gammel's form is the primary term and $\cos^3\theta$ and $\cos^4\theta$ terms were added as suggested by Gammel in this energy range.[20] The rest of the terms were selected rather arbitrarily to give the best fit. Generally, the total scattering cross section data are more reliable than those for differential cross sections, and in the fitting procedure, the following condition was imposed so that the differential cross sections should satisfy the total scattering cross section on integration over the whole solid angle:

$$\sigma_{tot}(E'_n) = \int_{4\pi} \sigma_{np}(\theta_c, E'_n)\,d\underset{\sim}{\Omega}\,. \qquad (5\text{-}17)$$

In fact, the calculation scheme was set up in such a way that it automatically satisfies this normalization condition to the total cross section in applying the least squares method.[34] Table (5-1) shows the fitting coefficients which give best fit for each discrete energy of incident neutron energies where experimental data are available, and figures in the Appendix show the curves fitted with the experimental data. For the energies between the discrete energy points, the differential cross sections are obtained by interpolation in the CM system.

In the simulation procedure in the next section we need to know differential cross sections in terms of laboratory energies. These can be obtained from equation (5-16), using the following two kinematical relationships between the neutron scattering angle θ_c in the CM system and the recoil proton energy E_p in the Laboratory system:

$$\sigma_{np}(\theta_c, E'_n)\, 2\pi\, d(\cos\theta_c) = \sigma_{np}(E'_n, E_p)\, dE_p \tag{5-18}$$

and

$$\cos\theta_c = 1 - 2\,\frac{E_p}{E'_n}\,. \tag{5-19}$$

Then the desired form is

$$\sigma_{np}(E'_n, E_p) = \sigma_{np}(\theta_c, E'_n)\, 2\pi \left| \frac{d(\cos\theta_c)}{dE_p} \right|$$

$$= \sigma_{np}(\theta_c, E'_n)\, \frac{4\pi}{E'_n} \tag{5-20}$$

$$= \sigma_M(E'_n)\, f_{1H}(E_p; E'_n)\,,$$

where $\sigma_{np}(\theta_c, E'_n)$ is provided by equation (5-16), and sinusoidal terms in it are converted by equation (5-19) into the functions of E'_n, E_p. This is the marginal p.d.f. of E_p, irrespective of recoil angle of the outcoming proton, and its behavior with energy is shown in Fig. 29a and b.

The recoil proton angle θ_p in the Laboratory system, when the incoming neutron energy E'_n and the recoil proton energy E_p are given in the Laboratory frame, is determined by

$$\cos\theta_p = \left[\frac{E_p(E'_n + 2\,E_{on})}{E'_n(E_p + 2\,E_{on}} \right]^{1/2} \tag{5-21}$$

from the relativistic kinematics.[21] Here E_{on} is the rest mass energy of a neutron, which is 939.550 MeV. The neutron scattering angle in the Laboratory system is obtained similarly from $E_n = E'_n - E_p$.

$$\cos\theta_n = \left[\frac{E_n(E'_n + 2\,E_{on})}{E'_n(E_n + 2\,E_{on})} \right]^{1/2} \tag{5-22}$$

Here one should not forget that the incoming neutron direction and outgoing proton and neutron directions are in the same plane, in order to conserve momentum. These angles are needed in the determination of path of emerging particles in the sampling procedure. The conditional

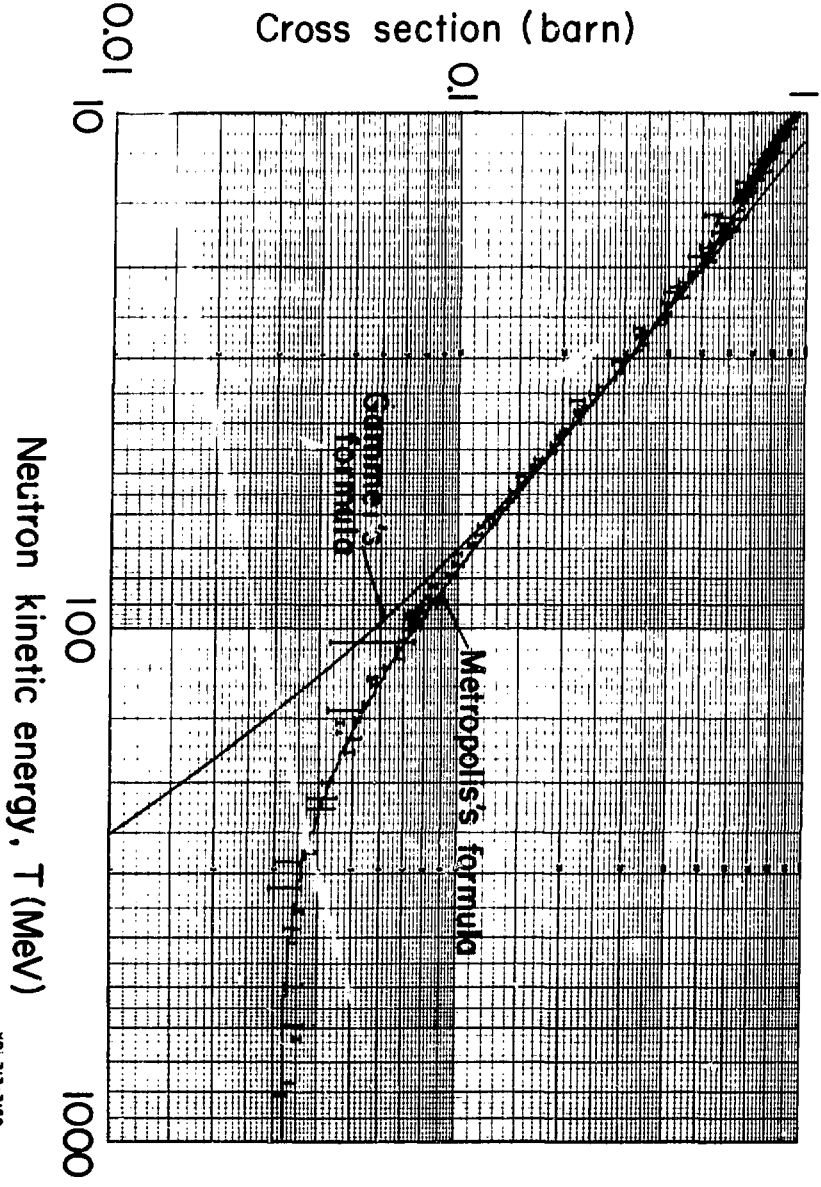

Fig. 28. Total n-p cross section data with fitting formulas

Table 5.1.

FITTING FORMULA COEFFICIENTS FOR THE C.M. DIFF. SCATT. X-SECTIONS

T(MEV)	A	B	C	D	E	F	G
22.5	8.799E-01	-1.481E-02	-6.651E-02	0.	0.	0.	1.334E-01
27.5	-7.428E-01	3.215E-02	1.666E-01	0.	0.	0.	1.709E+00
28.4	-4.987E-01	-3.694E-02	1.819E-01	0.	0.	0.	1.462E+00
32.5	6.528E-01	-1.332E-02	1.188E-01	6.795E-02	7.297E-02	-1.095E-02	2.701E-01
37.5	4.375E-01	2.157E-03	-2.839E-01	-4.506E-01	5.698E-02	-1.081E-02	9.732E-01
42.5	8.902E-01	3.437E-02	-6.942E-01	-8.363E-01	2.629E-02	1.916E-02	9.055E-01
47.5	3.307E-01	4.451E-02	9.322E-02	-2.336E-01	3.064E-02	2.292E-02	8.342E-01
52.5	-8.409E-02	5.159E-02	5.668E-01	-9.561E-02	1.518E-02	1.756E-04	1.046E+00
57.5	-4.460E-02	5.211E-02	7.227E-01	-1.138E-02	2.665E-02	-1.237E-02	9.090E-01
62.5	4.536E-01	5.194E-02	4.514E-01	1.611E-02	1.599E-02	7.504E-02	4.434E-01
70.0	4.336E-01	-4.610E-02	2.084E-01	-5.318E-01	9.802E-02	4.248E-02	9.424E-01
80.0	3.107E-01	-1.775E-02	-5.047E-01	-1.313E+00	4.404E-02	-4.296E-02	1.822E+00
91.0	2.585E-01	-7.040E-02	-5.259E-01	-1.665E+00	-6.674E-04	5.871E-02	2.155E+00
99.0	6.168E-01	-2.012E-01	-6.357E-01	-1.297E+00	-8.475E-03	6.285E-02	1.529E+00
105.0	3.095E-01	-1.003E-01	-9.398E-01	-2.252E+00	-8.379E-03	1.009E-01	2.648E+00
108.5	3.262E-01	-1.377E-01	-8.891E-01	-2.118E+00	-1.181E-01	2.838E-02	2.515E+00
120.0	7.326E-02	-1.617E-01	7.956E-01	-7.141E-01	3.930E-02	3.708E-02	1.328E+00
130.0	-3.386E-01	-4.356E-01	-3.325E-02	-2.592E+00	-4.518E-02	8.249E-02	3.381E+00
137.0	2.200E-01	-1.891E-01	5.893E-01	-6.526E-01	-2.426E-01	-1.331E-02	1.175E+00
150.0	-2.312E-02	-1.521E-01	-1.094E-01	-2.412E+00	-1.069E-02	1.039E-01	2.939E+00
156.0	-7.533E-02	-5.355E-02	1.018E-02	-2.160E+00	-2.362E-01	2.060E-02	2.770E+00
172.0	-1.412E+00	-5.626E-01	5.776E-01	-5.753E+00	3.887E-01	2.147E-01	6.815E+00
200.0	-9.141E-01	-1.679E-01	-1.199E+00	-6.170E+00	-1.554E-01	-2.006E-02	7.000E+00
215.0	-7.336E-01	-1.177E-01	-9.291E-01	-6.365E+00	1.031E-02	3.960E-02	6.918E+00
260.0	-1.055E+00	1.886E-01	-2.946E-01	-6.667E+00	-2.046E-01	-4.154E-02	7.349E+00
300.0	-3.204E-01	-8.375E-01	-1.796E+00	-4.872E+00	3.462E-01	1.572E-01	5.506E+00
380.0	-1.445E+00	5.832E-03	-1.417E+00	-9.114E+00	-3.569E-02	-4.361E-02	9.926E+00
400.0	-7.619E-01	-9.052E-01	-3.060E+00	-8.174E+00	4.112E-01	1.377E-01	8.794E+00
580.0	-7.528E-01	2.333E-01	-1.544E+00	-7.034E+00	2.673E-01	-5.861E-02	7.586E+00
630.0	-9.030E-01	7.137E-01	-1.528E+00	-7.732E+00	-5.974E-02	-1.524E-01	8.281E+00

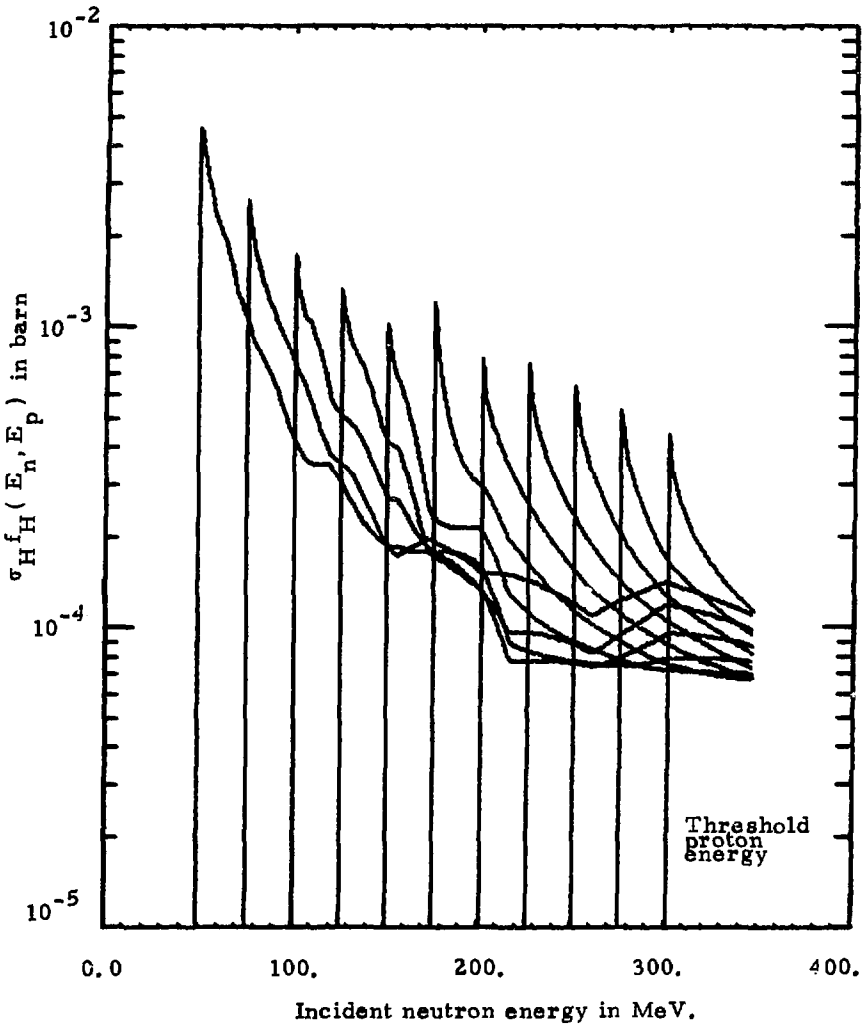

Fig. 29-a. Differential cross section of n-p scattering reaction as a function of incident neutron energy for a set of different threshold proton energies.

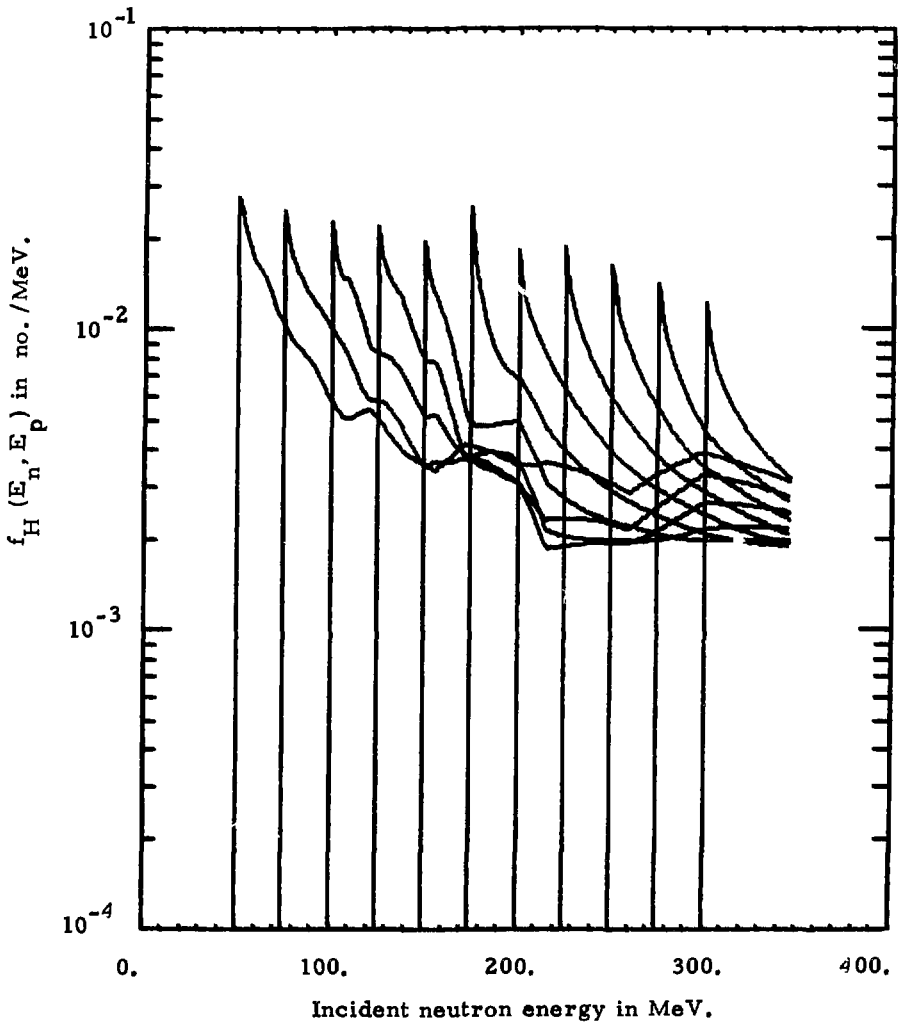

Fig. 29-b. Proton emission spectra of n-p scattering reaction as a function of incident neutron energy for a set of different threshold proton energies.

p. d. f. of θ_p, given E'_n and E_p, in the sense of equation (5-10) and (5-12), is mathematically represented as

$$f_{2H}(\underset{\sim}{\Omega} \mid E_p;E'_n) = f_{2H}(\theta_p, \phi_p \mid E_p;E'_n)$$

$$= \frac{1}{2\pi}\,\delta\left\{\theta_p - \cos^{-1}\left(\left[\frac{E_p(E'_n + 2\,E_{on})}{E'_n(E_p + 2\,E_{on})}\right]^{1/2}\right)\right\} \text{per ster.} \qquad (5\text{-}23)$$

where θ_p and ϕ_p are polar and azimuthal angles of the recoil proton in the Laboratory system and δ means a delta function.

Two remarks will be made before we proceed to the n-C interactions. First, regarding the sum of $\theta_n + \theta_p$ in the Laboratory system, it is a well known fact that in the n-p scattering in the non-relativistic case the sum is 90° or $\pi/2$ radian.[21] However, in the relativistic case this sum tends to decrease slowly with increasing energy, peaking in the middle of 90°.[35] The decrease is small and I don't think it has any appreciable effect in our spectrometer. The next remak concerns the viewing of the differential cross section as a function of the neutron Laboratory scattering angle summed over the azimuthal angle. When we use an angle as an independent random variable, the differential cross section should be multiplied by the Jacobian sin θ_c in the CM system. This gives the effect of a fairly sharp peak at 45° in the Laboratory system in the low energy region where the differential cross section is uniform in the CM system. However, at higher energies, the differential cross section in the CM system is more or less symmetrical about 90°, peaking in the forward and backward direction, and in the Laboratory system when θ_n is used as an independent random variable, this shows the splitting of the above peak into two maxima. Thus at higher energies it is most likely that E_n is large and E_p small, or vice versa,[35] while at low energies equipartition of E'_n into E_p and E_n is most likely.

n-C interaction

The basic physics of this interaction in our energy range has also been explained in Chapter II, and here we introduce the analytic fits done by Alsmiller, et al.[11] to the intranuclear-cascade data generated by H. W. Bertini.[4] Alsmiller, et al. carried out this analytic fitting

for many target elements when both neutrons and protons are incident on the elements. Analytic expressions are given for

1. the non-elastic cross section as a function of energy;

2. the cascade neutron- and proton-emission spectra in the angular intervals 0-30°, 30-60°, 60-90°, and 90-180°;

3. the evaporation neutron- and proton-emission spectra (assumed isotropic); and

4. the cascade neutron- and proton-emission spectra integrated over all angles.

Here we shall introduce only items 1, 2 and 4 when a neutron is incident and a carbon nucleus is the target. The evaporation process is of negligible importance to us since it involves lower energies, roughly below 40 MeV.

For the nonelastic cross section, the following analytic form was used in fitting:

$$\sigma(E') = \frac{1}{400} \exp\left[\sum_{j=0}^{N} a_j \left(\frac{E}{400}\right)^j\right], \text{ mb} \tag{5-24}$$

where the a_j's are coefficients to be determined and E is in MeV, and the following quantity has been minimized with respect to a_j's in the least squares fitting procedure:

$$R = \sum_{E_i} \left[\log 400\ \sigma_{E_i} - \sum_{j=0}^{N} a_j \cdot \left(\frac{E}{400}\right)^j \right]^2 . \tag{5-25}$$

The fitting gives the following a_j's for n-C interactions:

a_0	a_1	a_2	a_3	a_4
12.382795	-5.4469868	11.550725	-11.297047	4.2141600

Figure 30 shows this analytic fit with Bertini's Monte Carlo data.

The cascade particle-emission spectra integrated over all angles was obtained using the functional form:

$$F(E;E_0) \equiv c(E_0)f(E;E_0) = \frac{1}{E_0} \exp\left[\sum_{j=0}^{N} a_j \left(\frac{E}{E_0}\right)\right]^j \tag{5-26}$$

TABLE 5.2.

NEUTRONS INCIDENT ON C

EMIN # 0.871 (MEV)

from ORNL-4046, p84

PROTONS EMITTED

EO (MEV)	ANG. INT.	AC	A1	A2	A3	A4	A5	NO. EMIT.	ENERGY EMIT./EO	EMAX /EO
25	0 - 180	6.3879918E-01	-1.1632667E 01	6.1106633E 01	-1.8579578E 02	2.5667729E 02	-1.2729611E 02	0.420	0.1471	0.917
50	0 - 180	1.0514362E 00	-8.7390893E 00	2.6406887E 01	-6.9863339E 01	9.5568873E 01	-4.6547045E 01	0.619	0.2054	0.963
100	0 - 180	1.5544686E 00	-1.4982067E 01	4.9278550E 01	-9.1401166E 01	8.7994570E 01	-3.3670345E 01	0.794	0.2706	0.984
150	0 - 180	1.7477183E 00	-2.2004878E 01	1.0763407E 02	-2.6275304E 02	2.9430469E 02	-1.2071964E 02	0.844	0.2885	0.976
200	0 - 180	1.8056439E 00	-1.9420854E 01	8.6481911E 01	-2.0650736E 02	2.3045571E 02	-9.4071699E 01	0.900	0.2955	0.983
250	0 - 180	1.9115806E 00	-1.7335598E 01	4.8598961E 01	-6.1334863E 01	2.7909490E 01	0.	0.918	0.2900	0.993
300	0 - 180	1.8913446E 00	-2.0312262E 01	7.5106176E 01	-1.4644950E 02	1.3939885E 02	-5.0177654E 01	0.876	0.2917	0.988
350	0 - 180	1.9812979E 00	-1.9104650E 01	5.3355684E 01	-6.5215783E 01	2.8795457E 01	0.	0.904	0.2903	0.993
400	0 - 180	1.8955539E 00	-1.5653124E 01	3.9200392E 01	-4.7557139E 01	2.2073417E 01	0.	0.924	0.2832	0.990

NEUTRONS EMITTED

EO (MEV)	ANG. INT.	AC	A1	A2	A3	A4	A5	NO. EMIT.	ENERGY EMIT./EO	EMAX /EO
25	0 - 180	6.4987518E-01	-9.2441963E 00	4.7220611E 01	-1.3675431E 02	1.7999482E 02	-8.5473866E 01	0.564	0.2171	0.964
50	0 - 180	1.2060275E 00	-1.0178925E 01	3.5402357E 01	-7.5117560E 01	8.3485591E 01	-3.6249574E 01	0.859	0.3282	0.972
100	0 - 180	1.5932997E 00	-1.2070468E 01	3.9642700E 01	-7.2661155E 01	7.0364777E 01	-2.7643990E 01	1.154	0.4390	0.980
150	0 - 180	1.9723459E 00	-2.0490403E 01	1.0401333E 02	-2.5653343E 02	2.8942295E 02	-1.1581719E 02	1.329	0.4983	0.984
200	0 - 180	2.0259154E 00	-1.8681913E 01	8.0957105E 01	-1.7715261E 02	1.8622985E 02	-7.4254697E 01	1.422	0.5399	0.990
250	0 - 180	2.1607233E 00	-2.2092114E 01	1.0095085E 02	-2.1871792E 02	2.2044607E 02	-8.3227739E 01	1.487	0.5735	0.994
300	0 - 180	2.1493860E 00	-1.9795305E 01	9.1504624E 01	-2.1291865E 02	2.3270836E 02	-9.4402988E 01	1.554	0.5847	0.988
350	0 - 180	2.0467743E 00	-1.9012332E 01	8.4643456E 01	-1.7925537E 02	1.7444684E 02	-6.2705370E 01	1.573	0.6220	0.990
400	0 - 180	2.2182243E 00	-1.8775260E 01	7.8315976E 01	-1.6168694E 02	1.5690703E 02	-5.6661327E 01	1.688	0.6389	0.993

TABLE 5.3.

NEUTRONS INCIDENT ON C

PROTONS EMITTED

EMIN = 0.871 (MEV)

from ORNL-4046, p 25

EO (MEV)	ANG. INT.	A0	A1	A2	A3	A4	A5	NO. EMIT.	ENERGY EMIT./EO	EMAX /EO
25	0 - 30	-6.4117976E-01	-8.6290736E 00	2.1393453E 01	-1.5314557E 01	0.	0.	0.156	0.0699	0.916
	30 - 60	-1.7182376E 00	3.0424412E 00	-3.4093238E 01	8.9384487E 01	-9.4470529E 01	3.1912042E 01	0.189	0.0627	0.886
	60 - 90	2.9518770E-01	-7.7704060E 01	7.7895681E 02	-3.6479889E 03	7.5845647E 03	-5.7158269E 03	0.065	0.0119	0.551
	90 -180	0.	0.	0.	0.	0.	0.	0.012		
50	0 - 30	-5.6122807E-01	-7.7591252E 00	1.4648871E 01	-7.4770729E 00	0.	0.	0.193	0.0968	0.962
	30 - 60	-5.8111326E-01	-6.9960666E 00	5.2881505E 00	1.9799778E 01	-4.0799161E 01	1.8926803E 01	0.287	0.0841	0.926
	60 - 90	-1.0189220E 00	-1.4339928E 01	6.2858148E 01	-1.6046026E 02	1.2505679E 02	0.	0.124	0.0199	0.597
	90 -180	-2.6188844E 00	-2.1386651E 01	8.6126248E 01	-1.5809745E 02	0.	0.	0.026	0.0026	0.270.
100	0 - 30	-4.5043561E-01	-1.1340668E 01	2.9154161E 01	-4.4473137E 01	5.3750681E 01	-2.7875702E 01	0.225	0.1295	0.984
	30 - 60	-7.6139371E-01	-6.4216444E 00	-1.4271622E 01	1.2537734E 02	-2.1024852E 02	1.0306785E 02	0.315	0.1059	0.896
	60 - 90	-4.1967847E-01	-2.0055805E 01	9.0177184E 01	-1.5949410E 02	1.3719026E 02	0.	0.188	0.0283	0.578
	90 -180	-7.2326279E-01	-7.7947981E 01	9.0112027E 02	-4.3506297E 03	6.7942827E 03	0.	0.067	0.0053	0.256
150	0 - 30	-3.3661134E-01	-2.8007717E 01	1.4889149E 02	-3.5485067E 02	3.9539030E 02	-1.6287404E 02	0.226	0.1425	0.976
	30 - 60	-3.7875932E-01	-1.6019848E 01	7.2828984E 01	-1.5433484E 02	1.5892653E 02	-6.9394302E 01	0.344	0.1091	0.839
	60 - 90	-2.4809762E-01	-4.0633004E 01	3.8801233E 02	-1.6856957E 03	3.2163233E 03	-2.2643225E 03	0.194	0.0312	0.535
	90 -180	-1.3372796E 00	-1.6490154E 01	-1.2988376E 01	-2.7322530E 01	3.7490783E 02	0.	0.085	0.0052	0.269
200	0 - 30	-2.4993150E-01	-1.8274240E 01	7.2070588E 01	-1.5552774E 02	1.7958195E 02	-7.8621223E 01	0.246	0.1514	0.983
	30 - 60	-5.9512441E-01	-1.0810527E 01	4.3260031E 01	-7.7022272E 01	5.9564553E 01	-1.9181827E 01	0.363	0.1174	0.852
	60 - 90	1.1479608E-01	-4.6371657E 01	5.0038502E 02	-2.5995629E 03	6.0330532E 03	-5.1511379E 03	0.222	0.0298	0.455
	90 -180	-1.2573084E 00	-1.9266301E 01	1.2484397E 01	-1.3842904E 01	0.	0.	0.090	0.0050	0.247
250	0 - 30	-7.8771110E-01	-1.4453869E 01	5.0066197E 01	-1.1574134E 02	1.2698621E 02	-5.2410541E 01	0.215	0.1416	0.993
	30 - 60	-5.2519155E-02	-2.4414937E 01	1.3313731E 02	-3.2080369E 02	3.5583520E 02	-1.5381467E 02	0.371	0.1150	0.851
	60 - 90	-6.6531354E-02	-3.0491963E 01	2.8895524E 02	-1.4836621E 03	3.3241898E 03	-2.7020325E 03	0.227	0.0269	0.482
	90 -180	-5.9932761E-01	-4.0606412E 01	2.0345147E 02	-4.7629328E 02	0.	0.	0.111	0.0059	0.250
300	0 - 30	-1.2155360E-01	-2.1731345E 01	7.8681130E 01	-1.4409672E 02	1.4343592E 02	-5.6490879E 01	0.246	0.1579	0.988
	30 - 60	-3.7193603E-01	-1.6553672E 01	6.3703451E 01	-1.1059728E 02	1.0029305E 02	-4.6061453E 01	0.321	0.1020	0.829
	60 - 90	-2.8208230E-01	-2.8063827E 01	2.5518559E 02	-1.2282931E 03	2.5585526E 03	-1.9154318E 03	0.212	0.0284	0.520
	90 -180	-5.4376391E-01	-7.9226521E 01	2.0098954E 03	-3.0054446E 04	2.0322205E 05	-4.9468843E 05	0.104	0.0053	0.184
350	0 - 30	4.9973676E-03	-2.5870804E 01	1.2477932E 02	-2.9986539E 02	3.3845728E 02	-1.3787044E 02	0.239	0.1526	0.993
	30 - 60	7.3580483E-02	-3.4102023E 01	2.1108432E 02	-5.8862568E 02	7.7569330E 02	-3.9378913E 02	0.341	0.1103	0.766
	60 - 90	7.0846651E-02	-3.2576236E 01	2.2428352E 02	-7.1769189E 02	7.5546995E 02	-4.3808124E 01	0.218	0.0233	0.413
	90 -180	-5.9619313E-01	-5.3074278E 01	4.9380922E 02	-1.9365708E 03	0.	0.	0.103	0.0047	0.185
400	0 - 30	-6.6414855E-01	-9.8006985E 00	2.6002760E 01	-5.7253648E 01	8.2484297E 01	-4.1018071E 01	0.234	0.1501	0.990
	30 - 60	-2.0020833E-01	-2.2868510E 01	1.2136427E 02	-2.7775533E 02	2.8624358E 02	-1.1444596E 02	0.330	0.0979	0.820
	60 - 90	1.4867976E-01	-4.2491637E 01	4.3383504E 02	-2.0681772E 03	4.2879112E 03	-3.2866879E 03	0.248	0.0299	0.448
	90 -180	-3.3305976E-01	-6.9980804E 01	8.1158859E 02	-4.3627996E 03	7.8309917E 03	0.	0.119	0.0064	0.215

TABLE 5.4.

NEUTRONS INCIDENT ON C

NEUTRONS EMITTED

EMIN = 0.871 (MEV)

from ORNL-4046, p 26

EO (MEV)	ANG. INT.	A0	A1	A2	A3	A4	A5	NO. EMIT.	ENERGY EMIT./EO	EMAX /EO
25	0 - 30	-7.6493350E-01	-8.6013533E 00	4.2105941E 01	-1.0521529E 02	1.3237319E 02	-6.3241627E 01	0.206	0.1032	0.960
	30 - 60	-6.8448551E-01	-1.2403641E 01	6.8768542E 01	-1.9225215E 02	2.3739658E 02	-1.0654224E 02	0.274	0.0956	0.923
	60 - 90	-2.7510834E 00	6.6206055E 00	-5.2716327E 01	1.1157715E 02	-8.6005285E 01	0.	0.078	0.0181	0.705
	90 -180	0.	0.	0.	0.	0.	0.	0.013		
50	0 - 30	-2.0778567E-01	-1.1704290E 01	3.9372058E 01	-6.8497888E 01	7.0718166E 01	-3.0879007E 01	0.291	0.1596	0.972
	30 - 60	-6.4984113E-01	-7.7406247E 00	3.0661108E 01	-6.3479368E 01	6.4041349E 01	-2.7396025E 01	0.401	0.1416	0.906
	60 - 90	-1.1523665E 00	-1.0863029E 01	5.8903286E 01	-2.4516166E 02	4.3394194E 02	-2.7706701E 02	0.141	0.0252	0.661
	90 -180	-2.4017256E 00	-8.3832544E 00	-1.7807788E 02	1.5209739E 03	-3.2495096E 03	0.	0.038	0.0040	0.292
100	0 - 30	-1.1774624E-01	-1.5545677E 01	5.4972131E 01	-9.8816444E 01	1.0278292E 02	-4.4001123E 01	0.334	0.2032	0.980
	30 - 60	-6.4101563E-01	-4.0426673E 00	-2.8640786E 00	5.4036796E 01	-9.7089226E 01	4.7576697E 01	0.531	0.1997	0.933
	60 - 90	-5.3330283E-01	-1.1318016E 01	1.7012274E 01	5.8204978E 01	-2.6157126E 02	2.2672234E 02	0.228	0.0360	0.599
	90 -180	-1.9028035E 00	-2.9879983E 00	-1.7882437E 02	1.0467939E 03	-1.7825228E 03	0.	0.076	0.0065	0.341
150	0 - 30	-2.0959782E-01	-2.2994879E 01	1.2912985E 02	-3.2612559E 02	3.7679781E 02	-1.5980101E 02	0.348	0.2237	0.984
	30 - 60	-2.3527726E-01	-1.1842771E 01	4.7225636E 01	-7.4792103E 01	4.8996539E 01	-1.3455162E 01	0.595	0.2202	0.905
	60 - 90	-1.8632898E-01	-1.8984977E 01	1.0699300E 02	-3.0976274E 02	3.6779867E 02	-1.5732480E 02	0.299	0.0480	0.551
	90 -180	-1.1363826E 00	-2.7559410E 01	9.4244428E 01	-1.5680726E 02	0.	0.	0.093	0.0069	0.346
200	0 - 30	-1.1750917E-01	-1.8730914E 01	5.3922731E 01	-7.5016534E 01	7.5080383E 01	-3.5821483E 01	0.360	0.2426	0.990
	30 - 60	1.3369825E-02	-1.8249426E 01	8.6052132E 01	-1.6805498E 02	1.5119174E 02	-5.6470636E 01	0.632	0.2378	0.927
	60 - 90	-2.9516557E-01	-1.7265287E 01	1.2322163E 02	-4.5872537E 02	7.3127470E 02	-4.5993271E 02	0.314	0.0482	0.514
	90 -180	-8.5156131E-01	-3.8428568E 01	6.8202530E 02	-9.9092146E 03	5.9031255E 04	-1.1731995E 05	0.113	0.0070	0.260
250	0 - 30	-4.3746096E-01	-1.5260643E 01	6.2977042E 01	-1.3634289E 02	1.5884999E 02	-7.0017192E 01	0.398	0.2740	0.994
	30 - 60	-3.6453561E-02	-1.8896747E 01	9.2007339E 01	-1.7994496E 02	1.6700939E 02	-5.8968556E 01	0.646	0.2464	0.877
	60 - 90	1.2702489E-02	-2.7445977E 01	2.2016220E 02	-8.3467653E 02	1.3190954E 03	-7.5253193E 02	0.313	0.0455	0.562
	90 -180	-4.7721499E-01	-2.9904421E 01	-2.1129479E 02	5.7995796E 03	-3.8098317E 04	7.5246299E 04	0.147	0.0065	0.287
300	0 - 30	-2.5286143E-01	-1.5761725E 01	4.6247803E 01	-8.0016946E 01	9.9215782E 01	-4.9810593E 01	0.393	0.2732	0.988
	30 - 60	-2.8370045E-01	-1.0464207E 01	4.1487364E 01	-5.6932179E 01	2.5939067E 01	-3.3443879E 00	0.694	0.2636	0.907
	60 - 90	9.6215317E-02	-2.6312302E 01	2.1745939E 02	-8.5171151E 02	1.3518755E 03	-7.6125124E 02	0.342	0.0459	0.523
	90 -180	-6.0772640E-01	-3.1096759E 01	8.5231426E 01	3.3234029E 01	-5.0693763E 02	0.	0.137	0.0079	0.285
350	0 - 30	-5.7709907E-02	-1.6087930E 01	3.5065401E 01	-3.2080775E 01	3.2145140E 01	-1.8840252E 01	0.426	0.2988	0.990
	30 - 60	-3.6367399E-01	-1.5652454E 01	8.7387666E 01	-1.8606756E 02	1.7589416E 02	-6.7149365E 01	0.679	0.2644	0.845
	60 - 90	-1.8106236E-01	-1.6460295E 01	1.0175429E 02	-3.0146182E 02	2.6376266E 02	0.	0.341	0.0498	0.551
	90 -180	-4.9459853E-01	-3.8331112E 01	1.6298981E 02	-3.3873454E 02	0.	0.	0.127	0.0062	0.241
400	0 - 30	-6.0341378E-01	-1.2985270E 00	-3.8113036E 01	1.1502897E 02	-9.9257529E 01	2.4351025E 01	0.461	0.3193	0.993
	30 - 60	2.2382567E-02	-1.8473116E 01	9.3587853E 01	-1.8968690E 02	1.7583970E 02	-6.8876105E 01	0.708	0.2590	0.858
	60 - 90	1.9678671E-02	-2.1993045E 01	2.0627431E 02	-9.4960274E 02	1.7888151E 03	-1.1952493E 03	0.385	0.0535	0.505
	90 -180	-1.6666759E-01	-7.3026296E 01	1.5760147E 03	-1.9318715E 04	9.7578561E 04	-1.6699234E 05	0.159	0.0095	0.275

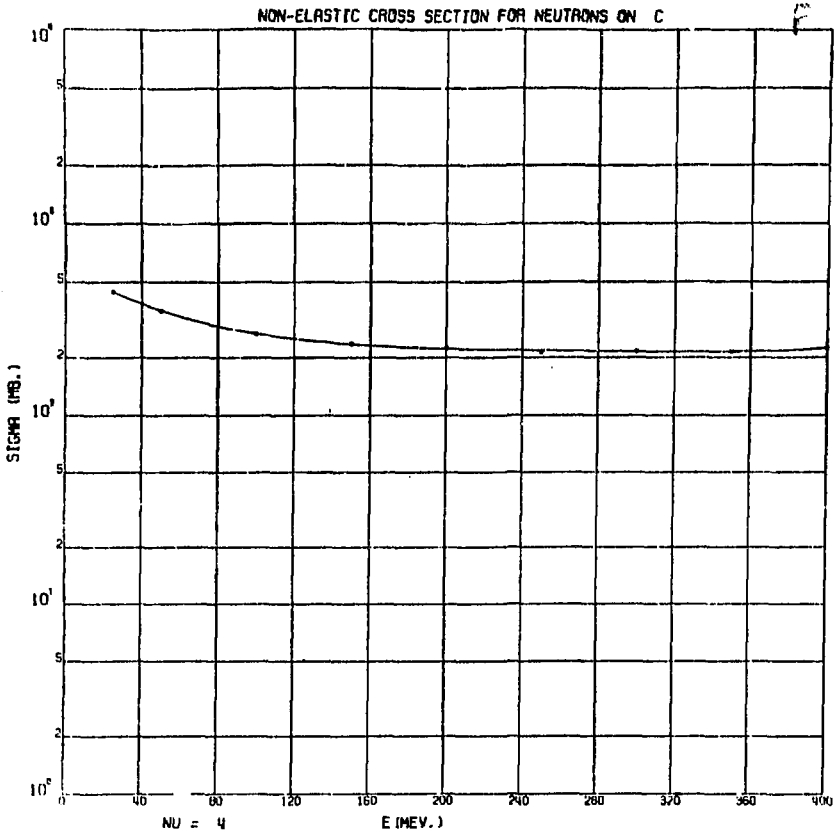

Fig. 30. Non-elastic cross section for neutrons on C with fitting formula

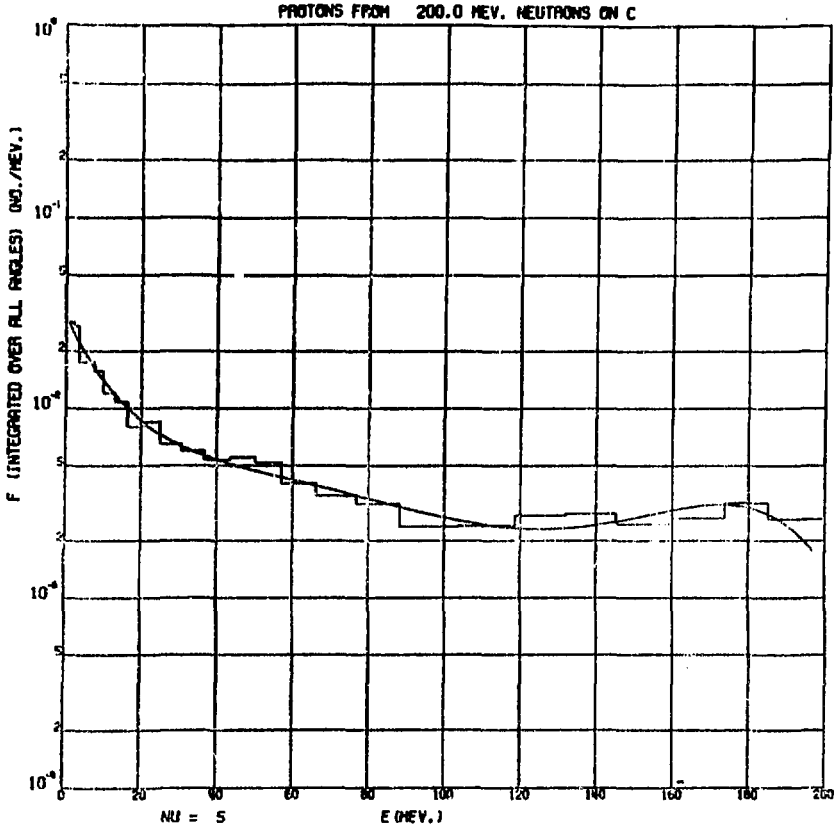

Fig. 31. An example of cascade protons emission spectra integrated over all angles from the n-C cascade reaction.

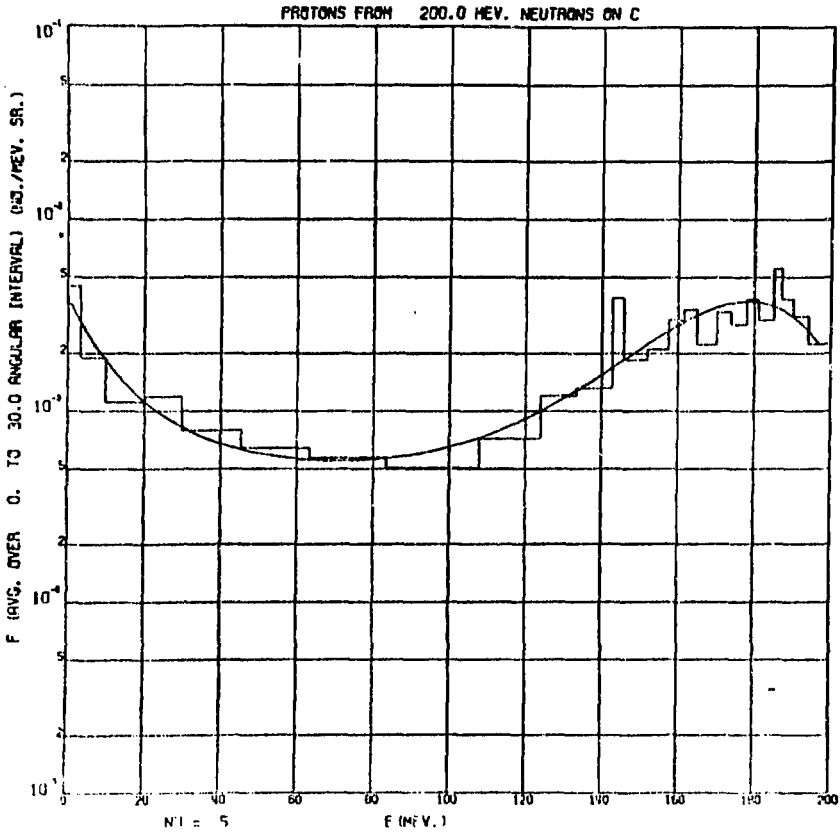

Fig. 32. An example of angular cascade protons emission spectra from n-C cascade reaction.

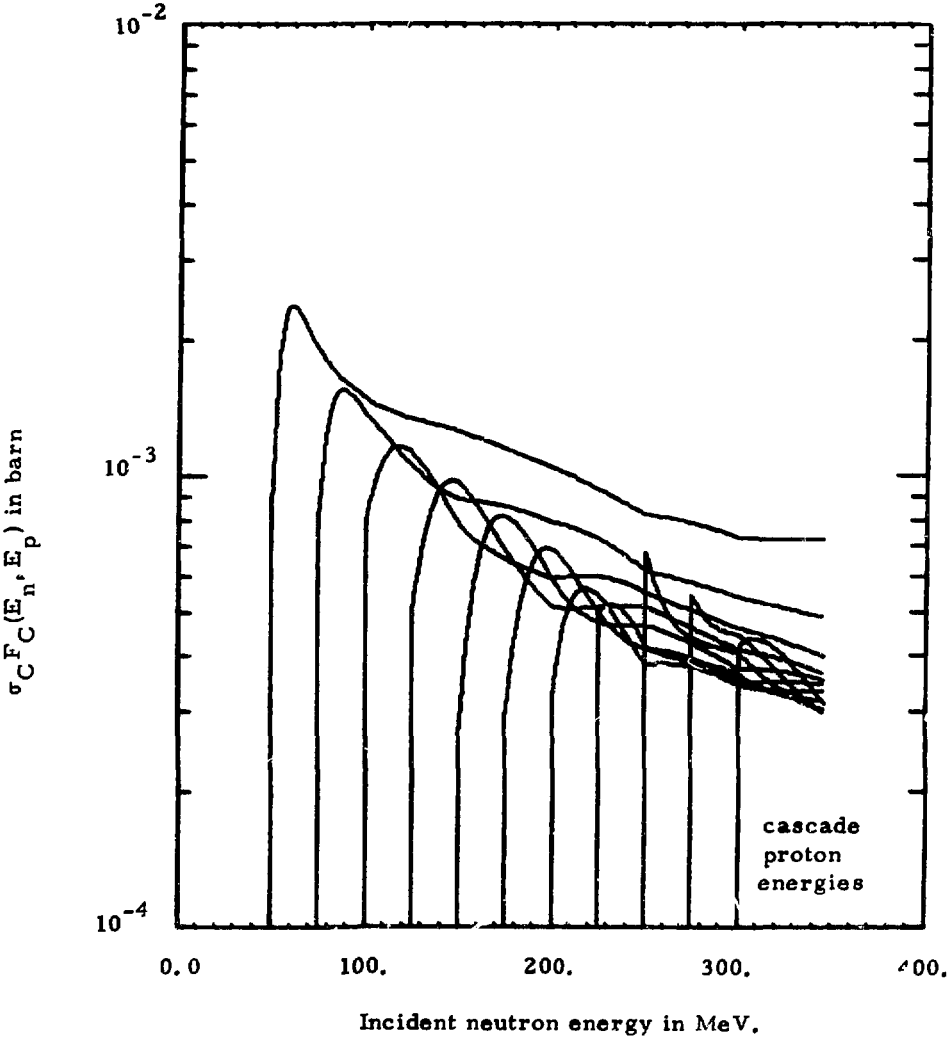

Fig. 33-a. Differential cross section of proton emitting cascade interaction with carbon nucleus as a function of incident neutron energy for a set of different cascade proton energies.

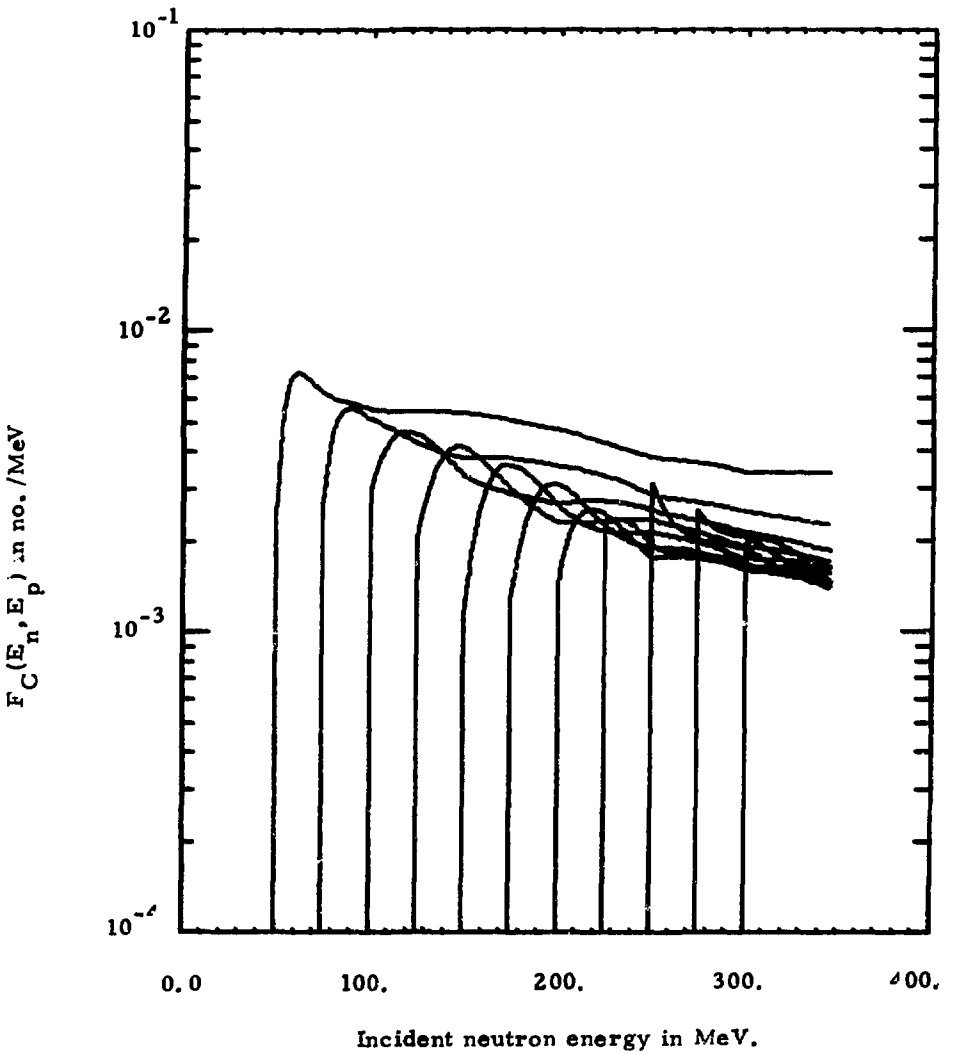

Fig. 33-b. Cascade proton emission energy spectra from the n-C cascade interaction as a function of incident neutron energy for a set of different cascade proton energies.

for the discrete energy points of incident neutron energy E_0. Table 5-2 gives the fitting coefficients (a_j's) for the emitted neutron and proton when a neutron of energy E_0 is incident on a carbon nucleus. The above distribution is in units of number per MeV per collision.

The energy-angle distributions of the cascade neutrons and protons emitted from a collision are more complicated, with the high energy particles being emitted predominantly at the smaller angles. The Monte Carlo results presented by Bertini give the emission spectra in the form of a histogram with equal energy intervals, averaged over specified angular intervals. These are the spectra that have been fitted. The assumed form of the energy distribution (number of emitted particles per MeV per steradian per collision), averaged over a specified angular interval, has the same form as equation (5-26). Tables 5-3 and 5-4 give the fitting coefficients (a_j's) for emission energy spectra of emitted protons and neutrons for each angular interval. Note that all of the formulas above are represented in laboratory energies in MeV.

In the simulation described in the next section, the angular distribution in each interval is assumed to be uniform in that interval, and for the incident neutron energies between the given energy points, the cross sections are obtained by linear interpolation from the two closest energy points for which fitting formulas are available.

Figures 31 and 32 show the fits with the data of the integrated and angular emission energy spectra when neutrons are incident on carbon.

3. Monte Carlo simulation procedure

The following is a somewhat simplified outline of the sampling procedure used in the kernel matrix element generation for specified incident neutron and detected proton energies (E'_n, E_p). In the samplings of a random variable, the random number generator RGEN has been used; this is a library routine of the Lawrence Berkeley Laboratory computing center. This routine generates random numbers that are distributed uniformly between 0 and 1. The coordinate system is the same as before (See Fig. 27).

Step 1: An initial position and incoming angle of the incident neutrons are chosen (with respect to front face of the spectrometer):

Choose x'_n and y'_n from the uniform distribution. Choose the incoming angle from a distribution approximating the forward peaking nature of the incoming neutron angular distribution. Suppose a power function of the cosine of the incident angle μ' is used: then the p. d. f. between $\mu=0$ and $\mu=1$ becomes $f(\mu) = (n+1)\mu^n$, and from $\int_0^{\mu'} (n+1)\mu^n d\mu = RGEN$, μ' is selected by

$$\mu' = (RGEN)^{\frac{1}{n+1}} \tag{5-27}$$

The azimuthal angle ϕ' is selected from the uniform distribution between 0 and 2π.

<u>Step 2:</u> Next, the particle is transported to the next collision site:

Choose R from $\Sigma_t(\underset{\sim}{r}' + R\underset{\sim}{\Omega}', E')\exp\left(-\int_0^R \Sigma_t(\underset{\sim}{r}' + R'\underset{\sim}{\Omega}', E')dR'\right)$.

Set $\underset{\sim}{r} = \underset{\sim}{r}' + R\underset{\sim}{\Omega}'$

If $\underset{\sim}{r}$ is outside the spectrometer volume, the particle has escaped and its history is terminated by scoring zero. However note that our spectrometer size is less than or comparable to the mean free path, and most of the injected neutrons are expected to escape without collision. So in actual sampling, a batch of neutrons are injected up to the maximum path length R_{max} within which neutrons can make collisions inside the spectrometer volume, and the equivalent total injection number is calculated from

$$\text{Equivalent Batch Number} = \text{Injection Number} \times \frac{1}{\int_0^{R_{max}} \Sigma_t e^{-\Sigma_t R} dR} .$$

Within R_{max}, R_{max} has beendivided 10 equal intervals and a collision number in each interval has been assigned out of the injection number by

$$\text{Injection Number} \times \frac{\int_{R_i}^{R_{i+1}} \Sigma_t e^{-\Sigma_t R} dR}{\int_0^{R_{max}} \Sigma_t e^{-\Sigma_t R} dR} \quad i = 0, 1, \ldots, 9.$$

In each interval R was selected by a rejection technique using

the p.d.f. $e^{-x} \approx 1 - x$ since x is small. The above sampling technique is a type of systematic sampling.

Step 3: At the new collision site the colliding nuclide among hydrogen and carbon is selected from

$$\text{Hydrogen: Carbon} = \frac{\Sigma_H(\underset{\sim}{r}, E')}{\Sigma_t(\underset{\sim}{r}, E')} : \frac{\Sigma_C(\underset{\sim}{r}, E')}{\Sigma_t(\underset{\sim}{r}, E')} .$$

Step 4: At this stage, in usual particle transport new energies and directions of the emitted proton and neutron are chosen as follows:[36]

Choose $E, \underset{\sim}{\Omega}$ from $\dfrac{\Sigma_S(E', \underset{\sim}{\Omega}' \to E, \underset{\sim}{\Omega} \mid \underset{\sim}{r})}{\Sigma_S(\underset{\sim}{r}, E')}$ as follows:

Choose μ from $f(\mu \mid E', \underset{\sim}{r})$.
Use the energy-angle relationship to determine $E = E(\mu, E')$.
Choose $\underset{\sim}{\Omega}$ so that $\underset{\sim}{\Omega} \cdot \underset{\sim}{\Omega}' = \mu$.
However, in our case we are interested in the proton single track event, as explained in the first section, whose energy is E_p when the incident neutron energy is E_n. This means that in our case the emitted particle energies have been predetermined and thus $f(E_p; E'_n)$ should be multiplied in the final scoring in order to account for this fact. Then the emission angle of the proton and the energy and scattering angle of the outcoming neutron are selected for the above E'_n and E_p.
Here the process is divided into two branches, namely, the case of a collision with H and a collision with C.

Case of a collision with H:

The recoil angle of the proton is calculated with given E'_n and E_p from equation (5-21).
The scattered neutron energy E_n is calculated from

$$E_n = E'_n - E_p ,$$

and its scattering angle is calculated from equation (5-22). Don't

forget that the recoil proton and scattered proton are emitted in the plane containing $\underset{\sim}{\Omega}'$ and $\underset{\sim}{\Omega}_p$.

Case of a collision with C:

In our energy range the number of emitted cascade protons (c-number) is smaller than one, and the number of emitted cascade neutron is larger than one, as shown in Table (5-2). So, if no proton is emitted, the history is terminated by scoring zero. However, if a proton is emitted, the emission angle interval is selected from Table (5-3), using the linear interpolation in the incident neutron energy, and the final emission angle is selected from the uniform distribution in that interval. The energies of the emitted neutrons are selected from the average energy emitted and their emission angles are selected from Table (5-4), using a similar linear interpolation as in the case of the emitted proton.

Step 5: Transformation of particle emission angle to the spectrometer reference frame.

The emission angles of proton and neutron as converted to the spectrometer frame to decide the new transport directions in the spectrometer volume. Suppose that the old and new directions of the particles are represented as

$$\underset{\sim}{\Omega}' = (\omega_1', \omega_2', \omega_3') \text{ and } \underset{\sim}{\Omega} = (\omega_1, \omega_2, \omega_3)$$

where
$$\omega_1 = \sin\theta \cos\phi$$
$$\omega_2 = \sin\theta \cos\phi$$
$$\omega_3 = \sin\theta \cos\phi \quad ,$$

and the particle emission angle is characterized by a polar angle θ_0 from $\underset{\sim}{\Omega}'$ and an azimuthal angle ϕ_0 of $\underset{\sim}{\Omega}$ from the plane containing ($\underset{\sim}{\Omega}'$, z). Then the expression for the new spherical coordinates in terms of the old is[33]

$$\cos\theta = \cos\theta' \cdot \cos\theta_0 + \sin\theta' \sin\theta_0 \cos\phi_0$$

$$\sin(\phi - \phi') = \frac{\sin\theta_0 \sin\phi_0}{\sin\theta}$$

$$\cos(\phi - \phi') = \frac{\cos\theta_0 - \cos\theta' \cos\theta}{\sin\theta' \sin\theta} \quad , \qquad (5\text{-}28)$$

and in Cartesian coordinates:[37] (5-29)

$$\omega_3 = \omega_3' \cos\theta_0 + \sin\theta_0 \cos\phi_0 \sqrt{1 - \omega_3'^{\,2}}$$

$$\omega_2 = \frac{1}{1-\omega_3'^{\,2}} \left[\omega_2' (\cos\theta_0 - \omega_3' \omega_3) + \sin\theta_0 \sin\phi_0 \, \omega_1' \sqrt{1-\omega_3'^{\,2}}\,.\right]$$

$$\omega_1 = \frac{1}{1-\omega_3'^{\,2}} \left[\omega_1' (\cos\theta_0 - \omega_3' \omega_3) - \sin\theta_0 \sin\phi_0 \, \omega_2' \sqrt{1-\omega_3'^{\,2}}\,.\right]$$

Step 6: Transport of emitted neutrons.

The emitted neutrons are transported as in Step 2, and if they make collisions inside the spectrometer volume the history is terminated by scoring zero. However, if they escape the spectrometer volume without collisions, Step 7 is processed.

Step 7: Transport of emitted proton

The emitted proton is transported by calculating the range corresponding to the energy E_p, using the range energy relationship and projecting it in the direction Ω to decide its stopping point. If it is within the spectrometer and the proton's path traverses more than two chambers to initiate sparking, then finally success is scored; otherwise fail is scored. In case the option of an extension leakage check of the proton track is used, this condition is also imposed before success is scored. A splitting technique has been used in Steps 6 and 7.

The above steps are repeated for each injected neutron until each batch is exhausted. In the process of the above sampling, the average fraction of the detected single proton track events (scored successes) against the equivalent injected batch neutron number is calculated after the exhaustion of each batch, which is the desired kernel matrix element for a given E'_n and E_p. Also, its variance and standard deviation from the estimate is calculated in the course of sampling, and the above procedure is continued until either the given error limit (standard deviation of the estimate) is satisfied or the given maximum injection number has been reached after the batch. In addition to the above estimates, many other quantities are estimated in the process, such as injected neutron collision probability and the proton detection probability, and so on.

4. Kernel Generation

The above sampling procedure has been programmed for calculations with the CDC 6600 and 7600 computers in order to generate the kernal matrix elements for each set of neutron and proton energies K(En', Ep). First, a convergence study was made for several sets of neutron and proton energies in order to see the speed of convergence of the estimated kernel matrix elements. Figure 34 shows the convergence rate of some kernel matrix elements as the neutron injection number increases. Usually 3 or 4% relative accuracy is obtained as the injection number reaches 30,000, and the sampling variances observed follow the central limit theorem rather faithfully. Table (5-5) shows the estimates of a kernel matrix element, its variance and relative error.

Next, functional forms approximating the highly peaked angular distribution of the incident neutrons have been studied. Since the incident angle covers only half of a unit sphere of solid angle, the cosine, μ, of the incident polar angle, θ, ranges from 1 to 0. One simple functional form, approximating the above type incident angular distribution in the above angular range of μ, is the power function of μ, i.e. $f(\mu) = (n+1)\mu^n$. There may be better functional forms approximating the above property. However, only power functions of μ have been studied. Table (5-6) shows the cumulative contribution of the above power function p.d.f. in each angular region of μ, for different values of power n. When n becomes 4, about 51% of the incident neutrons fall in the angular region of 30° from the normal direction. Figure 35 shows the p.d.f. $f(\mu) = (n+1)\mu^n$ on the μ scale.

With the above power functions, the kernel matrix elements have been generated for one incident neutron energy as a function of proton energy, with various n as parameter. This is shown in Fig. 35; it shows an abvious trend that as n increases the variation in the estimated kernel matrix element decreases, even though the variation with n is rather great when n is small. The above trend is typical, more or less, in every case.

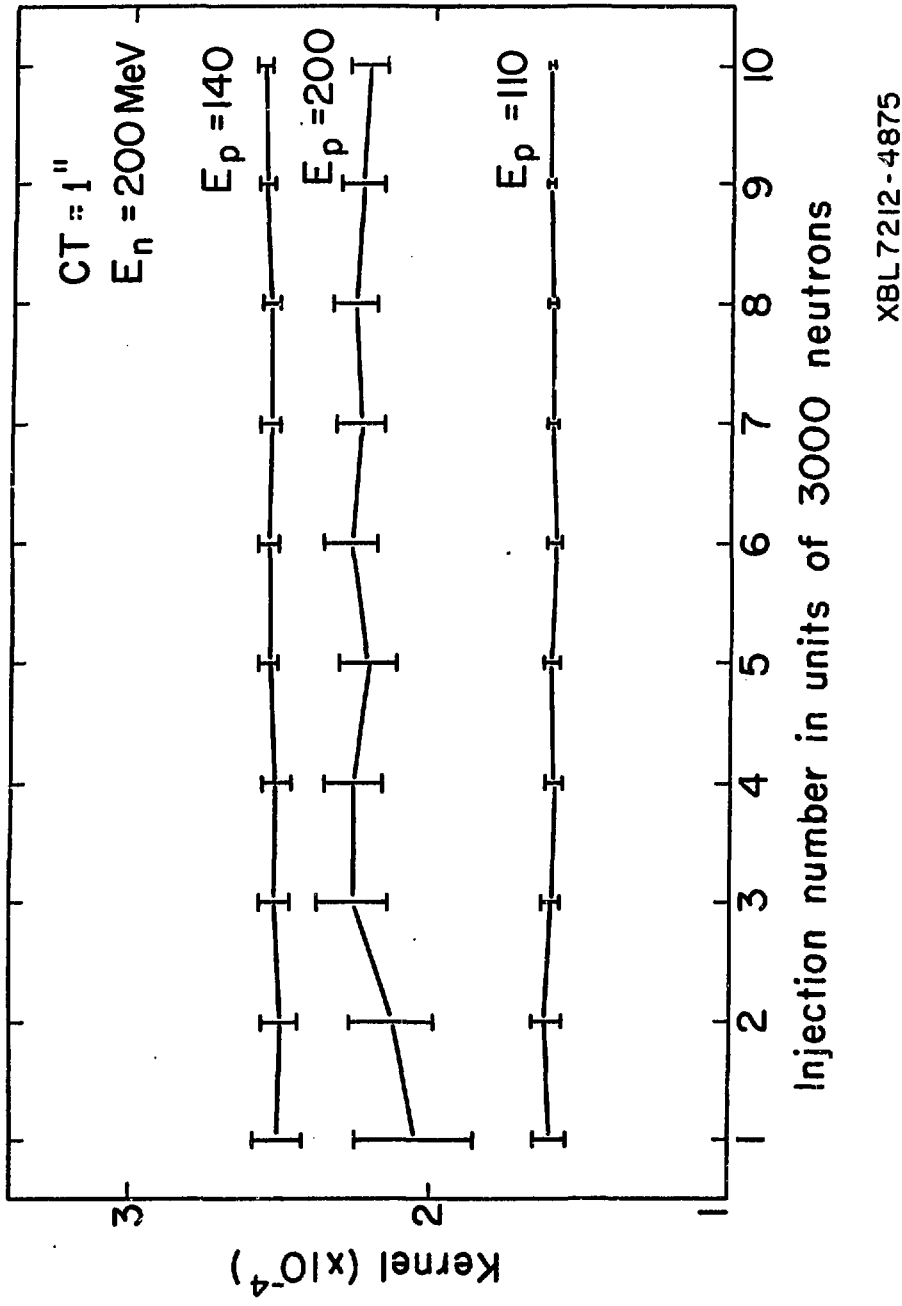

XBL 7212-4875

Fig. 34. Convergence of kernel estimate with an increase of the neutron injection number.

Table (5-5) Convergence of estimated kernel values with the increase of neutron injection numbers. (without extension option)

Injected Neutron Energy En=200 MeV, Converter thickness 1 inch, $f(\mu)=4\mu^3$

Proton Energy (MeV)		Neutron injection number in units of 3000 particles				
		2	4	6	8	10
110	$\hat{K}$	1.62	1.59	1.59	1.61	1.61
	$\hat{\sigma}$	3.79	2.64	2.16	1.88	1.68
	$\hat{\sigma}/\hat{K}$	2.33	1.66	1.36	1.17	1.05
140	$\hat{K}$	2.51	2.52	2.54	2.54	2.57
	$\hat{\sigma}$	5.71	4.04	3.32	2.89	2.60
	$\hat{\sigma}/\hat{K}$	2.28	1.60	1.31	1.13	1.01
170	$\hat{K}$	2.53	2.57	2.58	2.58	2.57
	$\hat{\sigma}$	7.03	5.02	4.11	3.57	3.18
	$\hat{\sigma}/\hat{K}$	2.78	1.95	1.59	1.38	1.24
200	$\hat{K}$	2.13	2.26	2.27	2.26	2.22
	$\hat{\sigma}$	14.9	11.0	8.97	7.76	6.85
	$\hat{\sigma}/\hat{K}$	6.99	4.84	3.95	3.43	3.10

$\hat{K}$; estimated kernel value in 10^{-4}

$\hat{\sigma}$; estimated sampling standard deviation in 10^{-6}

$\hat{\sigma}/\hat{K}$; relative error in 10^{-2}

Table 5.6. Cumulative distribution of $f(\mu) = (n+1)\mu^n$ in cones of angular region from $\theta = 0$ to $\theta = \cos^{-1}(x)$.

$$\int_x^1 (n+1)\mu^n \, d\mu = 1 - x^{n+1} \quad \text{and} \quad \int_0^1 f(\mu)d\mu = 1$$

$$\int_x^1 (n+1)\mu^n \, d\mu = 1 - x^{n+1}$$

n	$f(\mu)$	x 0.9659	0.8660	0.7071	0.5	0.2588
		θ 15°	30°	45°	60°	75°
0	1	0.034	0.134	0.293	0.5	0.741
1	2μ	0.067	0.25	0.5	0.75	0.933
2	$3\mu^2$	0.099	0.350	0.646	0.875	0.983
3	$4\mu^3$	0.130	0.437	0.750	0.9375	0.996
4	$5\mu^4$	0.159	0.513	0.823	0.969	0.999
5	$6\mu^5$	0.188	0.578	0.875	0.984	0.9997
6	$7\mu^6$	0.216	0.635	0.912	0.992	0.9999
7	$8\mu^7$	0.242	0.684	0.938	0.996	
8	$9\mu^8$	0.268	0.726	0.956	0.998	
9	$10\mu^9$	0.293	0.763	0.969	0.999	
10	$11\mu^{10}$	0.317	0.795	0.978	0.9995	

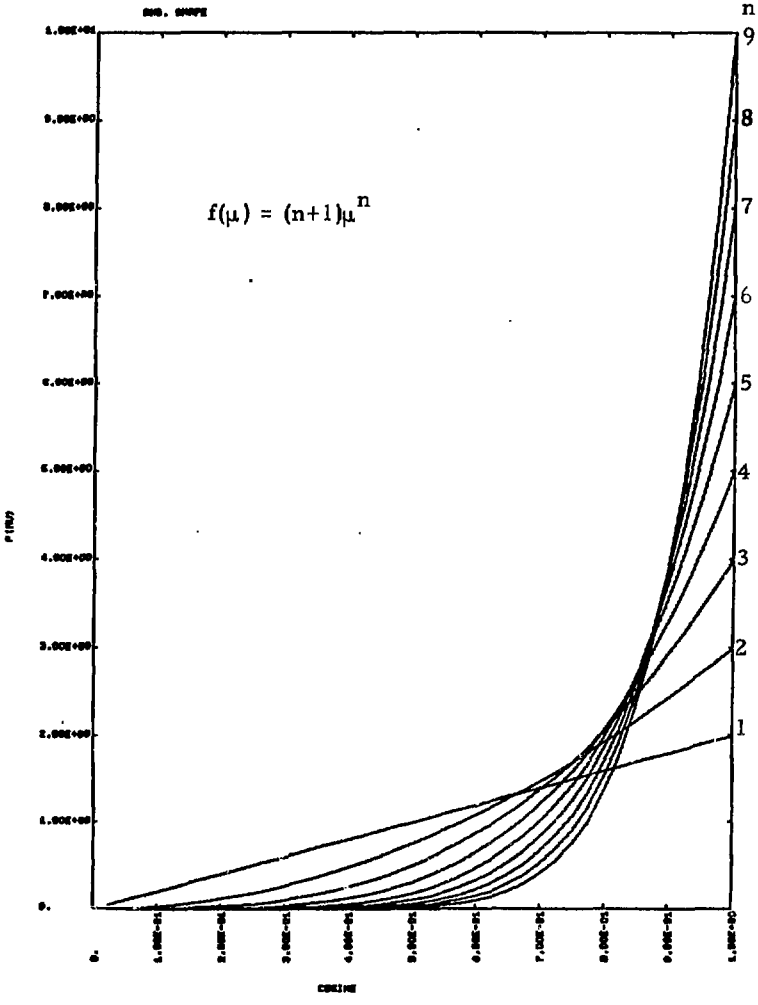

CHART No. 12-00

Fig. 35a. Shape of angular distribution function $f(\mu)$.

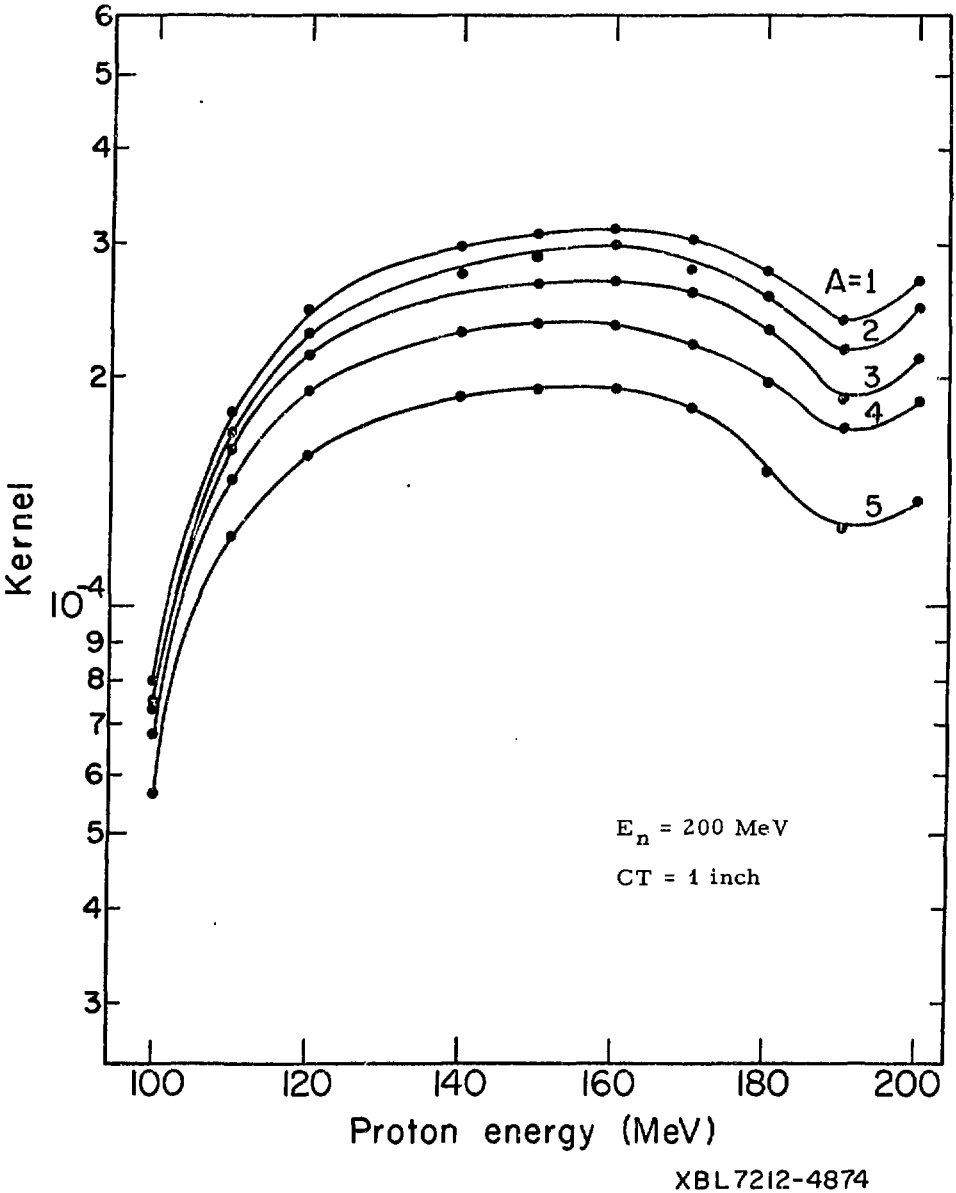

Fig. 35b. Variation of kernel estimate with change of n in $f(\mu) = (n+1)\mu^n$.

Table 5.7.-a

SUMMARY OF FINAL GENERAL REPORT

COLLISION EFFICIENCY -- CEFF(I).

EN	100.00	110.00	120.00	130.00	140.00	150.00	160.00	170.00	180.00	190.00	200.00	210.00
	220.00	230.00	240.00									
CEFF	2.82E-01	2.73E-01	2.53E-01	2.55E-01	2.42E-01	2.38E-01	2.37E-01	2.30E-01	2.26E-01	2.26E-01	2.21E-01	2.19E-01
	2.19E-01	2.19E-01	2.15E-01									

DETECTON EFFICIENCY -- DEFF

EN	100.00	110.00	120.00	130.00	140.00	150.00	160.00	170.00	180.00	190.00	200.00	210.00
	220.00	230.00	240.00									
EP												
100.0	2.15E-01	2.05E-01	1.79E-01	1.72E-01	1.61E-01	1.53E-01	1.35E-01	1.28E-01	1.24E-01	1.12E-01	1.12E-01	1.12E-01
.1	1.03E-01	9.83E-02										
110.0	0.	3.98E-01	3.94E-01	3.83E-01	3.51E-01	3.30E-01	3.06E-01	2.86E-01	2.79E-01	2.66E-01	2.62E-01	2.51E-01
.2	2.28E-01	2.27E-01										
120.0	0.	0.	4.59E-01	4.47E-01	4.46E-01	4.16E-01	3.89E-01	3.83E-01	3.73E-01	3.46E-01	3.37E-01	3.25E-01
.3	3.06E-01	3.07E-01										
130.0	0.	0.	0.	4.43E-01	4.47E-01	4.40E-01	4.06E-01	4.01E-01	3.85E-01	3.69E-01	3.64E-01	3.42E-01
.3	3.32E-01	3.26E-01										
140.0	0.	0.	0.	0.	4.23E-01	4.00E-01	3.95E-01	3.94E-01	3.76E-01	3.57E-01	3.44E-01	3.34E-01
.3	3.27E-01	3.24E-01										
150.0	0.	0.	0.	0.	0.	3.71E-01	3.53E-01	3.60E-01	3.53E-01	3.39E-01	3.39E-01	3.22E-01
.3	2.99E-01	3.01E-01										
160.0	0.	0.	0.	0.	0.	0.	3.18E-01	3.16E-01	3.10E-01	3.05E-01	2.95E-01	2.97E-01
.3	2.79E-01	2.69E-01										
170.0	0.	0.	0.	0.	0.	0.	0.	2.78E-01	2.75E-01	2.65E-01	2.55E-01	2.55E-01
.2	2.39E-01	2.30E-01										
180.0	0.	0.	0.	0.	0.	0.	0.	0.	2.25E-01	2.22E-01	2.23E-01	2.25E-01
.2	2.08E-01	2.00E-01										
190.0	0.	0.	0.	0.	0.	0.	0.	0.	0.	1.81E-01	1.81E-01	1.80E-01
.2	1.73E-01	1.72E-01										
200.0	0.	0.	0.	0.	0.	0.	0.	0.	0.	0.	1.45E-01	1.41E-01
.1	1.39E-01	1.39E-01										
210.0	0.	0.	0.	0.	0.	0.	0.	0.	0.	0.	0.	1.11E-01
.1	1.04E-01	1.01E-01										
220.0	0.	0.	0.	0.	0.	0.	0.	0.	0.	0.	0.	0.
.1	7.25E-02	7.45E-02										
230.0	0.	0.	0.	0.	0.	0.	0.	0.	0.	0.	0.	0.
0.0	3.89E-02	4.03E-02										
240.0	0.	0.	0.	0.	0.	0.	0.	0.	0.	0.	0.	0.
0.0	0.	1.18E-02										

Table 5.7.-b

OVERALL EFF. -- G KERNEL

EN / EP	100.00 / 220.00	110.00 / 230.00	120.00 / 240.00	130.00	140.00	150.00	160.00	170.00	180.00	190.00	200.00	210.00
100.0	6.07E-02	5.55E-02	4.71E-02	4.37E-02	3.96E-02	3.64E-02	3.20E-02	2.93E-02	2.80E-02	2.53E-02	2.47E-02	2.46E-02
.0	2.25E-02	2.12E-02										
110.0	0.	1.09E-01	1.03E-01	9.75E-02	8.49E-02	7.87E-02	7.25E-02	6.56E-02	6.32E-02	6.01E-02	5.73E-02	5.50E-02
.1	4.99E-02	4.88E-02										
120.0	0.	0.	1.20E-01	1.14E-01	1.07E-01	9.92E-02	9.21E-02	8.80E-02	8.45E-02	7.83E-02	7.44E-02	7.13E-02
.1	6.70E-02	6.62E-02										
130.0	0.	0.	0.	1.13E-01	1.08E-01	1.05E-01	9.61E-02	9.20E-02	8.72E-02	8.36E-02	8.04E-02	7.49E-02
.1	7.25E-02	7.02E-02										
140.0	0.	0.	0.	0.	1.02E-01	9.53E-02	9.35E-02	9.04E-02	8.50E-02	8.06E-02	7.60E-02	7.32E-02
.1	7.14E-02	6.97E-02										
150.0	0.	0.	0.	0.	0.	8.85E-02	8.37E-02	8.26E-02	7.99E-02	7.64E-02	7.47E-02	7.06E-02
.1	6.55E-02	6.47E-02										
160.0	0.	0.	0.	0.	0.	0.	7.53E-02	7.26E-02	7.02E-02	6.89E-02	6.51E-02	6.51E-02
.1	6.10E-02	5.78E-02										
170.0	0.	0.	0.	0.	0.	0.	0.	6.38E-02	6.23E-02	6.02E-02	5.65E-02	5.62E-02
.1	5.23E-02	4.95E-02										
180.0	0.	0.	0.	0.	0.	0.	0.	0.	5.10E-02	5.03E-02	5.04E-02	4.93E-02
.0	4.56E-02	4.30E-02										
190.0	0.	0.	0.	0.	0.	0.	0.	0.	0.	4.09E-02	4.01E-02	3.96E-02
.0	3.79E-02	3.69E-02										
200.0	0.	0.	0.	0.	0.	0.	0.	0.	0.	0.	3.26E-02	3.10E-02
.0	3.05E-02	3.00E-02										
210.0	0.	0.	0.	0.	0.	0.	0.	0.	0.	0.	0.	2.64E-02
.0	2.28E-02	2.18E-02										
220.0	0.	0.	0.	0.	0.	0.	0.	0.	0.	0.	0.	0.
.0	1.59E-02	1.61E-02										
230.0	0.	0.	0.	0.	0.	0.	0.	0.	0.	0.	0.	0.
0.0	9.51E-03	8.67E-03										
240.0	0.	0.	0.	0.	0.	0.	0.	0.	0.	0.	0.	0.
0.0	0.	2.55E-03										

Table 5.7.-c

KERNEL MATRIX --AKENEL

EM / EP	100.00 / 220.00	110.00 / 230.00	120.00 / 240.00	130.00	140.00	150.00	160.00	170.00	180.00	190.00	200.00	210.00
100.0	6.78E-04	4.32E-04	2.84E-04	2.43E-04	1.84E-04	1.41E-04	1.14E-04	9.45E-05	8.52E-05	7.39E-05	6.86E-05	6.39E-05
.0	5.68E-05	5.24E-05										
110.0	0.	1.06E-03	6.96E-04	5.05E-04	4.67E-04	3.41E-04	2.77E-04	2.10E-04	1.89E-04	1.70E-04	1.54E-04	1.34E-04
.0	1.19E-04	1.16E-04										
120.0	0.	0.	1.04E-03	7.45E-04	6.55E-04	4.93E-04	3.95E-04	2.92E-04	2.58E-04	2.24E-04	1.96E-04	1.70E-04
.0	1.53E-04	1.52E-04										
130.0	0.	0.	0.	1.03E-03	6.76E-04	5.68E-04	4.50E-04	3.30E-04	2.80E-04	2.49E-04	2.20E-04	1.81E-04
.0	1.62E-04	1.57E-04										
140.0	0.	0.	0.	0.	6.90E-04	5.21E-04	4.83E-04	3.55E-04	2.96E-04	2.61E-04	2.23E-04	1.84E-04
.0	1.59E-04	1.54E-04										
150.0	0.	0.	0.	0.	0.	5.96E-04	4.33E-04	3.52E-04	3.05E-04	2.71E-04	2.44E-04	1.91E-04
.0	1.48E-04	1.43E-04										
160.0	0.	0.	0.	0.	0.	0.	5.18E-04	3.40E-04	2.89E-04	2.70E-04	2.36E-04	1.95E-04
.0	1.43E-04	1.28E-04										
170.0	0.	0.	0.	0.	0.	0.	0.	5.45E-04	2.81E-04	2.54E-04	2.27E-04	1.89E-04
.0	1.30E-04	1.13E-04										
180.0	0.	0.	0.	0.	0.	0.	0.	0.	4.08E-04	2.26E-04	2.11E-04	1.82E-04
.0	1.20E-04	1.00E-04										
190.0	0.	0.	0.	0.	0.	0.	0.	0.	0.	2.90E-04	1.76E-04	1.55E-04
.0	1.08E-04	9.09E-05										
200.0	0.	0.	0.	0.	0.	0.	0.	0.	0.	0.	2.24E-04	1.32E-04
.0	9.75E-05	8.21E-05										
210.0	0.	0.	0.	0.	0.	0.	0.	0.	0.	0.	0.	1.69E-04
.0	8.11E-05	6.60E-05										
220.0	0.	0.	0.	0.	0.	0.	0.	0.	0.	0.	0.	0.
.0	6.99E-05	5.44E-05										
230.0	0.	0.	0.	0.	0.	0.	0.	0.	0.	0.	0.	0.
0.0	6.18E-05	3.68E-05										
240.0	0.	0.	0.	0.	0.	0.	0.	0.	0.	0.	0.	0.
0.0	0.	1.77E-05										

Table 5.7.-d

SAMPLING STANDARD DEVIATIONS -- STCK

IN / IP	100.00 / 220.00	110.00 / 230.00	120.00 / 240.00	130.00	140.00	150.00	160.00	170.00	180.00	190.00	200.00	210.00
10.0	1.87E-05	1.22E-05	7.15E-06	5.99E-06	4.55E-06	3.49E-06	2.85E-06	2.45E-06	2.25E-06	2.00E-06	1.85E-05	1.75E-06
.0	1.66E-05	1.51E-06										
20.0	0.	3.12E-05	1.46E-05	1.11E-05	8.62E-06	6.19E-06	5.05E-06	3.84E-06	3.44E-06	3.10E-06	2.81E-05	2.49E-06
.0	2.25E-05	2.29E-06										
30.0	0.	0.	2.81E-05	1.50E-05	1.17E-05	8.34E-06	6.61E-06	4.72E-06	4.16E-06	3.65E-06	3.23E-06	2.77E-05
.0	2.53E-06	2.49E-06										
40.0	0.	0.	0.	3.00E-05	1.46E-05	1.00E-05	7.75E-06	5.45E-06	4.61E-06	4.12E-06	3.66E-05	2.95E-06
.0	2.61E-05	2.54E-06										
50.0	0.	0.	0.	0.	2.12E-05	1.15E-05	8.96E-06	6.03E-06	5.04E-06	4.49E-06	3.89E-05	3.12E-06
.0	2.61E-05	2.51E-06										
60.0	0.	0.	0.	0.	0.	1.46E-05	1.01E-05	6.50E-06	5.46E-06	4.85E-06	4.42E-05	3.33E-06
.0	2.50E-05	2.38E-06										
70.0	0.	0.	0.	0.	0.	0.	1.89E-05	8.25E-06	5.78E-06	5.21E-06	4.64E-05	3.65E-06
.0	2.57E-05	2.29E-06										
80.0	0.	0.	0.	0.	0.	0.	0.	1.57E-05	7.19E-06	5.50E-06	4.86E-05	3.82E-06
.0	2.54E-05	2.17E-06										
90.0	0.	0.	0.	0.	0.	0.	0.	0.	1.25E-05	6.12E-06	4.79E-05	3.89E-06
.0	2.46E-06	2.03E-06										
100.0	0.	0.	0.	0.	0.	0.	0.	0.	0.	1.30E-05	4.99E-05	3.74E-06
.0	2.30E-06	1.91E-06										
110.0	0.	0.	0.	0.	0.	0.	0.	0.	0.	0.	1.05E-05	4.13E-06
.0	2.41E-05	1.97E-06										
120.0	0.	0.	0.	0.	0.	0.	0.	0.	0.	0.	0.	6.01E-06
.0	2.35E-05	1.79E-06										
130.0	0.	0.	0.	0.	0.	0.	0.	0.	0.	0.	0.	0.
.0	1.97E-05	1.29E-06										
140.0	0.	0.	0.	0.	0.	0.	0.	0.	0.	0.	0.	0.
0.0	3.14E-05	1.69E-06										
150.0	0.	0.	0.	0.	0.	0.	0.	0.	0.	0.	0.	0.
0.0	0.	2.23E-06										

Table 5.7.-e

ELATIVE ERRORS -- RELERR

N	100.00	110.00	120.00	130.00	140.00	150.00	160.00	170.00	180.00	190.00	200.00	210.00
	220.00	230.00	240.00									
P												
0.0	2.76E-02	2.82E-02	2.52E-02	2.46E-02	2.45E-02	2.47E-02	2.49E-02	2.59E-02	2.64E-02	2.71E-02	2.71E-02	2.74E-02
.0	2.92E-02	2.88E-02										
0.0	0.	2.94E-02	2.09E-02	1.86E-02	1.85E-02	1.82E-02	1.83E-02	1.83E-02	1.82E-02	1.83E-02	1.82E-02	1.85E-02
.0	1.96E-02	1.97E-02										
0.0	0.	0.	2.69E-02	2.02E-02	1.78E-02	1.69E-02	1.67E-02	1.62E-02	1.61E-02	1.63E-02	1.64E-02	1.62E-02
.0	1.65E-02	1.64E-02										
0.0	0.	0.	0.	2.92E-02	2.13E-02	1.77E-02	1.72E-02	1.65E-02	1.64E-02	1.66E-02	1.66E-02	1.63E-02
.0	1.60E-02	1.61E-02										
0.0	0.	0.	0.	0.	3.08E-02	2.21E-02	1.86E-02	1.70E-02	1.70E-02	1.72E-02	1.74E-02	1.69E-02
.0	1.63E-02	1.63E-02										
0.0	0.	0.	0.	0.	0.	2.45E-02	2.34E-02	1.84E-02	1.79E-02	1.79E-02	1.81E-02	1.75E-02
.0	1.69E-02	1.67E-02										
0.0	0.	0.	0.	0.	0.	0.	3.65E-02	2.43E-02	2.00E-02	1.92E-02	1.95E-02	1.88E-02
.0	1.79E-02	1.78E-02										
0.0	0.	0.	0.	0.	0.	0.	0.	2.88E-02	2.56E-02	2.16E-02	2.14E-02	2.03E-02
.0	1.96E-02	1.93E-02										
0.0	0.	0.	0.	0.	0.	0.	0.	0.	3.06E-02	2.71E-02	2.27E-02	2.14E-02
.0	2.04E-02	2.02E-02										
0.0	0.	0.	0.	0.	0.	0.	0.	0.	0.	4.47E-02	2.83E-02	2.41E-02
.0	2.13E-02	2.10E-02										
0.0	0.	0.	0.	0.	0.	0.	0.	0.	0.	0.	4.67E-02	3.13E-02
.0	2.47E-02	2.39E-02										
0.0	0.	0.	0.	0.	0.	0.	0.	0.	0.	0.	0.	3.55E-02
.0	2.89E-02	2.71E-02										
0.0	0.	0.	0.	0.	0.	0.	0.	0.	0.	0.	0.	0.
.1	2.81E-02	2.36E-02										
0.0	0.	0.	0.	0.	0.	0.	0.	0.	0.	0.	0.	0.
0.0	5.88E-02	4.58E-02										
0.0	0.	0.	0.	0.	0.	0.	0.	0.	0.	0.	0.	0.
0.0	0.	1.26E-01										

Table (5-7) shows the sample kernel matrix generated with the incident angular distribution $f(\mu) = 4\mu^3$ for the converter thickness of 1 inch. One can note from the table that for a fixed proton energy the variation with the incident neutron energy is rather weak, while the variation of the matrix element with the proton energy for a fixed neutron energy is appreciable. The average variation with proton energy tends to peak in the middle and drops out quickly as the proton energy decreases or increases from the peaking middle. Dropping in the lower proton energy region is mainly due to the requirement of minimum triple chambers sparking with short proton range, and that in the higher proton energy region is generally attributed to the large escape probability of proton tracks, due to the large range of higher energy protons.

In the generation of the above sample kernel matrix, a constant angular shape has been used throughout its neutron energy range. However, in an actual situation, the incident neutron angular shape does vary with the incoming neutron energy so that it is more sharply peaked in the higher energy region, and as the neutron energy decreases, its sharpness decreases gradually. Therefore, in actual kernel generation for a real situation, it is recommended that the kernel matrix be generated by incorporating the above type energy dependency of the incident neutron angular distribution. Sometimes this energy dependency of the incident angular distribution is available from the literature.[1,38]

5. Solution of the Neutron Spectrum from the Measured Proton Spectrum

Once the proton energy spectrum is available from the measurement with the spectrometer set-up, and the kernel matrix is ready, the unknown neutron energy spectrum is obtained by solving equation (2-47), which is the first order Fredholm integral equation. If we rearrange the equation slightly, the integral equation to be solved is represented as

$$N(E') = \int_{E_{min}}^{E_{max}} K(E', E)\,\phi(E)\,dE \qquad (5\text{-}30)$$

Theoretically, there are several solution techniques which are known to give a formal solution to the above integral equation.[39,40,41] However, the formal solution methods are not applicable generally in the case where neither the measured spectrum N(E') nor the kernal K(E',E) is known analytically, but rather as a set of discrete points. The solution of such a system may be obtained only through numerical techniques. In most of these techniques, the integral equation is usually approximated by a system of linear equations, and the methods known for the solution of such a system are applied. One should also note that sometimes the formal solution to the above integral equation is not unique.

In any practical situations where the above type integral equation arises in connection with the experiments, the measured values from the experiment always involve random errors, and this fact poses a new problem. The uncertainties of the used kernel also add to the difficulty of the problem. Therefore, in the practical numerical solution technique, an approximate solution is pursued which gives the physically acceptable answer that fits well the measured values. Sometimes it is important, in the solution technique, to weigh the prior knowledge and the information contained in the measured values. Therefore, the basic criteria in the usual practical solution techniques is to find an appropriate solution which matches the measured spectrum faithfully and gives the physically acceptable shape. These are the prime requirements of the solution. Numerous practical solution techniques in the above situation have been reviewed recently by Jorma Routti in his Ph. D. thesis.[8] He also developed two general least squares methods to solve the above integral equation numerically, called respectively a generalized least-squares method with matrix inversion and a generalized least-squares method with non-negative solution. In the first method the flux is approximated by a piecewise linear continuous function, and the deviation between the measured spectrum and calculated spectrum at each energy point is minimized essentially by inverting the normal equation which is obtained from the usual minimization requirement at each flux point, namely, setting the first derivatives equal to zero. It has the option of introducing prior

information of smoothness of the solution spectrum and the closeness to a given physically acceptable solution shape in a flexible way. But this method does not guarantee the nonnegativity of the solution spectrum which can not be possible physically. On the other hand the second method has the assurance of the nonnegativity of the solution, in addition to the above options, by introducing the variable X_i in the least squares process such that $\phi_i = X_i^2$ at each energy mesh point. However the least squares process is different from the above in the sense that the least squares sum of the difference between the measured and calculated responses is directly minimized with respect to X_i, using a minimization technique called the iterative gradient method with variable metric.[42,43] This method will be used in our case. The above two methods have been programmed into a computer code by Jorma Routti and are called respectively called KIEPPI and LOUHI.

The remainder of this section will explain the mathematical and numerical details of the above least squares solution method (LOUHI), giving more emphasis to the actual calculational scheme used in the program, rather than generalizing.

First, the integral equation can be rewritten to include a term $\epsilon(E')$, representing the uncertainties and error of the measured values:

$$\int_{E_{min}}^{E_{max}} K(E', E)\phi(E)dE = A(E') + \epsilon(E'), \tag{5-31}$$

where $A(E')$ represents the measured proton spectrum and is changed from $N(E')$ for notational convenience. The above equation is put into a quadrature form by approximating the flux with a piecewise linear continuous function, defined between the energy values E_1 and E_n, which extend from the lowest threshold to the cut-off energy of the solution. Then the solution in the interval E_i to E_{i+1} is given by

$$\phi(E) = \phi_{i+1} \cdot \left(\frac{E - E_i}{E_{i+1} - E_i}\right) + \phi_i \cdot \left(\frac{E_{i+1} - E}{E_{i+1} - E_i}\right) . \tag{5-32}$$

Suppose E' is divided in the same way as E and represented as E_{ji}; then at each point E_j the substitution of equation (5-32) into the integral equation yields

$$K_{ji} = \int_{E_{i-1}}^{E_i} \left(\frac{E - E_{i-1}}{E_i - E_{i-1}} \right) K(E_j, E)dE + \int_{E_i}^{E_{i+1}} \left(\frac{E_{i+1} - E}{E_{i+1} - E_i} \right) K(E_j, E)dE, \tag{5-33}$$

and the resulting quadrature formula have the matrix form

$$\underset{\sim}{K}\ \underset{\sim}{\phi} = \underset{\sim}{A} + \underset{\sim}{\epsilon}\ , \tag{5-34}$$

where $\underset{\sim}{A}$, $\underset{\sim}{\epsilon}$ and $\underset{\sim}{\phi}$ are column vectors with components A_j, ϵ_j $(j = 1, \ldots . m)$ and ϕ_i $(i = 1, \ldots . n)$, respectively, and K is the kernel matrix of dimensions nxm.

Next, the basic considerations in making the square sum for minimization are the following requirements:

i)	matching the measured values	Q_0
ii)	closeness to a given physical shape function P	Q_1
iii)	smoothness requirement	Q_2
iv)	nonnegativity requirement	$\phi_i = X_i^2$.

Then the solution of the integral equation is obtained by minimizing the following quadratic form with respect to the Xi's

$$Q = Q_0 + \gamma (\overline{W}_1 Q_1 + \overline{W}_2 Q_2), \tag{5-35}$$

where $\overline{W}_1$ and $\overline{W}_2$ are relative weights of Q_1 and Q_2 terms and γ specifies the overall importance of the Q_1, Q_2 term representing a priori conditions. Here

$$\begin{aligned} Q_0 &= \sum_{j=1}^{m} \omega_j^0 \epsilon_j^2 = \sum_{j=1}^{m} \omega_j^0 \left(A_j^m - A_j^c \right)^2 \\ &= \sum_{j=1}^{m} \omega_j^0 \left(A_j^m - \sum_{i=1}^{n} K_{ji} X_i^2 \right)^2 \end{aligned} \tag{5-36}$$

where

A_j^m = measured value

A_j^c = computed value from X_i

W_j^0 = weighting function.

Q_1 and Q_2 terms are expressed in three different scales. They are on a linear scale

$$Q_1 = \sum_{i=1}^{n} \omega_i^1 (X_i^2 - P_i)^2$$

$$Q_2 = \sum_{i=2}^{n-1} \omega_i^2 (X_{i-1}^2 - 2X_i^2 + X_{i+1}^2)^2, \tag{5-37}$$

and on a relative scale

$$Q_1 = \sum_{i=1}^{n} \omega_i^1 \left(\frac{X_i^2 - P_i}{X_i^2}\right)^2$$

$$Q_2 = \sum_{i=2}^{n-1} \omega_i^2 \left(\frac{X_{i-1}^2 - 2X_i^2 + X_{i+1}^2}{X_i^2}\right)^2, \tag{5-38}$$

and on a logarithmic scale

$$Q_1 = \sum_{i=1}^{n} \omega_i^1 \left(\log X_i^2 - \log P_i\right)^2$$

$$Q_2 = \sum_{i=2}^{n-1} \omega_i^2 \left(\log X_{i-1}^2 - 2 \log X_i^2 + \log X_{i+1}^2\right)^2. \tag{5-39}$$

In the process of minimization of the function Q with respect to the Xi's, using an iterative gradient method, the partial derivatives of the function Q with respect to Xi's are required in projecting a new minimizing direction. Their expressions are rather lengthy and can be obtained from the expression of Q. Here only the form in the linear scale will be given. Noting that the derivative of Q is the sum of the partial derivatives of its components, we get the following expression for each term for $i = \ell$:

$$G_\ell^0 = \frac{\partial Q_0}{\partial X_\ell} = \sum_{j=1}^{m} 4\omega_j^0 K_{j\ell} X_\ell \left(A_j^m - \sum_{i=1}^{n} K_{ji} X_i^2\right)^2, \tag{5-40}$$

$$G_\ell^1 = \frac{\partial Q_1}{\partial X_\ell} = 4\omega_\ell^1 X_\ell (X_\ell^2 - P_\ell), \tag{5-41}$$

and

$$G_\ell^2 = \left(\frac{\partial Q_2}{\partial X_\ell}\right)_{(\ell+1)\text{ term}} + \left(\frac{\partial Q_2}{\partial X_\ell}\right)_{\ell\text{ term}} + \left(\frac{\partial Q_2}{\partial X_\ell}\right)_{(\ell-1)\text{ term}}, \tag{5-42}$$

where

$$\left(\frac{\partial Q_2}{\partial X_\ell}\right)_{(\ell+1)\text{ term}} = 4\omega_{\ell+1}^2 X_\ell (X_\ell^2 - 2X_{\ell+1} + X_{\ell+2}^2)$$

valid from $\ell = 1$ to $n-2$, otherwise zero,

$$\left(\frac{\partial Q_2}{\partial X_\ell}\right)_{\ell\text{ term}} = -8\omega_\ell^2 X_\ell (X_{\ell-1}^2 - 2X_\ell + X_{\ell+1}^2)$$

valid from $\ell = 2$ to $n-1$, otherwise zero,

$$\left(\frac{\partial Q_2}{\partial X_\ell}\right)_{(\ell-1)\text{ term}} = 4\omega_{\ell-1}^2 X_\ell (X_{\ell-2}^2 - 2X_{\ell-1} + X_\ell^2)$$

valid from $\ell = 3$ to N, otherwise zero,

$$\frac{\partial Q}{\partial X_\ell} = G_\ell^0 + \gamma(\overline{W}_1 G_\ell^1 + \overline{W}_2 G_\ell^2). \tag{5-43}$$

The set of Xi's which gives the minimum value of the function Q is obtained when the minimization process is finished, and finally $\phi_i = X_i^2$ (i = 1, ... n) from those Xi's is the desired solution. In the calculation, an iterative gradient method algorithm VARMIT with variable metric, developed by Davidon[42] and coded by Beals,[43] is used. The minimization is terminated when all the components of the next step are less than 10^{-8} if four succeeding values are the same, or 100 iterations have been completed.

The above program has been subjected to extensive tests by Jorma Routti and his broad experience with the method is described in detail in ref. 8. Figure 36 shows one example of the test of the above method with the kernel matrix generated in the previous section.

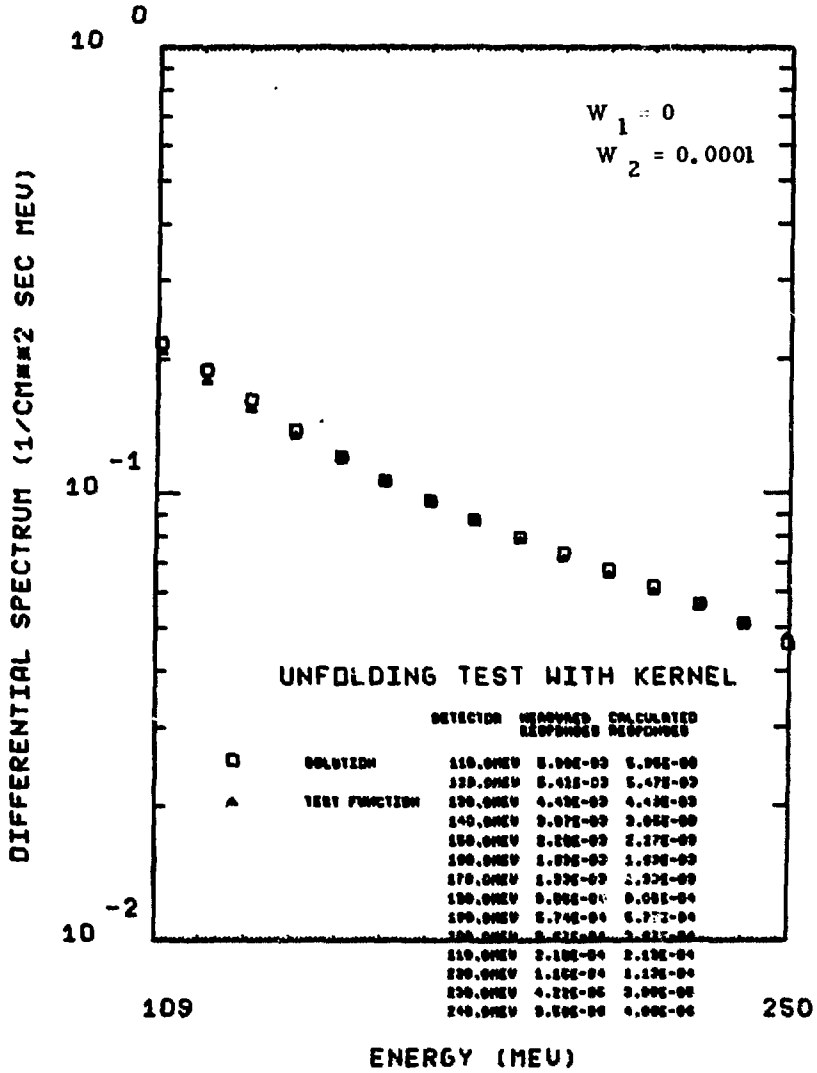

Fig. 36. Test of LOUHI program

VI. SAMPLE RESULTS

1. Measurement of stray neutron energy spectrum

The spectrometer setup was used to measure the stray neutron energy spectrum around the 184" Cyclotron at the Lawrence Berkeley Laboratory as a test of the overall scheme of the spectrometer. The spectrometer setup was positioned on the roof of the east counting area around the Cyclotron shielding blocks facing the accelerator. The orientation of the spectrometer setup was changed until it produced an azimuthal angular uniformity of the detected proton tracks. In this test run only 1 inch-thick polyethylene n-p converters were used. In the final measurement, about 4000 events were taken in the two hour run, and these data were used in the unfolding test. First, these proton track data were processed and a proton energy spectrum was generated. In this procedure, the forward extension option of the track was used, and those events whose extended end involved the frame were discarded in the generation of the proton energy spectrum. The first table (6-1) shows the overall result of the track data processing. According to it, there were 3921 events in the data tape, and 2146 events were free of machine irregularities and went through a least squares line check. Among them, 397 events could not pass through the line check, 455 events involved the frame when they were extended in the forward direction, and finally, 1294 events remained to generate the proton energy spectrum. Table (6-2) shows the fiducial pulse distances in each of the wands of 12 chambers before and after the experiment and the fiducial irregularities detected. It also shows the statistics of the spark types detected in each axis of the 12 chambers. Table (6-3) shows the statistics of the number of chambers sparked in each event, among the single track events, with the statistics of missing chambers in the double-scattering-like events. Table (6-4) shows the distribution of successful events in terms of proton energy and polar angle. Table (6-5) shows the deviations of spark positions from the fitted line in each chamber among the events which formed a straight line irrespective of their orientation. Finally, Fig. 38 shows the proton energy spectrum obtained from the successful events in the processing. Two broken line histograms

from the two energy conversion methods from the track lengths, respectively, as mentioned in Chapter IV. The dotted points are the values of data selected for unfolding the neutron energy spectrum.

2. Unfolded neutron energy spectrum

Kernel matrices were generated with the 1 inch converter thickness and the same inter-chamber spacings. Of course, the forward extension option of the track was used in sampling. Progressively peaking neutron angular shape has been assumed, varying linearly from A = 2 at neutron energy of 100 MeV to A = 8 at 200 MeV in $f(\mu) = \text{const.}\ \mu^A$. Tables (6-6, a and b) show the kernel matrix elements and sampling error bounds. Figure 39 shows the unfolded neutron energy spectrum when $\gamma = 1$, $W_1 = 0$ and $W_2 = 10^{-6}$ were used in the least squares unfolding process. The right hand side of the spectrum tends to go up, and probably this is due to the relatively greater contribution of the higher energy neutrons forming protons in this energy region. The energy spectrum for higher and lower energy regions could be obtained by using polyethelene converters of different thickness.

3. Concluding remarks

The test unfolded neutron energy spectrum shown in Fig. 39 gives a reasonable answer compatible with ordinary expectations. However, it is rather difficult to determine how reliable it is and how reliable the whole scheme is. These aspects will be studied further with more tests in the future. Here I would like to mention the things that need improvement in the near future. First, on the spectrometer setup side, the recording speed is too slow with only a magnetic tape deck. According to the simple calculation that assumes roughly 1 neutron/cm^2sec in the stray neutron field, we expect to have triggers of 10 to 20 events per second. However, the present cycling time is only once per second, due to the tape deck, and the system can not measure the absolute quantity of the neutron field with the present recording speed. This could be improved by connecting a small computer in the middle, acting as a buffer memory. Secondly, on the analysis side, the analytic expressions for the differential cross section, as a function of incident energy used in the sampling, need to be improved. Most of the experimental data for n-p cross sections are given as a function of emitting

proton angle or energy, for fixed incident neutron energies. But in our numerical unfolding process, we need the differential cross section as a function of incident neutron energy for fixed emitting proton energies, and the behavior of the present formula as a function of incident neutron energy is quite abrupt for fixed proton energies, even though it is well behaved as a function of proton energy for fixed neutron energies. We should improve the expression of the (n-p) differential cross section so that it gives a smoothly varying function on the incident neutron energy scale.

Table 6.1.

```
A. VARIOUS COUNTERS REPORT.

     NREC     =     785 ---( NO. OF RECORDS IN FILE )

       NPARF  =       1 ---( NO. OF PARITY ERRORS IN FILE )

     LENBIN( 1 ) =        1--(NO. OF RECORDS WHICH HAD EVENTS NUMBER   1 )

     LENBIN( 5 ) =      784--(NO. OF RECORDS WHICH HAD EVENTS NUMBER   5 )

     ------------------------------------------------------------------------

   ERROR COUNTERS IN ORDER OF DETECTIONS

     NEVTF    =    3921 ---( NO. OF EVENTS IN FILE )

       NBRITE =       0 ---( NO. OF BAD LEADING 7 CHECK )

     NGRITE   =    3921 ---( NO. OF GOOD LEADING 7 CHECK )

       NFSTPS =       4 ---( NO. STOPPED BY FID CHECKS. SEE C-1)

       NDTRST =     111 ---( NO. STOPPED BY DOUBLE TRACK EVENTS)

     NFPASS   =    3806 ---( NO. PASSING FID CHECK. SEE C-2 )

       MULSPK =     133 ---( MULTIPLE SCATT.-LIKE EVENTS )
       NORSCH =     685 ---( EVTS. HAVING LESS THAN TWO CH SPARKED
       JWHDIF =     243 ---( DIFF. JSWICH NO. EVENTS )
       NSAVE  =     135 ---( SAVED FROM THE ABOVE. )
       INCON1 =     469 ---( INCON. IN SINGLE SCAT. CASE. SEE C-3)
       NSAVE1 =     332 ---( SAVED FROM THE ABOVE. )
       INCON2 =      71 ---( DOUBLE SCAT-LIKE CASE )
       NDDBLS =     526 ---( DBL SCAT-LIKE EVENTS. SEE C-4 )
       NMPASS =       0 ---( EVTS. PROCESSED AMONG DBL-LIKE EVTS

     NPASS    =    2146 ---( EVENTS PASSED THE CHECKS SO FAR)


       NOLINE =     397 ---( NO. THAT HAD NO TRACK LINE IN LSQFIT

       NPESCB =       0 ---( ESCAPED EVENTS BY BACKWARD EXTENTION
       NPESCF =     455 ---( ESCAPED EVENTS BY FORWARD EXTENTION

     NLINE    =    1294 ---( TOTAL EVTS. HAVING TRACK LINES IN LSQ FIT )

     ------------------------------------------------------------------------

NOTE. CUMULATIVE REPORT INCLUDING THE PREVIOUS FILES ARE--

     NO. OF FILES READ ----        1
     NO. OF RECORDS READ --      785
     NO. OF PARITY-ERRORS -        1
     NO. OF EVENTS READ ---     3921
     NO. OF RECORD LENGTH ERROR---        1
```

Table 6.2.

B. FIDUCIAL PULSE DISTANCE REPORT IN OCTAL.

1. WHEN FILE PROCESSING STARTS.

CHAMBER NUMBERS	1	2	3	4	5	6	7	8	9	10	11	12
X-AXIS(HORIZONTAL)	3535	3531	3535	3534	3535	3536	3535	3536	3537	3536	3533	3537
Y-AXIS(VERTICAL)	3524	3522	3516	3520	3520	3523	3525	3524	3524	3523	3524	3523

2. WHEN FILE PROCESSING ENDS.

CHAMBER NUMBERS	1	2	3	4	5	6	7	8	9	10	11	12
X-AXIS(HORIZONTAL)	3533	3530	3533	3532	3533	3534	3533	3534	3536	3535	3531	3535
Y-AXIS(VERTICAL)	3522	3521	3514	3517	3516	3521	3523	3522	3522	3520	3521	3521

C. SPARK CHAMBERS PERFORMANCE REPORT.

C-1. FIDUCIAL CHECK ERROR FREQ. IN EACH CHAMBER --- NFDER(I,J,K)

1. X-AXIS (HORIZONTAL)

CHAMBER NUMBERS	1	2	3	4	5	6	7	8	9	10	11	12
NO FIRE	3	3	3	3	3	3	3	3	3	3	3	3
CLOCK ERROR	0	0	0	0	0	0	0	0	0	0	0	0
TOO LONG FID.	0	0	0	0	0	0	0	1	0	0	0	0
TOO SMALL FID.	4	3	8	7	6	2	6	9	2	1	2	2
TOTAL	7	6	11	10	9	5	9	13	5	4	5	5

2. Y-AXIS (VERTICAL)

CHAMBER NUMBERS	1	2	3	4	5	6	7	8	9	10	11	12
NO FIRE	3	3	3	3	3	3	3	3	3	3	3	3
CLOCK ERROR	0	0	0	0	0	0	0	0	0	0	0	1
TOO LONG FID.	0	0	0	0	0	0	0	0	0	0	0	0
TOO SMALL FID.	2	3	0	2	88	1	0	7	4	1	1	35
TOTAL	5	6	3	5	91	4	3	10	7	4	4	39

NOTE-- CLOCK AND TOO SMALL FID ERRORS ARE SAVABLE.

C-2. STATISTICS OF REGULAR DATA IN EACH CHAMBER---CHWND(I,J,K).

1. X-AXIS (HORIZONTAL)

CHAMBER NUMBERS	1	2	3	4	5	6	7	8	9	10	11	12
NO. OF ONE SPARK	282	454	1213	1301	1443	1440	1354	1250	1229	998	738	474
NO. OF TWO SPARKS	255	95	140	158	182	175	132	260	141	112	66	69
NO. OF NO SPARK	3269	2857	2453	2347	2181	2191	2320	2296	2436	2696	3002	3263
TOTAL	3806	3806	3806	3806	3806	3806	3806	3806	3806	3806	3806	3806

2. Y-AXIS (VERTICAL)

CHAMBER NUMBERS	1	2	3	4	5	6	7	8	9	10	11	12
NO. OF ONE SPARK	444	858	1277	1158	1497	1427	1260	1350	510	969	722	384
NO. OF TWO SPARKS	76	61	48	279	79	68	179	141	704	25	27	141
NO. OF NO SPARK	3286	2887	2480	2369	2230	2319	2367	2315	2584	2812	3057	3281
TOTAL	3806	3806	3806	3806	3806	3806	3806	3806	3806	3806	3806	3806

Table 6.3.

C-3 DETAILED STATISTICS OF SINGLE SCATT.-LIKE EVENTS---NRSPCH(CHNO,SPARKED CH NO.).

CHAMBER NUMBERS	1	2	3	4	5	6	7	8	9	10	11	12	TOTAL
1 CHMBS. SPARKED,	10	17	25	19	21	17	8	23	12	12	3	15	182
2 CHMBS. SPARKED,	5	30	28	28	29	23	22	27	23	13	20	0	248
3 CHMBS. SPARKED,	71	83	79	65	95	60	73	79	64	64	0	0	733
4 CHMBS. SPARKED,	52	52	56	52	53	50	35	43	38	0	0	0	431
5 CHMBS. SPARKED,	35	42	31	38	27	24	21	28	0	0	0	0	246
6 CHMBS. SPARKED,	29	29	26	22	18	13	17	0	0	0	0	0	154
7 CHMBS. SPARKED,	29	14	19	14	14	22	0	0	0	0	0	0	112
8 CHMBS. SPARKED,	16	9	7	7	13	0	0	0	0	0	0	0	52
9 CHMBS. SPARKED,	10	6	9	10	0	0	0	0	0	0	0	0	35
10 CHMBS. SPARKED,	8	4	9	0	0	0	0	0	0	0	0	0	21
11 CHMBS. SPARKED,	9	9	0	0	0	0	0	0	0	0	0	0	18
12 CHMBS. SPARKED,	12	0	0	0	0	0	0	0	0	0	0	0	12
TOTAL	286	295	289	255	270	209	176	200	137	89	23	15	2244

NOTE-- HORIZONTAL CH. NO. IS THE CH. NO. AT WHICH CONTINUOUS SPARKS STARTED AND VERTICAL NO. SHOWS THE SPARKED CHAMBER NO.

C-4 DETAILED STATISTICS OF DOUBLE SCATT.-LIKE EVENTS---NMSDAT(CH NO,MISSING CH NO.)

CHAMBER NUMBERS	1	2	3	4	5	6	7	8	9	10	11	12	TOTAL
1 CHMBS. MISSING,	0	19	11	27	11	13	29	11	9	4	8	0	142
2 CHMBS. MISSING,	0	6	14	20	6	29	14	9	13	14	0	0	125
3 CHMBS. MISSING,	0	8	11	17	18	15	5	6	10	0	0	0	90
4 CHMBS. MISSING,	0	5	8	17	11	4	6	8	0	0	0	0	59
5 CHMBS. MISSING,	0	4	8	16	11	6	6	0	0	0	0	0	51
6 CHMBS. MISSING,	0	5	8	7	4	6	0	0	0	0	0	0	30
7 CHMBS. MISSING,	0	4	2	1	5	0	0	0	0	0	0	0	12
8 CHMBS. MISSING,	0	3	1	7	0	0	0	0	0	0	0	0	11
9 CHMBS. MISSING,	0	3	3	0	0	0	0	0	0	0	0	0	6
10 CHMBS. MISSING,	0	0	0	0	0	0	0	0	0	0	0	0	0
11 CHMBS. MISSING,	0	0	0	0	0	0	0	0	0	0	0	0	0
12 CHMBS. MISSING,	0	0	0	0	0	0	0	0	0	0	0	0	0
TOTAL	0	57	66	112	66	73	60	34	32	18	8	0	526

NOTE-- HORIZONTAL CH. NO. IS THE CH NO. AT WHICH MIDDLE MISSING CHAMBERS STARTED.

Table 6.4.

3. ENERGY-POLAR ANGLE LOOK FOR THE NON-ESCAPED TRACKS ONLY. ENERGY IN MEV.

ACOS(MU)	84.3	78.5	72.5	66.4	60.0	53.1	45.6	36.9	25.8	0.	SUM
EKP= 55.0	0.	0.	0.	0.	0.	0.	0.	0.	0.	0.	0.
EKP= 65.0	0.	0.	0.	0.	0.	0.	0.	0.	0.	0.	0.
EKP= 75.0	0.	0.	0.	0.	0.	0.	0.	0.	0.	0.	0.
EKP= 85.0	0.	0.	0.	0.	0.	0.	0.	0.	0.	0.	0.
EKP= 95.0	0.	0.	0.	0.	0.	0.	0.	0.	0.	0.	0.
EKP= 105.0	0.	0.	0.	0.	0.	0.	0.	0.	0.	0.	0.
EKP= 115.0	0.	0.	0.	0.	0.	0.	0.	0.	0.	0.	0.
EKP= 125.0	0.	0.	0.	0.	0.	0.	0.	0.	103.0	287.0	390.0
EKP= 135.0	0.	0.	0.	0.	0.	0.	0.	57.0	58.0	74.0	189.0
EKP= 145.0	0.	0.	0.	0.	0.	0.	35.0	16.0	45.0	114.0	210.0
EKP= 155.0	0.	0.	0.	0.	0.	2.0	5.0	20.0	21.0	68.0	116.0
EKP= 165.0	0.	0.	0.	0.	2.0	5.0	10.0	9.0	39.0	37.0	103.0
EKP= 175.0	0.	0.	0.	0.	3.0	0.	7.0	6.0	7.0	59.0	82.0
EKP= 185.0	0.	0.	0.	0.	0.	1.0	3.0	7.0	11.0	40.0	62.0
EKP= 195.0	0.	0.	0.	0.	1.0	0.	2.0	4.0	8.0	23.0	38.0
EKP= 205.0	0.	0.	0.	0.	3.0	1.0	0.	1.0	3.0	15.0	24.0
EKP= 215.0	0.	0.	0.	0.	0.	1.0	3.0	4.0	5.0	17.0	30.0
EKP= 225.0	0.	0.	0.	1.0	1.0	1.0	1.0	2.0	2.0	10.0	18.0
EKP= 235.0	0.	0.	0.	0.	0.	0.	1.0	2.0	3.0	8.0	14.0
EKP= 245.0	0.	0.	0.	0.	1.0	0.	0.	1.0	3.0	12.0	17.0
EKP= 255.0	0.	0.	0.	0.	0.	0.	0.	0.	0.	0.	0.
EKP= 265.0	0.	0.	0.	0.	0.	0.	0.	0.	0.	0.	0.
EKP= 275.0	0.	1.0	0.	0.	0.	0.	0.	0.	0.	0.	1.0
EKP= 285.0	0.	0.	0.	0.	0.	0.	0.	0.	0.	0.	0.
EKP= 295.0	0.	0.	0.	0.	0.	0.	0.	0.	0.	0.	0.
EKP= 305.0	0.	0.	0.	0.	0.	0.	0.	0.	0.	0.	0.
SUM	0.	1.0	0.	1.0	11.0	12.0	68.0	129.0	308.0	764.0	1294.0

Table 6.5.

C-3 DETAILED STATISTICS OF SINGLE SCATT.-LIKE EVENTS---NRSPCH(CHNO,SPARKED CH NO.).

CHAMBER NUMBERS	1	2	3	4	5	6	7	8	9	10	11	12	TOTAL
1 CHMBS. SPARKED,	10	17	25	19	21	17	8	23	12	12	3	15	182
2 CHMBS. SPARKED,	5	30	28	28	29	23	22	27	23	13	20	0	248
3 CHMBS. SPARKED,	71	83	79	65	95	60	73	79	64	64	0	0	733
4 CHMBS. SPARKED,	52	52	56	52	53	50	35	43	38	0	0	0	431
5 CHMBS. SPARKED,	35	42	31	36	27	24	21	28	0	0	0	0	246
6 CHMBS. SPARKED,	29	29	26	22	18	13	17	0	0	0	0	0	154
7 CHMBS. SPARKED,	29	14	19	14	14	22	0	0	0	0	0	0	112
8 CHMBS. SPARKED,	16	9	7	7	13	0	0	0	0	0	0	0	52
9 CHMBS. SPARKED,	10	6	9	10	0	0	0	0	0	0	0	0	35
10 CHMBS. SPARKED,	8	4	9	0	0	0	0	0	0	0	0	0	21
11 CHMBS. SPARKED,	9	9	0	0	0	0	0	0	0	0	0	0	18
12 CHMBS. SPARKED,	12	0	0	0	0	0	0	0	0	0	0	0	12
TOTAL	286	295	289	255	270	209	176	200	137	89	23	15	2254

NOTE-- HORIZONTAL CH. NO. IS THE CH. NO. AT WHICH CONTINUOUS SPARKS STARTED AND VERTICAL NO. SHOWS THE SPARKED CHAMBER NO.

C-4 DETAILED STATISTICS OF DOUBLE SCATT.-LIKE EVENTS---NMSDAT(CH NO,MISSING CH NO.)

CHAMBER NUMBERS	1	2	3	4	5	6	7	8	9	10	11	12	TOTAL
1 CHMBS. MISSING,	0	19	11	27	11	13	29	11	9	4	8	0	142
2 CHMBS. MISSING,	0	6	14	20	6	29	14	9	13	14	0	0	125
3 CHMBS. MISSING,	0	8	11	17	18	15	5	6	10	0	0	0	90
4 CHMBS. MISSING,	0	5	8	17	11	4	6	8	0	0	0	0	59
5 CHMBS. MISSING,	0	4	8	16	11	6	6	0	0	0	0	0	51
6 CHMBS. MISSING,	0	5	8	7	4	6	0	0	0	0	0	0	30
7 CHMBS. MISSING,	0	4	2	1	5	0	0	0	0	0	0	0	12
8 CHMBS. MISSING,	0	3	1	7	0	0	0	0	0	0	0	0	11
9 CHMBS. MISSING,	0	3	3	0	0	0	0	0	0	0	0	0	6
10 CHMBS. MISSING,	0	0	0	0	0	0	0	0	0	0	0	0	0
11 CHMBS. MISSING,	0	0	0	0	0	0	0	0	0	0	0	0	0
12 CHMBS. MISSING,	0	0	0	0	0	0	0	0	0	0	0	0	0
TOTAL	0	57	66	112	66	73	60	34	32	18	8	0	526

NOTE-- HORIZONTAL CH. NO. IS THE CH NO. AT WHICH MIDDLE MISSING CHAMBERS STARTED.

Table 6.6.-a

KERNEL MATRIX --AKENEL

EN / EP	100.00 / 220.00	110.00 / 230.00	120.00 / 240.00	130.00	140.00	150.00	160.00	170.00	180.00	190.00	200.00	210.00
00.0	4.12E-04	3.51E-04	2.98E-04	2.65E-04	2.09E-04	1.59E-04	1.37E-04	1.11E-04	6.86E-05	8.97E-05	8.19E-05	7.44E-05
.0	5.91E-05	5.66E-05										
10.0	0.	8.67E-04	6.62E-04	6.52E-04	5.37E-04	4.21E-04	3.35E-04	2.62E-04	2.32E-04	2.11E-04	1.87E-04	1.65E-04
.0	1.47E-04	1.35E-04										
20.0	0.	0.	9.95E-04	8.14E-04	7.04E-04	6.00E-04	4.97E-04	3.66E-04	3.21E-04	2.83E-04	2.52E-04	2.20E-04
.0	2.04E-04	1.93E-04										
30.0	0.	0.	0.	1.09E-03	7.97E-04	6.74E-04	5.79E-04	4.13E-04	3.58E-04	3.19E-04	2.87E-04	2.41E-04
.0	2.15E-04	2.13E-04										
40.0	0.	0.	0.	0.	7.47E-04	6.16E-04	6.08E-04	4.52E-04	3.82E-04	3.39E-04	3.09E-04	2.52E-04
.0	2.10E-04	2.05E-04										
50.0	0.	0.	0.	0.	0.	7.67E-04	5.60E-04	4.56E-04	3.98E-04	3.63E-04	3.22E-04	2.53E-04
.0	2.03E-04	1.88E-04										
60.0	0.	0.	0.	0.	0.	0.	6.54E-04	4.42E-04	3.94E-04	3.60E-04	3.29E-04	2.60E-04
.0	1.82E-04	1.71E-04										
70.0	0.	0.	0.	0.	0.	0.	0.	7.07E-04	3.66E-04	3.45E-04	3.15E-04	2.62E-04
.0	1.79E-04	1.57E-04										
80.0	0.	0.	0.	0.	0.	0.	0.	0.	6.02E-04	3.29E-04	2.96E-04	2.57E-04
.0	1.68E-04	1.39E-04										
90.0	0.	0.	0.	0.	0.	0.	0.	0.	0.	4.47E-04	2.60E-04	2.29E-04
.0	1.58E-04	1.30E-04										
100.0	0.	0.	0.	0.	0.	0.	0.	0.	0.	0.	3.09E-04	2.10E-04
.0	1.51E-04	1.16E-04										
110.0	0.	0.	0.	0.	0.	0.	0.	0.	0.	0.	0.	2.48E-04
.0	1.23E-04	9.93E-05										
120.0	0.	0.	0.	0.	0.	0.	0.	0.	0.	0.	0.	0.
.0	1.05E-04	8.21E-05										
130.0	0.	0.	0.	0.	0.	0.	0.	0.	0.	0.	0.	0.
0.0	8.88E-05	5.34E-05										
140.0	0.	0.	0.	0.	0.	0.	0.	0.	0.	0.	0.	0.
0.0	0.	2.07E-05										

Table 6.6.-b

RELATIVE ERRORS -- RELERR

EN	100.00	110.00	120.00	130.00	140.00	150.00	160.00	170.00	180.00	190.00	200.00	210.00
EP	220.00	230.00	240.00									
100.0	3.55E-02	2.18E-02	2.47E-02	2.38E-02	2.33E-02	2.35E-02	2.38E-02	2.46E-02	2.50E-02	2.59E-02	2.60E-02	2.71E-02
.0	2.98E-02	2.14E-02										
110.0	0.	3.26E-02	2.11E-02	1.79E-02	1.71E-02	1.65E-02	1.67E-02	1.69E-02	1.60E-02	1.69E-02	1.72E-02	1.75E-02
.0	1.85E-02	1.90E-02										
120.0	0.	0.	2.75E-02	1.94E-02	1.67E-02	1.53E-02	1.51E-02	1.47E-02	1.48E-02	1.49E-02	1.49E-02	1.48E-02
.0	1.49E-02	1.50E-02										
130.0	0.	0.	0.	2.82E-02	1.99E-02	1.62E-02	1.55E-02	1.48E-02	1.48E-02	1.49E-02	1.50E-02	1.45E-02
.0	1.43E-02	1.42E-02										
140.0	0.	0.	0.	0.	2.94E-02	2.01E-02	1.67E-02	1.50E-02	1.51E-02	1.53E-02	1.53E-02	1.48E-02
.0	1.45E-02	1.43E-02										
150.0	0.	0.	0.	0.	0.	3.05E-02	2.09E-02	1.65E-02	1.57E-02	1.57E-02	1.59E-02	1.57E-02
.0	1.49E-02	1.48E-02										
160.0	0.	0.	0.	0.	0.	0.	3.24E-02	2.12E-02	1.72E-02	1.67E-02	1.69E-02	1.64E-02
.0	1.61E-02	1.57E-02										
170.0	0.	0.	0.	0.	0.	0.	0.	3.56E-02	2.27E-02	1.87E-02	1.84E-02	1.75E-02
.0	1.69E-02	1.67E-02										
180.0	0.	0.	0.	0.	0.	0.	0.	0.	3.56E-02	2.29E-02	1.95E-02	1.82E-02
.0	1.75E-02	1.74E-02										
190.0	0.	0.	0.	0.	0.	0.	0.	0.	0.	2.95E-02	2.37E-02	2.03E-02
.0	1.83E-02	1.80E-02										
200.0	0.	0.	0.	0.	0.	0.	0.	0.	0.	0.	2.79E-02	2.60E-02
.0	2.05E-02	2.01E-02										
210.0	0.	0.	0.	0.	0.	0.	0.	0.	0.	0.	0.	2.93E-02
.0	2.44E-02	2.24E-02										
220.0	0.	0.	0.	0.	0.	0.	0.	0.	0.	0.	0.	0.
.0	2.31E-02	2.86E-02										
230.0	0.	0.	0.	0.	0.	0.	0.	0.	0.	0.	0.	0.
.0	4.17E-02	2.77E-02										
240.0	0.	0.	0.	0.	0.	0.	0.	0.	0.	0.	0.	0.
.0	0.	1.11E-01										

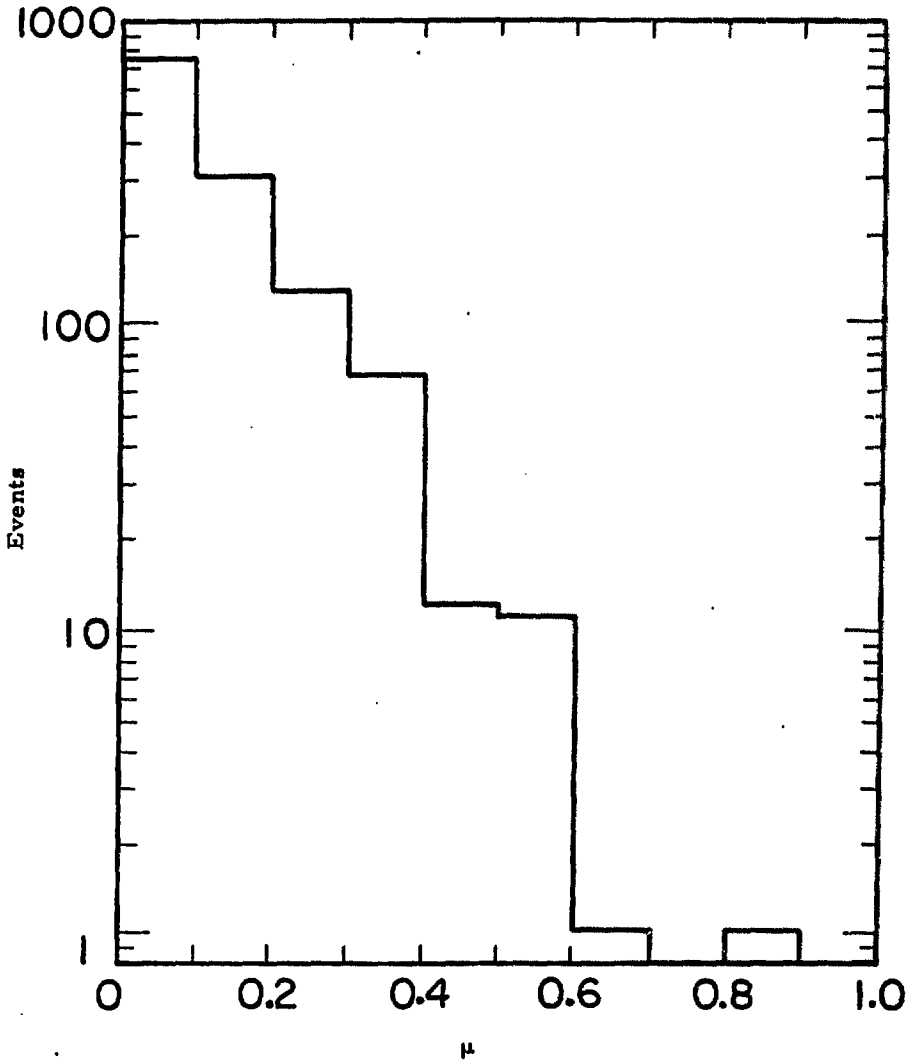

Fig. 37. Polar angle distribution of detected events.

XBL7212-4878

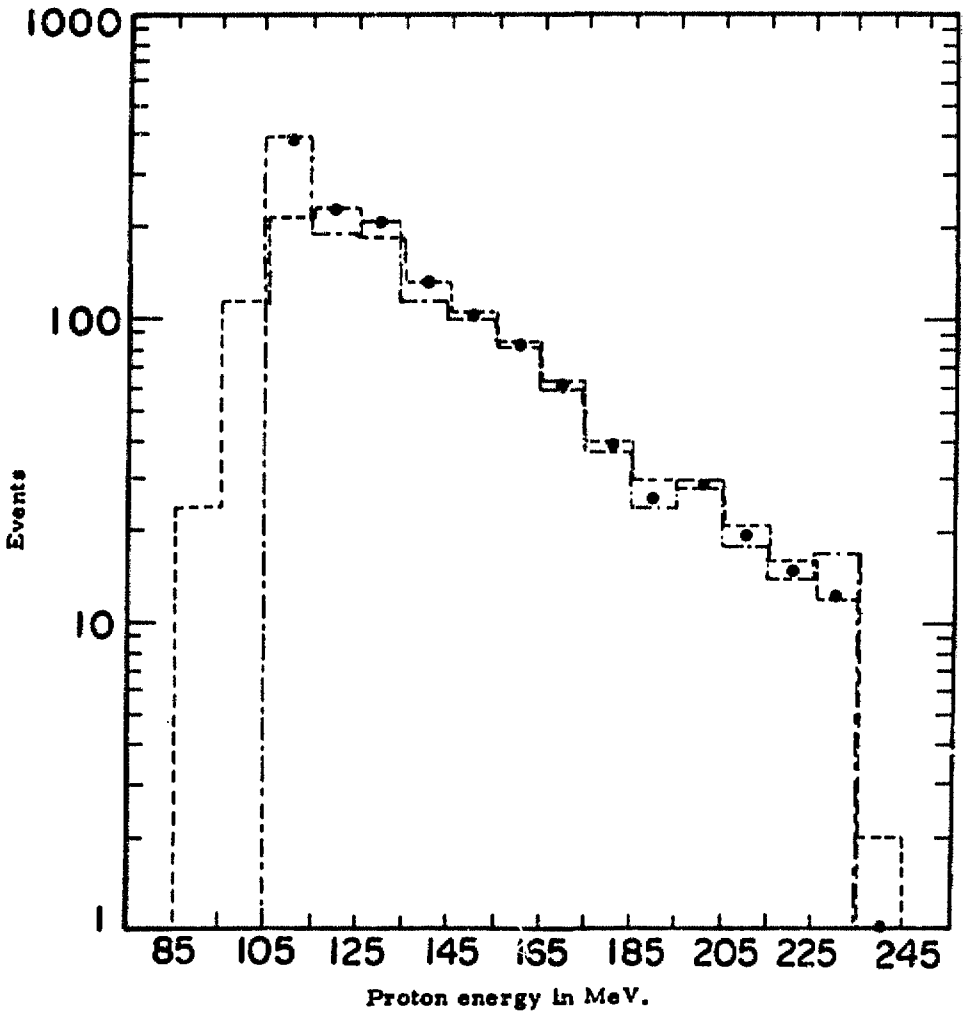

Fig. 38 Measured Proton Energy Spectrum

XBL7212-4877

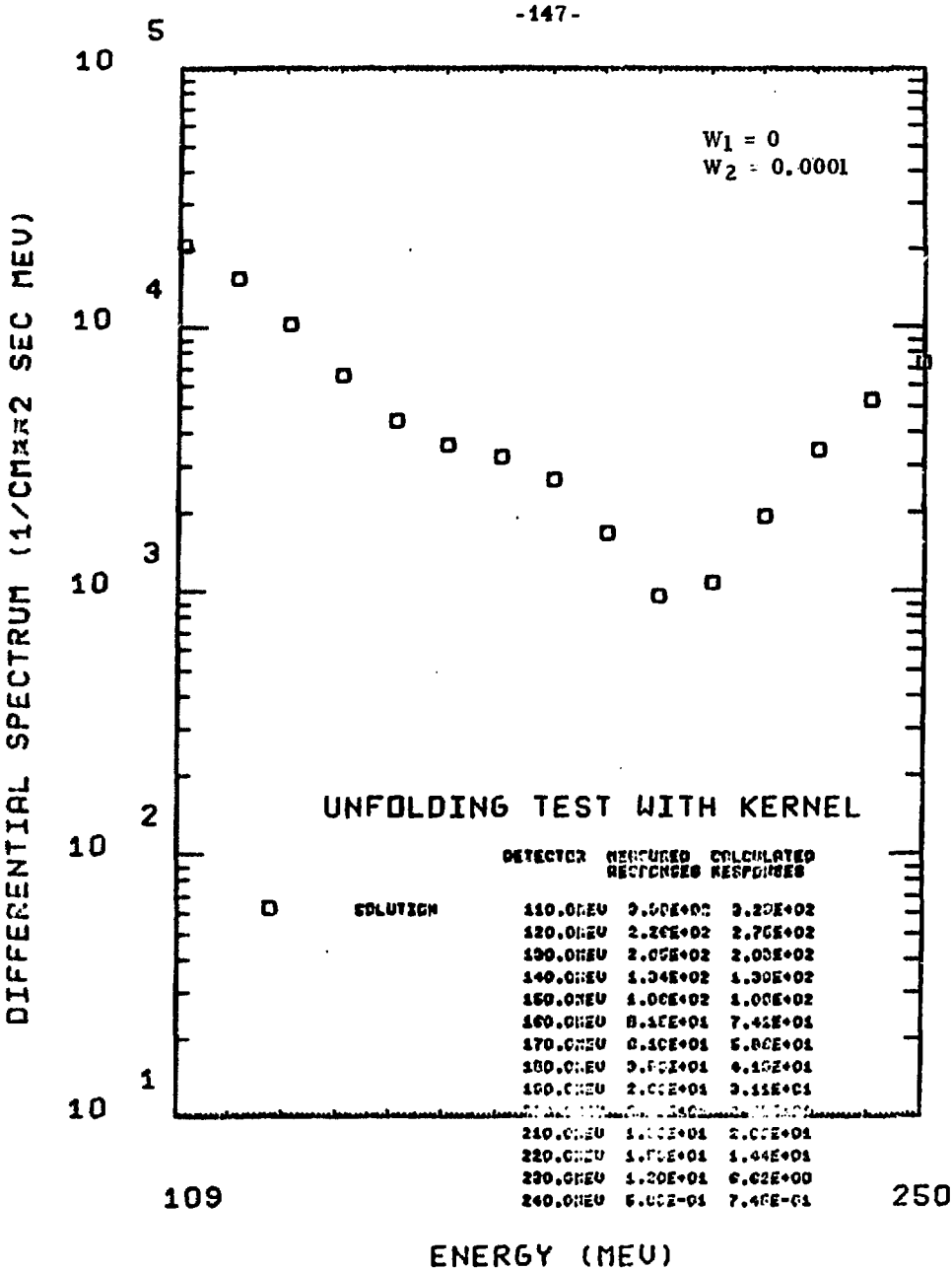

Fig. 39. Unfolded neutron spectrum

ACKNOWLEDGMENTS

I wish to express my gratitude and appreciation to Dr. Roger Wallace, Dr. Lawrence Grossman, and Dr. Victor Perez-Mendez who as members of my dissertation committee have provided guidance and assistance throughout my research work, and to Dr. Selig Kaplan for advising my graduate studies as my academic advisor.

I am greatly indebted to Mr. H. Wade Patterson for his enthusiastic support of this neutron spectrometer project, and to the entire Health Physics Department of the Lawrence Berkeley Laboratory for their continous support and cooperation. Particularly, I would like to thank Dr. Alessandro Rindi, who collaborated with me during the first half of this work, to Mr. Jerry Miller and Mr. Lloyd Stephens for their great help given during the 184-Inch Cyclotron beam run test, and to Mr. Leonard Proehl, in the Systems Group, for setting up and maintaining the magnetostrictive readout recording system.

The University Fellowship awarded during my first year at the University of California, Berkeley, which made it possible for me to have the privilege of graduate education, is greatly acknowleged. I now also would like to express my gratitude to Professors Pong-Yul Park, Byung-Ho Lee, Bong-Hee Han, and Chang-Gun Lee of the Seoul National University, Seoul, Korea, who encouraged me to have a graduate education in this country. My sincere thanks go to Mrs. Ellen Cimpher and Mrs. Mary Long, who have rendered valuable assistance throughout my graduate study and have typed the various drafts of this thesis, and to Mrs. Loretta Lizama, of the Information Division, for typing this report.

My most tender appreciation goes to my wife Hyang-Hy, whose understanding, patience, and continous support has made this possible. Finally, I want to dedicate this work to my mother.

REFERENCES

1. B. J. Moyer, Method of Calculation of Shielding for the Berkeley Bevatron, in The First International Conference on Shielding Around Large Accelerators, Saclay, France, 1962.
2. R. Wallace, Cyclotron Shielding, University of California Lawrence Radiation Report, UCRL-11315, 1965.
3. N. Metropolis, et al., Phys. Rev. 110, 185 , Part I Low-Energy Studies (1958).
4. H. W. Bertini, Phys. Rev. 131, 1801, Low Energy Intranuclear Cascade Calculation. (1963).
5. W. S. Gilbert, et al., CERN-LRL-RHEL Shielding Experiment at the CERN Proton Synchrotron, University of California Lawrence Radiation Laboratory Report, UCRL-17941, 1968.
6. H. W. Patterson, The Effect of Shielding on Radiation Produced by the 730 MeV Synchrocyclotron and the 6.3 GeV Proton Synchrotron at the LRL, in the First International Conference on Shielding Around Large Accelerators, Saclay, France, 1962.
7. A. R. Smith, Threshold Detector Applications to Neutron Spectroscopy at the Berkeley Accelerators, University of California Lawrence Radiation Laboratory Report, UCRL-16312, 1962.
8. J. R. Routti, High Energy Neutron Spectroscopy with Activation Detectors, Incorporating New Methods for the Analysis of Ge(Li) Gamma-Ray Spectra and the Solution of Fredholm Integral Equations, University of California Lawrence Radiation Report, UCRL-18514 1969.
9. M. D. Goldberg, Angular Distribution in Neutron-Induced Reactions, Brookhaven National Laboratory Report, BNL-400 1962.
10. R. Serber, Phys. Rev. 72, 1114, Nuclear Reactions at High Energies (1947).

11. R. G. Alsmiller, et al., Analytical Representation of Nonelastic Cross Sections and Particle Emission Spectra from Nucleon-Nucleus Collisions in the Energy Range 25 to 400 MeV, Oak Ridge National Laboratory Report, ORNL-4046, 1967.

12. V. Perez-Mendez, Developments in Magnetostrictive Readouts for Spark Chambers, Proceedings of the International Conference on Instrumentation for High-Energy Physics, held at Stanford, 1966.

13. V. Perez-Mendez and J. M. Pfab, Nucl. Instr. Methods 33, 141 (1965).

14. L. Kaufman, V. Perez-Mendez, and J. M. Pfab, IEEE Trans. Nucl. Sci. 3, 578 (June 1968).

15. B. Davison and J. B. Sykes, Neutron Transport Theory, Oxford at the Clarendon Press, 1958.

16. K. M. Kase and P. F. Zweifel, Linear Transport Theory, Addison-Wesley Publishing Co., 1967.

17. R. Madey, Range-Energy Tables, University of California Lawrence Radiation Laboratory Report, UCRL-2301, 1954.

18. R. Sanna, et al., Nuclear Emulsion Spectrometry at Low and Intermediate Energies, Health and Safety Laboratory Report, HASL-AEC, New York, July 1964.

19. W. R. Young, Neutron Spectra from an Organic Scintillator, University of California Lawrence Berkeley Laboratory Report, UCRL-16149, 1965.

20. J. L. Gammel, The n-p Total and Differential Cross Sections in the Energy Range 0-40 MeV, in Fast Neutron Physics, Part II, p. 2185, edited by J. B. Marion and J. L. Fowler, Interscience Publishers, New York, 1963.

21. F. Hajnal, Relativistic n-p Scattering Calculations for Recoil Proton Spectrometers, Health and Safety Laboratory Report, HASL - report, AEC, N. Y., October 1967.

22. L. B. Loeb, Basic Processes in Gaseous Electronics, University of California Press, Berkeley 1961.

23. J. G. Rutherglen, Spark Chambers, in Progress in Nuclear Physics, Vol. 9, 1964.

24. E. F. McLaughlin and R. V. Schafer, A Recirculator-Purifier for Spark Chamber Neon Gas, University of California Lawrence Radiation Laboratory Report, UCRL-18666, 1969.

25. R. V. Tuyl, K. lee, and V. Perez-Mendez, Electrical Pulsing and Operating Characteristics of Large Wire Spark Chambers with Magnetostrictive Readout, UCID-3099, 1967.

26. F. A. Kirsten, V. Perez-Mendez, and J. M. Pfab, Development of Magnetostrictive Chamber Readouts, UCID-2629, 1965.

27. S. Livingston and H. Bethe, Revs. Modern Phys. 9, 263 (1937).

28. W. H. Barkas and M. J. Berger, Tables of Energy Losses and Ranges of Heavy Charged Particles, in NAS-NRC Publication 1133, 1964.

29. M. L. Goldberger, Phys. Rev. 74, 1268 (1948).

30. H. Kahn, Applications of Monte Carlo, AECU-3259, 1954.

31. J. L. Doob, Stochastic Processes, John Wiley and Sons, 1953.

32. H. Cramér, Mathematical Methods of Statistics, Princeton University Press, 1946.

33. H. A. Meyer (ed.), Symposium on Monte Carlo Methods, John Wiley and Sons, New York, 1956.

34. A. Rindi and C. B. Lim, (n, p) Elastic Scattering: A Fitting Expression for the Differential Cross Sections in the Energy Range Between 22.5 and 400 MeV, University of California Lawrence Radiation Laboratory Report, UCRL- 20295, 1970.

35. H. Göllnitz, et al., Design of a Neutron Scattering Chamber Using Monte Carlo Calculations, Max-Planck Institute of Physics and Astrophysics report, München, September 1968.

36. D. C. Irving, The Adjoint Boltzman Equation and Its Simulation by Monte Carlo, Oak Ridge National Laboratory Report, ORNL-2879, 1970.

37. Y. A. Shreider (ed.), The Monte Carlo Method, Pergamon Press, 1966.

38. F. Hajnal, et al., Nucl. Instr. Meth. 69, 245, A Study of the Neutron Cascade in Iron, (1969).

39. W. B. Lovitt, Linear Integral Equations, McGraw Hill Book Co., 1924.

40. F. G. Tricomi, Integral Equations , Interscience Publishers, N. Y. 1957.

41. S. G. Mikhlin and K. L. Smolitsky, Approximative Methods for Solution of Differential and Integral Equations, American Elsevier Publishing Co.,N. Y., 1967.

42. W. C. Davidon, Variable Metric Method for Minimization, Argonne National Laboratory Report, ANL-5990, 1959.

43. E. Beals, VARMIT, LBL memo BKY-ZO (unpublished).

APPENDIX

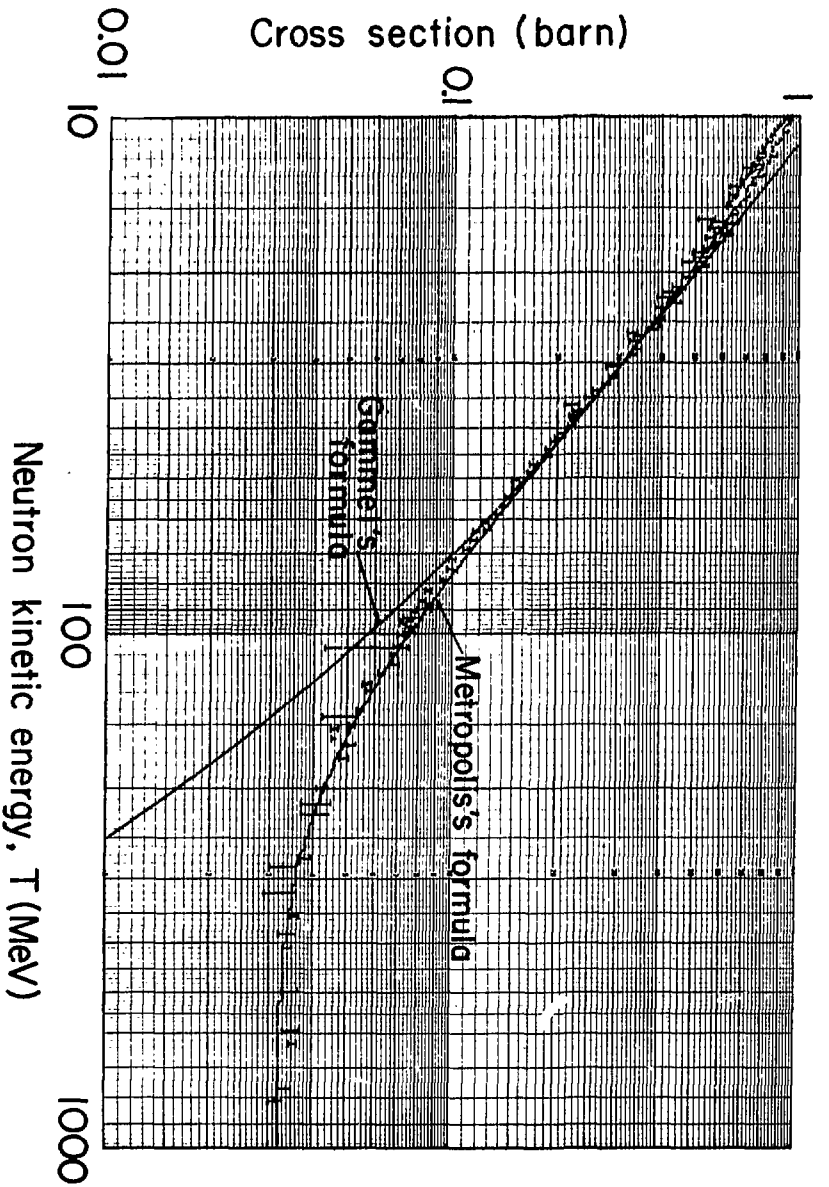

Fig. 1. Total n-p cross section data with fitting formulas

APPENDIX

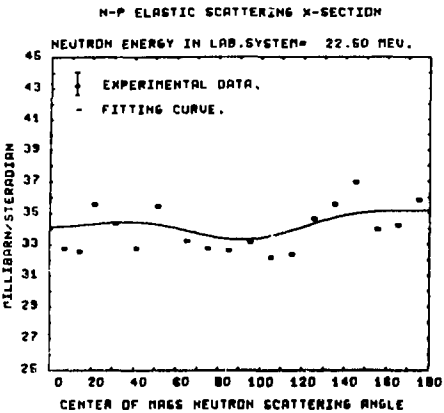

Fig. 2. Experimental data and fitting curves for np elastic scattering cross sections at various energies.

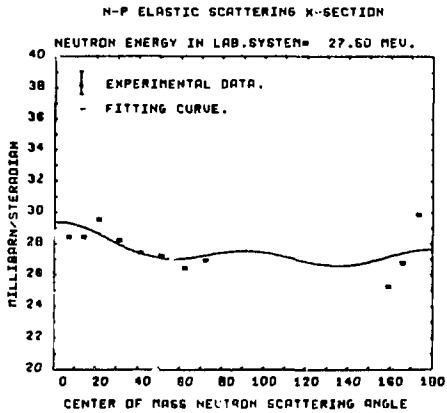

Fig. 3. Experimental data and fitting curves for np elastic scattering cross sections at various energies.

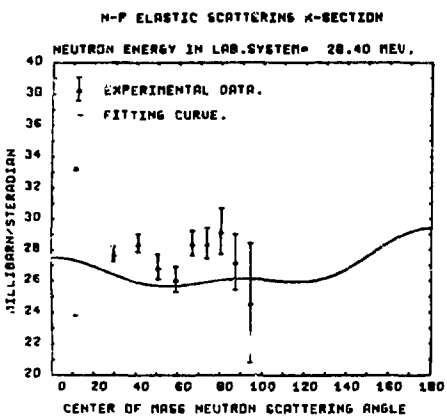

Fig. 4. Experimental data and fitting curves for np elastic scattering cross sections at various energies.

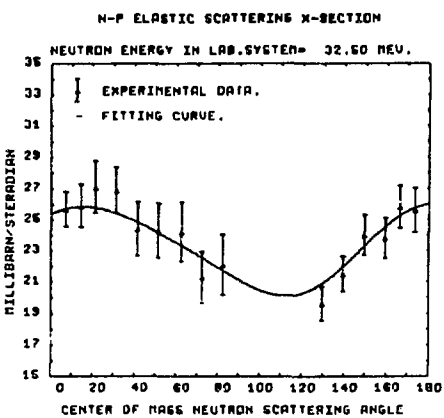

Fig. 5. Experimental data and fitting curves for np elastic scattering cross sections at various energies.

XBL 7212-5673

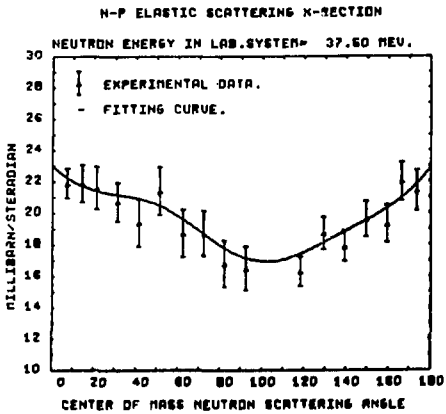

Fig. 6. Experimental data and fitting curves for np elastic scattering cross sections at various energies.

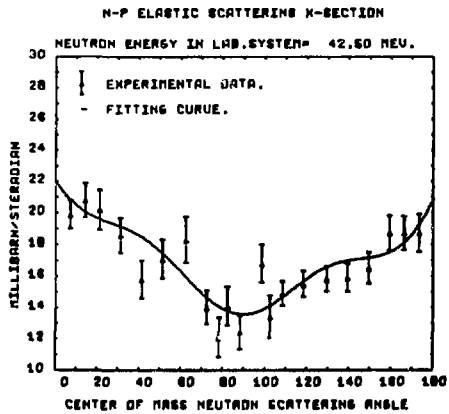

Fig. 7. Experimental data and fitting curves for np elastic scattering cross sections at various energies.

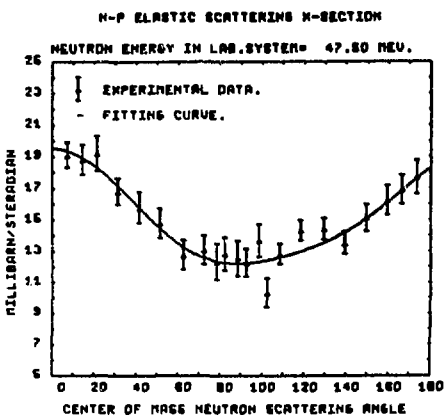

Fig. 8. Experimental data and fitting curves for np elastic scattering cross sections at various energies.

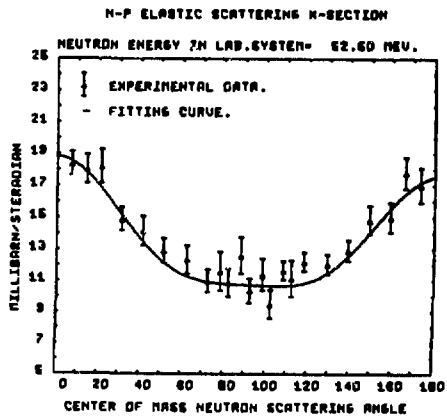

Fig. 9. Experimental data and fitting curves for np elastic scattering cross sections at various energies.

XBL 7212-5674

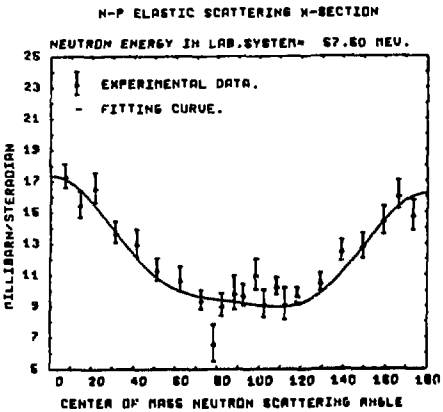

Fig. 10. Experimental data and fitting curves for np elastic scattering cross sections at various energies.

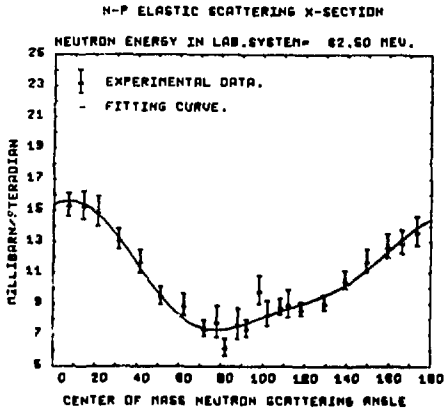

Fig. 11. Experimental data and fitting curves for np elastic scattering cross sections at various energies.

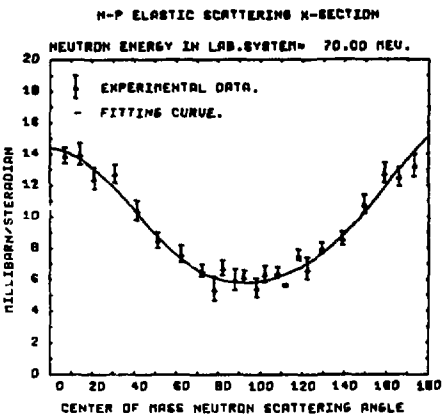

Fig. 12. Experimental data and fitting curves for np elastic scattering cross sections at various energies.

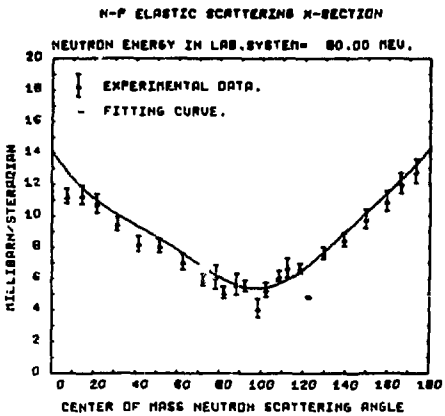

Fig. 13. Experimental data and fitting curves for np elastic scattering cross sections at various energies.

XBL 7212-5675

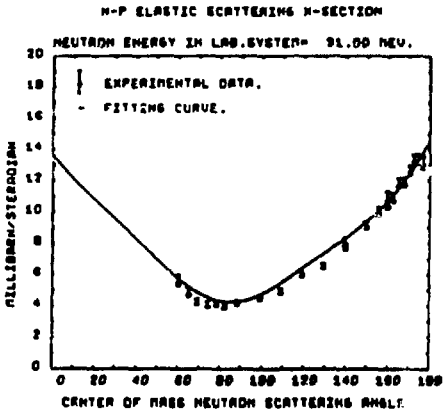

Fig. 14. Experimental data and fitting curves for np elastic scattering cross sections at various energies.

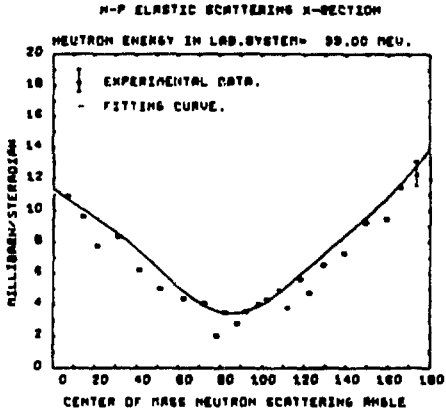

Fig. 15. Experimental data and fitting curves for np elastic scattering cross sections at various energies.

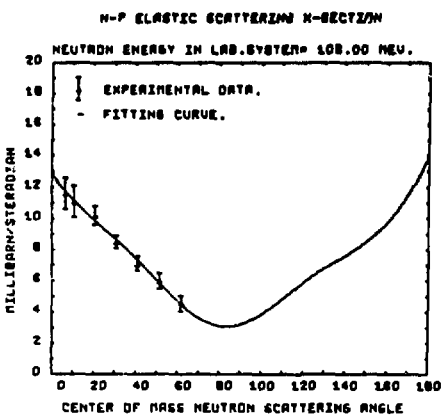

Fig. 16. Experimental data and fitting curves for np elastic scattering cross sections at various energies.

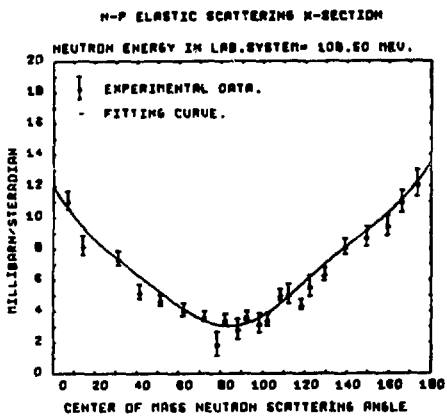

Fig. 17. Experimental data and fitting curves for np elastic scattering cross sections at various energies.

XBL 7212-5676

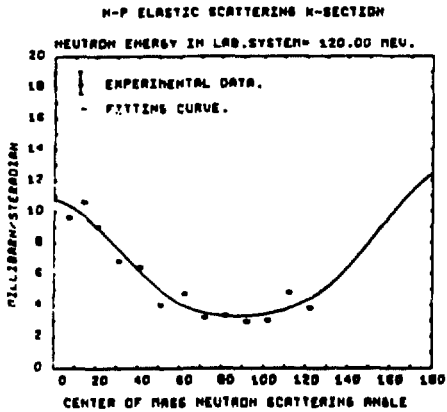

Fig. 18. Experimental data and fitting curves for np elastic scattering cross sections at various energies.

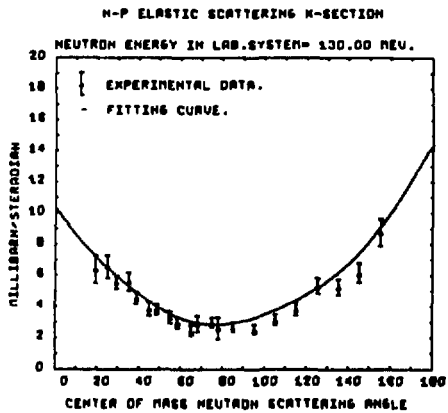

Fig. 19. Experimental data and fitting curves for np elastic scattering cross sections at various energies.

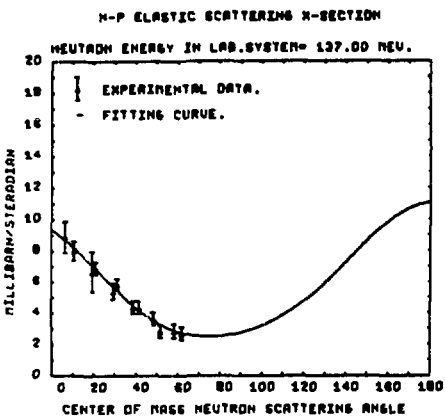

Fig. 20. Experimental data and fitting curves for np elastic scattering cross sections at various energies.

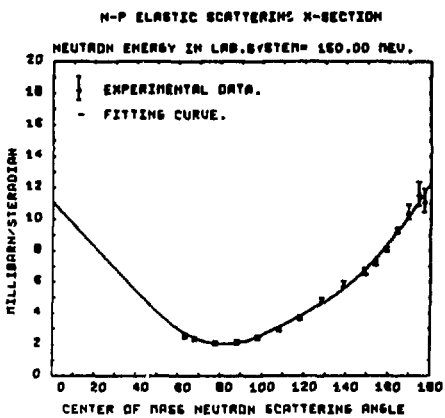

Fig. 21. Experimental data and fitting curves for np elastic scattering cross sections at various energies.

XBL 7212-7494

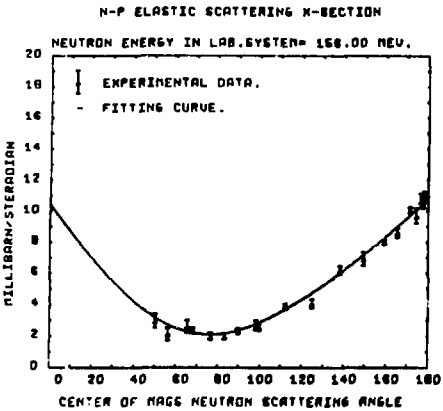

Fig. 22. Experimental data and fitting curves for np elastic scattering cross sections at various energies.

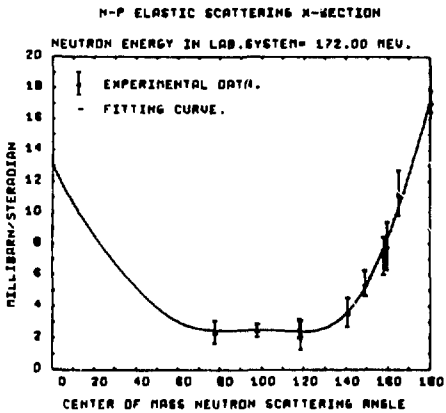

Fig. 23. Experimental data and fitting curves for np elastic scattering cross sections at various energies.

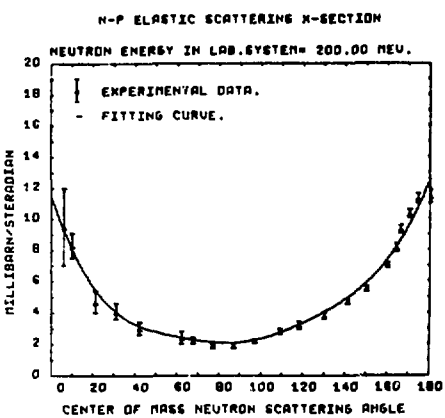

Fig. 24. Experimental data and fitting curves for np elastic scattering cross sections at various energies.

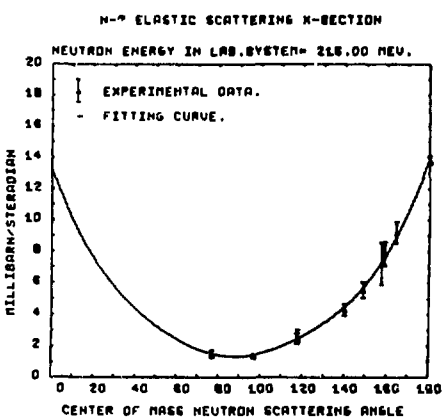

Fig. 25. Experimental data and fitting curves for np elastic scattering cross sections at various energies.

XBL 7212-7495

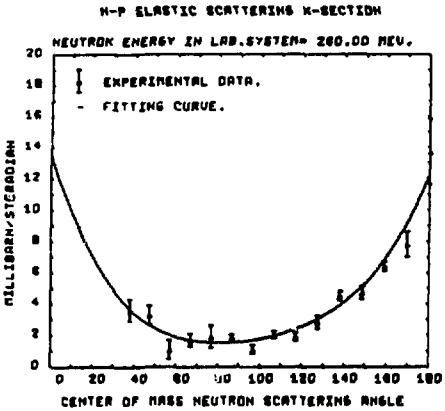

Fig. 26. Experimental data and fitting curves for np elastic scattering cross sections at various energies.

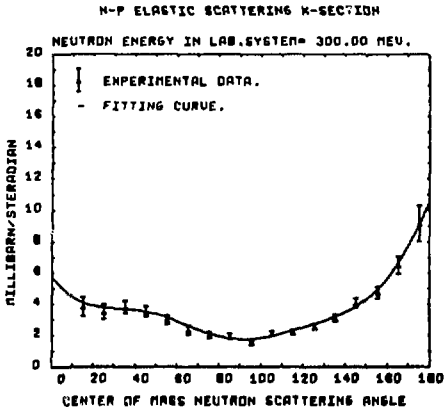

Fig. 27. Experimental data and fitting curves for np elastic scattering cross sections at various energies.

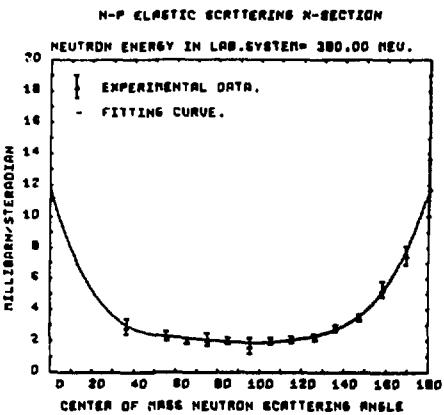

Fig. 28. Experimental data and fitting curves for np elastic scattering cross sections at various energies.

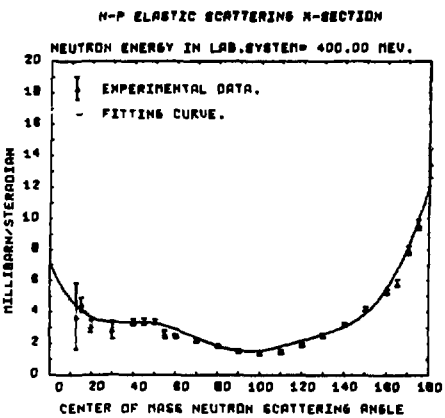

Fig. 29. Experimental data and fitting curves for np elastic scattering cross sections at various energies.

XBL 7212-7496

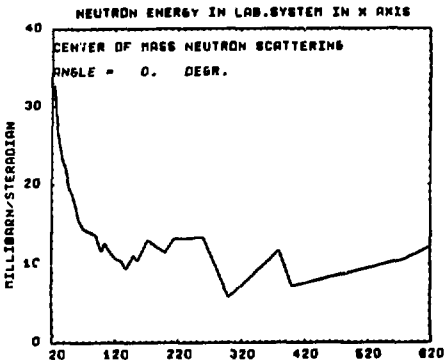

Fig. 30. Variation of cross section as a function of energy for various scattering angles.

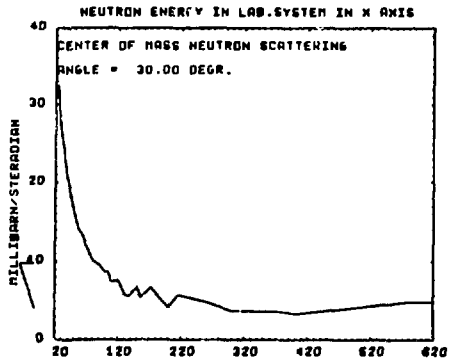

Fig. 31. Variation of cross section as a function of energy for various scattering angles.

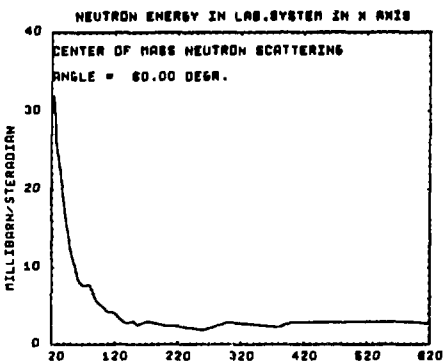

Fig. 32. Variation of cross section as a function of energy for various scattering angles.

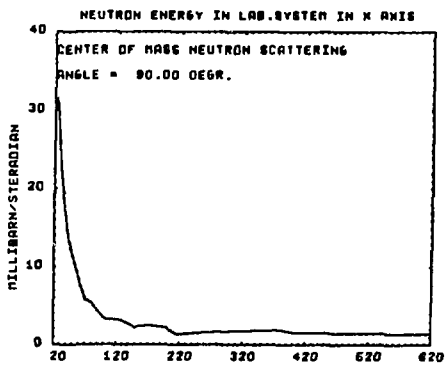

Fig. 33. Variation of cross section as a function of energy for various scattering angles.

XBL 7212-7497

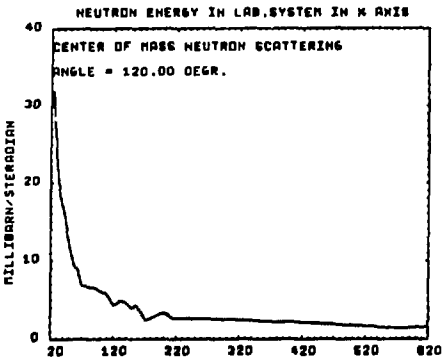

Fig. 34. Variation of cross section as a function of energy for various scattering angles.

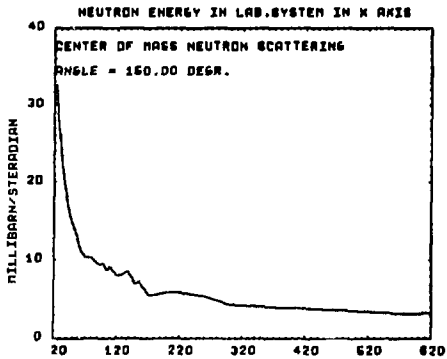

Fig. 35. Variation of cross section as a function of energy for various scattering angles.

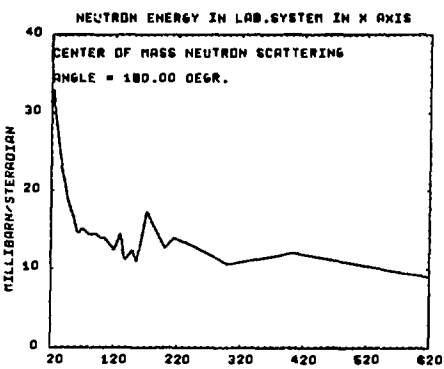

Fig. 36. Variation of cross section as a function of energy for various scattering angles.

XBL 7212-7498

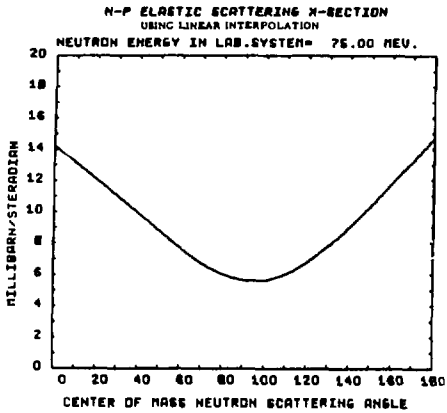

Fig. 37. Some examples of calculated np elastic scattering cross sections at some energies for which there are no experimental data.

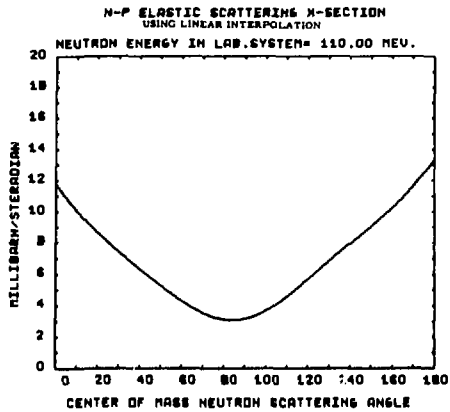

Fig. 38. Some examples of calculated np elastic scattering cross sections at some energies for which there are no experimental data.

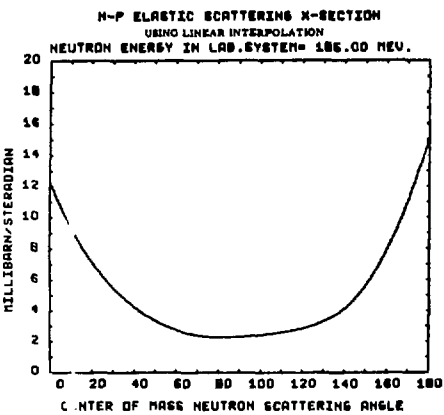

Fig. 3 . Some examples of calculated np elastic scattering cross sections at some energies for which there are no experimental data.

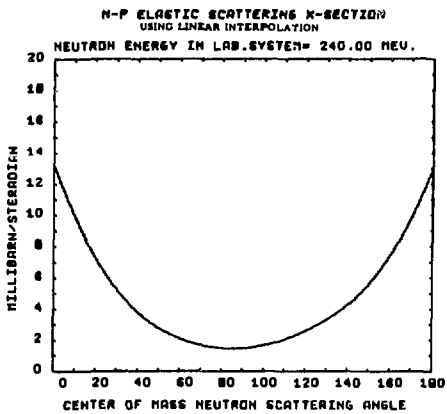

Fig. 40. Some examples of calculated np elastic scattering cross sections at some energies for which there are no experimental data.

XBL 7212-7499

-- END --